AN EXPERIMENTAL AND NUMERICAL STUDY OF TEMPERATURE UNIFORMITY ENHANCEMENT VIA PASSIVE GEOMETRY MODIFICATIONS IN AIR DILUTION MIXING

by

Ibrahim Soliman

A Thesis Submitted in

Partial Fulfillment of the

Requirements for the Degree of

Master of Science

in Engineering

at

The University of Wisconsin-Milwaukee

December 2023

ABSTRACT

AN EXPERIMENTAL AND NUMERICAL STUDY OF TEMPERATURE UNIFORMITY ENHANCEMENT VIA PASSIVE GEOMETRY MODIFICATIONS IN AIR DILUTION MIXING

by

Ibrahim Soliman

The University of Wisconsin-Milwaukee, 2023
Under the Supervision of Professor Ryoichi S. Amano

This work studies the effect of passive geometries on the temperature uniformity downstream of gas turbines dilution zones. The experimental setup simulates the non-reacting hot and cold air mixing in a dilution chamber, with inlet Reynolds number in the range of 40,000 – 95,000. Several CFD models were investigated and validated against experimental results. The proposed passive geometries include dilution jet extender parts that are installed on the large dilution holes (5mm to 25mm). The second proposed geometry is converging nozzle parts, called jet area modifiers, installed on the inner side of the large dilution holes. The converging nozzle parts have lengths of 5mm, 15mm, and 25mm and area ratios of 0.5 and 0.75. The presented research investigates the effect of different factors affecting temperature uniformity. Results indicate that temperature uniformity is the strongest factor affecting the usefulness efficiency, followed by the jet extender length. The Reynolds number does not have a significant effect on the usefulness efficiency. Jet extenders offer improvement on the temperature uniformity index by 0.9% - 14.9% depending on the temperature ratio and extender length. The added pressure drop varies between 5% and 28% depending on extender length. Jet area modifiers result in an improvement in the temperature uniformity index between 2% and 29%, and pressure drop of 8%-36% compared to the baseline extender case. The realizable $k-\varepsilon$ model showed good agreement with experimental data and performed well against $k-\omega$ (SST) and Reynolds Stress Turbulence (RST) models.

To

my parents, the light in my life, my everything.

TABLE OF CONTENTS

LIST OF FIGURES

LIST OF TABLES

NOMENCLATURE

Variables\Parameters

A	Area (m^2)
$C_{1\varepsilon}$	Turbulence model coefficient 1
$C_{2\varepsilon}$	Turbulence model coefficient 2
$C_{3\varepsilon}$	Turbulence model coefficient 3
C_p	Specific heat capacity for air ($J.kg^{-1}. K^{-1}$)
f	Mixture fraction
f^*	Normalized mixture fraction
G	Geometric propagation factor
g	Gravitational acceleration ($m.s^{-2}$)
G_b	buoyancy forces Turbulent kinetic energy generation ($W.m^{-3}$)
G_k	Velocity gradients Turbulent kinetic energy generation ($W.m^{-3}$)
k	Turbulence kinetic energy ($m^2.s^{-2}$)
$\dot{m}$	Total measured mass flowrate ($kg. s^{-1}$)
P	Pressure (Pa)
$\dot{q}$	Heat flux ($W.m^{-2}$)
R	Radius (m)
R_{air}	specific gas constant for air ($J.kg^{-1}.K^{-1}$)
r	Radial direction
Re	Reynolds number
T	Temperature (ºC)

$\bar{T}$	Average temperature (°C)
t	Time scale (s)
v, u	Total velocity component (m.s^{-1})
V	Velocity component (m.s^{-1})
x	Axial direction
Y_M	Non-homogonous dilatation effect term (W.m^{-3})
$Y+$	Nearest wall distance measured in viscous lengths

Greek Symbols

δ_{min}	Minimum total prism layers thickness
$\delta(x)$	Error in variable x
$\partial(x)$	Partial derivative of x
ε	Turbulence dissipation rate
μ	Absolute viscosity
μ_t	Turbulent eddy viscosity
ν	Kinematic viscosity
ρ	Air density
σ_k	Turbulence model coefficient
τ	Shear stress
ω	Specific turbulence dissipation rate
λ_T	Temperature Uniformity Index
η	Usefulness Efficiency

Subscript

a	Axial
avg	Average (arithmetic mean)
c	Cross-section

d	dynamic
eq	Equilibrium
f	Face on surface mesh
i	Tensor notation index (first dimension)
j	Tensor notation index (second dimension)
k	Tensor notation index (third dimension)
m	mean
p	Primary
r	radial
s	Secondary

Abbreviations

CAD	Computer Aided Design
CFD	Computational Fluid Dynamics
HP	High Pressure Stage
hp	Horsepower
RNG	Reynolds Normalization Group
RST	Reynolds Stress Turbulence
SST	Shear Stress Theory

ACKNOWLEDGEMENTS

I would like to extend my sincerest appreciation and love to my family, friends, and colleagues who supported me through this endeavor. I would also like to express my gratitude to Professor Ryo Amano for providing the support and resources necessary for this undertaking. The author is profoundly grateful to the UWM high-performance computing facility, and US Wright-Patterson Airforce Research Laboratory supported a part of the research. The computation grant is funded by NSF Award #2126229.

CHAPTER 1 – INTRODUCTION

1.1. Motivation

Gas turbine engines are widely used in various industries such as power generation, aviation and oil and gas, due to their high efficiency and power output. However, the temperature uniformity at the downstream section of the gas turbine dilution zones remains a significant challenge that needs to be addressed. Non-uniform temperatures across the turbine can result in thermal gradients and hot spots, which can lead to reduced component life and increased maintenance costs. The main aim of this research is to investigate the potential of using passive geometries in the downstream section of the dilution zones to improve the temperature uniformity of the combustion gases. The proposed approach is to modify the jet flow coming from the dilution holes by using passive geometries such as jet extenders and nozzle jet modifiers. By doing so, the goal is to promote better mixing of the hot gases, leading to a more uniform temperature distribution across the downstream section of the dilution zones. This research will be important to address the current challenges in the field of gas turbine combustion, which include reducing thermal gradients, hot spots and maintenance costs. The proposed approach, if proven to be successful, could provide a cost-effective solution to improve the temperature uniformity of the combustion gases, and can be easily implemented in existing gas turbine engines.

1.2. Gas Turbine Components and Operation

Gas turbines are an indispensable component in applications such as power generation and aircraft propulsion. Such that, these engines are typically used to generate utility-scale electricity, and even on-site generation for large industrial plants. Also, these engines are commonly used in ships and aircrafts to drive the propellers or provide aircraft thrust in jet engines.

A gas turbine is a type of internal combustion engine that utilizes a continuous flow of gas to convert mechanical energy into electrical energy via the turbine and alternator. The main three components of a gas turbine are the compressor, combustion chamber (or can), and the turbine. There are different classifications to gas turbine. First, the open cycle gas turbine, for which ambient air is compressed to high pressure, which raises the air temperature as well. After that, the compressed air is mixed with fuel in the combustion chamber, where an ignition leads to a combustion process. Then, the hot gas stream is routed through a stator array to the gas turbine, where the hot gases expand to rotate the gas turbine by exacting force on the gas turbine blades. After that, the mechanical energy of the gas turbine drives the main shaft which typically drives the compressors as well. Also, the mechanical energy of the rotating turbine is converted into electricity through the connected electrical generator (or alternator). Second, the combined cycle gas turbine operates under the same principles except that the hot gases that result from the combustion process are used to generate stream, which in turn is used to expand in a steam turbine to generate mechanical energy, and consequently, electricity through the connected alternator.

One of the main advantages of gas turbines is their high-power density [1], which makes it ideal for aircraft applications where weight and size are imperative. Also, gas turbine engines have a relatively higher response time compared to other engine types [2], which allows it to rapidly adjust the power output to match the demand. Gas turbine engines are characterized with a relatively lower emissions to compared to other engine types [3].

1.2.1. Gas Turbine Main Stages

An overview of a gas turbine engine is stated as follows. First, ambient air is drawn through the intake to the compressor, for which the air is compressed to high pressure. The compressor is typically designed in stages of sequential compression, and it is also driven by the gas turbine shaft. After the compression process, the high-pressure and high-temperature air flows to the combustion cans and is mixed with fuel at very precise rations, which is also subject to ignition to start the combustion process. After that, the hot gases flow through stators to the gas turbine blades, to expand through the turbine and exact forces on the blades in order to convert the flow energy to rate the turbine. The expanded hot gases exit the turbine through the exhaust and are typically used for jet thrust applications. It should be noted that all these processes occur continuously throughout the turbine at every section. **Figure 1** provides an overview of the components of a basic turbojet. In general, a gas turbine gas be split into four stages as follows:

1. Compression: The compressor draws atmospheric air and compresses it to high pressure, which increases the air density and temperature.
2. Combustion: The compressed air enters the combustion chamber, where it is mixed with fuel and ignited. This process generates hot gases.
3. Expansion: The hot gases from combustion expand through the turbine, causing it to spin and generate mechanical power.
4. Exhaust: The gases exiting the turbine are at a lower pressure and temperature than the combustion gases and are exhausted to the atmosphere in case of open cycle gas turbines.

A combined cycle utilizes the exhaust air to heat steam, which in turn is used to expand in a steam turbine.

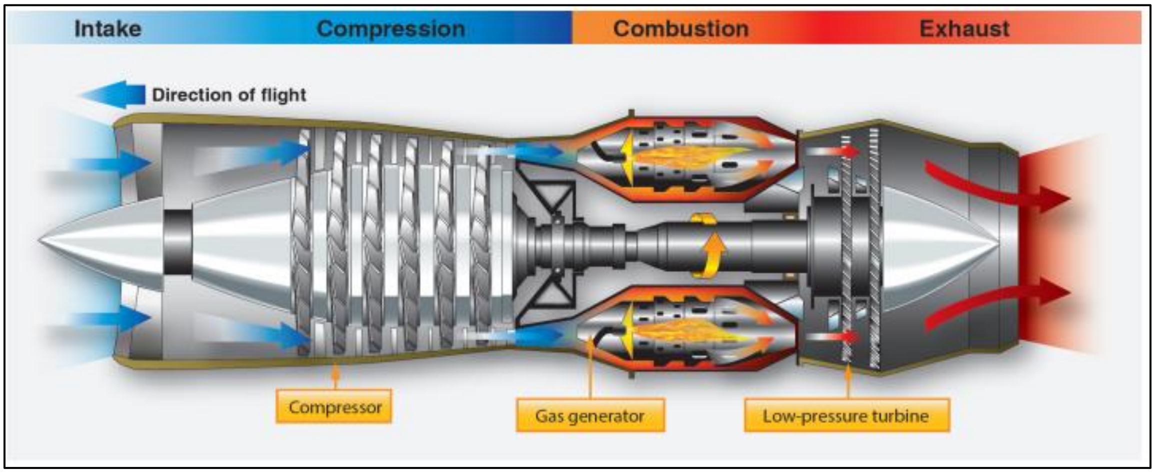

Figure 1: Basic turbojet components *[4]*

1.2.1.1. Compression Stage

The compression stage starts with drawing atmospheric air and then compressing it to high pressure and temperature. In most situations, the compressor is of axial or centrifugal type and modular design, where it is comprised of multiple stages of fan blades that rotate around the shaft axis to compress the air. Higher compression of the air results in a more efficient expansion in the turbine, and more power throughput. This characteristic is quantified by the compression ratio, defined as the ratio between the inlet to outlet pressures. The compression ratio is imperative in the design of gas turbines, where higher compression ratios indicate a better performance. To achieve higher engine performance, compressor designs feature modifications such as variable inlet guide vanes to optimize the flow of gases. Also, ceramic blades are used for their ability to withstand high pressure and temperature, which enables higher compression ratios. The compressed air exits through guide vanes to the diffuser section. The purpose of the divergent diffuser section is to further convert the dynamic energy associated with velocity into static pressure, which is favorable for the compression ratio and conducive to satisfactory combustion.

1.2.1.2. Combustion Stage

The compressed air from the compression stage enters the combustion zone, where it is mixed with fuel and then ignited. This leads to a combustion process which generates the hot gases that are necessary for the expansion process in the next stage. The combustion chamber has different configurations, one of which is the can-annular type, which is used to industrial power plants. Such that, the compressed air flows through a hollow chamber, where it surrounds the fuel injectors. The fuel is injected into the chamber and is mixed with the compressed air, just to be ignited shortly after to commence the combustion process. The performance of the gas turbine engine depends on the efficiency of the combustion process, for which, higher temperature and pressure of the combustion gases are sought after. Incomplete combustion or quenched combustion due to inadequate fuel-air ratios or mixing degrades the performance of the gas turbine. This is because the expanded gases do not reach the design pressure levels and more importantly, contain incomplete combustion products such as Carbon Monoxide (CO), Nitrogen Oxides (NOx), and Sulfur Oxides (SOx). These oxide byproducts are very harmful to humans and to the environment. To improve the combustion process, advanced strategies such as lean-burn are used, in which a lean fuel-to-air mixture is used to achieve a complete combustion with reduced emissions. The latter approach is especially powerful with NOx traps that absorb any residual Nitrogen Oxides (NOx) that result from the combustion process.

In general, the combustion chamber can be divided into three zones as primary, secondary, and tertiary as shown by **Figure 2**. The air is introduced around the jet fuel in the primary zone, which has 15-20% of the compressed air flow. This is the region where combustion starts. Then, 30% of the compressed air is introduced in the secondary zone to complete the combustion process. Finally, the remainder of the air, approximately 50-55% is introduced within the tertiary zone, also known as the dilution zone. The dilution zone serves the purpose of cooling the extremely hot combustion gases and providing a certain degree of turbulence to promote mixing and to reduce hot streaks that can damage the gas turbine blades within the next stage of the engine.

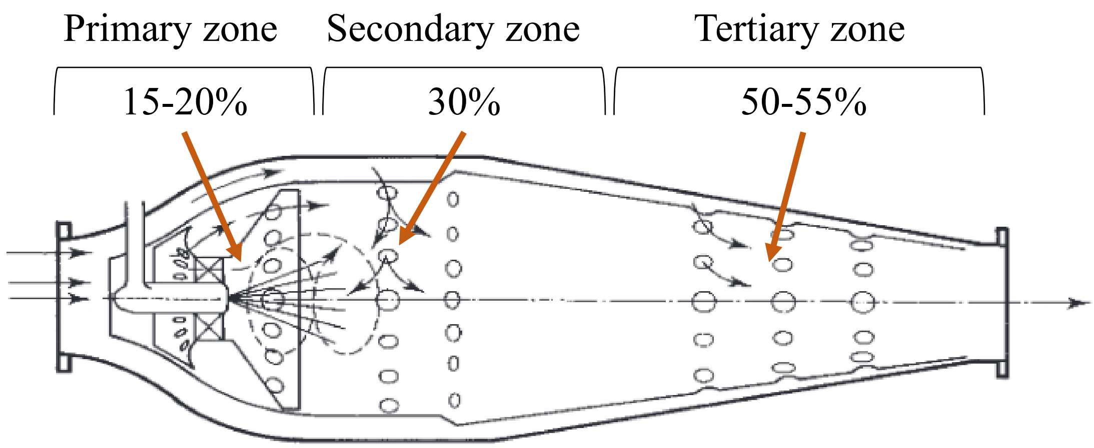

Figure 2: Combustion chamber zones and percentage of compressed air introduction (adapted from *[49]*)

1.2.1.3. Expansion Stage

The hot gases enter the expansion stage to impinge on the gas turbine blades and convert the hot gases flow energy and drive the turbine to generate electricity. The hot gases enter through the nozzle stators, an array of stationary components with a geometry specially designed to redirect the hot gases and guide it an optimal angle relative to the turbine blades. The stator blades convert more of the hot gases energy associated with static pressure into a dynamic energy component, which results in more useful energy that can be extracted by the gas turbine blades. Therefore, the nozzle stators improve the efficiency of the gas turbine. The hot gases expand through the turbine rotor blades, which causes the turbine shaft to rotate. Turbine stators are located at the downstream of the turbine rotors, and their function is to maintain an optimal flow angle and reduce swirling. The combustion firing temperature is the highest temperature within the engine, and it can reach up to 2,071 ^{o}C [5] in modern engines. These operating conditions constitute a metallurgical challenge so that new alloys and component materials can operate safely [6]. Therefore, gas turbine engine components must be built to withstand these temperature levels throughout a reasonable lifecycle. The importance of withstanding high temperatures is amplified within the turbine section, as the rotating components are more prone to failure due to the kinetic stresses that are added to the thermal stresses due to high temperature and varying temperature profiles. Therefore, turbine blade materials are typically made of nickel alloys, ceramic composites, and titanium alloys, all of which are characterized with high tolerance to pressure and temperature of the combustion gases. Ensuring a uniform temperature profile is imperative to prolong the life of the gas turbine engine components, which can be achieved via adequate quenching (dilution) techniques, internal cooling of components, and external cooling as well.

1.2.1.4. Exhaust Stage

After converting the hot gases energy in the expansion process, the expanded gases are discharged through the exhaust. In case of jet engines, the exhaust gases pass through an exhaust nozzle, which is a passive device with special convergent geometry that helps to shape and direct the hot gases as they are discharged to the atmosphere. Sometimes, some of the energy from the exhaust gases is recovered through a recuperator, which is a heat exchanger that is used to recover some energy from the exhaust to preheat the compressed air before combustion, which enhances the efficiency of the gas turbine engine. Exhaust gases are also used in the combined cycle to heat steam in a closed heat exchanger, and in turn the steam is used in a Rankine cycle to drive a steam turbine and generate electricity. The exhaust gases may contain high levels of pollutants that are very harmful to the environment. Hence, several emission reduction methods are employed such as using filters, NOx traps, and catalytic converters. The exhaust stage expels relatively high velocity hot gases, which can generate significant noise, especially in power generation mega gas turbines. Exhaust mufflers are usually employed to conform with regulations and keep noise levels in check. Finally, some gas turbine engines utilize exhaust gas recirculation, in which a small portion of the exhaust gases is rerouted to the combustion chamber in order to quench the combustion temperatures and reduce the Nitrogen Oxides (NOx) pollutant levels.

1.3. Challenges in Gas Turbine Engines and Active Research

There are several challenges that are faced in gas turbine engines, and ongoing research is being conducted to improve their efficiency and address these problems. First, some research seeks to improve the efficiency of gas turbine engines through advanced materials, aerodynamics, and combustion methodologies to enhance the efficiency and reduce fuel consumption. Emission reduction is an active area of research as Nitrogen Oxides (NOx), Sulfur Oxides (NOx), and particulates pose a serious threat on the environment. Some research studies new emission control technologies in advanced combustion techniques, exhaust gas recirculation, and emission control systems. Operating gas turbines at higher combustion temperatures allows for improvements in the overall efficiency of the engine. However, engine components need to withstand extreme temperature levels without catastrophic failure, especially dynamic components that are already under kinetic stresses. To improve the range of operating temperature, some research focuses on advanced materials that can withstand high temperature. For example, Improved materials such as advanced ceramics, superalloys, and advanced composites are being developed to withstand the extreme temperatures and pressures in order to increase the efficiency and reduce the weight of the engine. Another approach to improving the lifespan of engine components is to enhance the cooling efficiency. Engine component research aims to improve the cooling performance of engine components using different methods such as internal cooling, external cooling, and thin film technology. Nonuniform temperature profiles at the upstream of turbine blades is yet another challenge in gas turbine engines as the variation of temperature across the turbine blade causes hot spots, and therefore thermal stress. Ultimately, thermal stress on the turbine blades reduces their lifespan and increases the chances of sudden and catastrophic failures, which can easily destroy other parts of the engine and cause irreparable damage. Hence, research is being conducted on improving the non-uniformity challenge through streamline bodies, dilution hole guide vanes, and optimization of the dilution zone geometries.

1.4. Problem Statement

Gas turbine engines are commonly used in various industries such as power generation, aviation and oil and gas, due to their high efficiency and power output. However, despite their advantages, there are still some challenges that need to be addressed in order to optimize their performance and prolong the life of the components. One of the main challenges is achieving optimal temperature uniformity in the downstream section of the gas turbine dilution zones. The downstream section of the dilution zones is where the combustion gases are mixed with cool air to reduce their temperature before they reach the turbine blades. The uniformity of the temperature across the turbine blade is crucial to prevent thermal gradients and hot spots, which can lead to reduced component life and increased maintenance costs.

To address this challenge, this research aims to investigate the potential of using passive geometries in the downstream section of the dilution zone to improve temperature uniformity. The proposed approach is to modify the jet flow coming from the dilution holes by using two passive geometries: dilution jet hole extenders and nozzle jet modifiers. The dilution jet hole extenders are cylindrical shell geometries that provide extra protection for the dilution hole jet, allowing it to develop further without being influenced by the crossflow. The aim of this jet extender is to enable the dilution jet to penetrate further into the main flow, and delay the effect of the crossflow. The nozzle jet modifier is the second investigated geometry, which is also installed at the dilution holes. This geometry is a decreasing area cylinder, similar to a converging nozzle. The aim of this converging nozzle shape is twofold: first, to provide the same protection against crossflow as outlined earlier in the example of the jet extender, and second, to increase the mean velocity of the dilution jet and enable the jet to penetrate further into the main stream.

By using these passive geometries, the goal is to promote better mixing of the hot gases and a more uniform temperature distribution across the downstream section of the dilution zones. This research will be important to address the current challenges in the field of gas turbine combustion, which include reducing thermal gradients, hot spots and maintenance costs. The proposed approach, if proven to be successful, could provide a cost-effective solution to improve the temperature uniformity of the combustion gases, and can be easily implemented in existing gas turbine engines.

CHAPTER 2 – LITERATURE REVIEW

The topic of improving temperature uniformity in the downstream section of gas turbine dilution zones has received notable attention for a long time. A number of studies have been conducted to investigate different methods and techniques for achieving optimal temperature uniformity in this area. The literature review on this topic can be broadly categorized into two main areas: the use of active control systems and the use of passive geometries. In terms of active control systems, researchers have investigated the use of methods such as active cooling, exhaust gas recirculation, and fuel injection strategies to achieve better temperature uniformity in the downstream section of the dilution zones. These studies have shown that active control systems can be effective in reducing thermal gradients and hot spots, but they can also be complex and costly to implement. Alternatively, the use of passive geometries has gained attention as a cost-effective and simple alternative to active control systems. Studies have focused on using passive geometries such as vortex generators, porous walls, and jet hole extenders to modify the jet flow coming from the dilution holes. These studies have shown that passive geometries can be effective in promoting better mixing of the hot gases and achieving a more uniform temperature distribution in the downstream section of the dilution zones.

Hot streak migration is a phenomenon that occurs in gas turbine blades, where high temperature hot spots, or "streaks," form and migrate along the surface of the blade. These hot streaks can be caused by a variety of factors, such as uneven fuel distribution or combustion instability. The migration of hot streaks along the blade can lead to several problems, including increased thermal stress, reduced blade life, and reduced turbine efficiency. Hot streaks can cause the formation of hot corrosion, which is a type of corrosion that occurs at high temperatures and can further degrade the blade. To mitigate the detrimental effect of hot streak migration, several research studies have focused on the factors influencing their migration and the overall effect on the performance [7] [8] [9] [10]. The study by Adams et al. [11] presents an experimental and computational investigation into the effects of combined hot streaks and swirl on turbine aerodynamics. The study was conducted in the Oxford Turbine Research Facility (OTRF) which is a short-duration rotating transonic facility that matches the nondimensional parameters relevant to turbine fluid mechanics and heat transfer to engine conditions. The turbine under investigation is the LEMCOTEC turbine which has been designed to represent modern aero-engine architectures and is robust to lean-burn combustor-representative inlet flows. Two turbine inlet flows were considered, one being uniform in total pressure, total temperature, and flow angle and the other featuring a nonuniform total temperature (hot streak) profile superimposed on a swirling velocity profile. The study found that the inlet temperature nonuniformity was relatively well preserved upon being convicted through the turbine and that the predicted root mean-square variation in the IP vane exit total temperature field was approximately double that with uniform inlet conditions. The study highlights the challenge of accurately predicting the complex IP vane flow and the importance of controlling dimensionless numbers such as Reynolds number to achieve better outcomes. Amano et. al. [12] conducted an experimental and numerical study on the effect of jet-to-mainstream momentum flux ratio on the temperature uniformity downstream of the dilution zone. Results show that an increase in the jet-to-mainstream momentum flux ratio yields an improvement in the mixed gas temperature uniformity.

Other research and novel designs focused on improving the geometry of gas turbine combustors, to improve thermal uniformity and air flow [13] [14] [15]. For example, the work by Hatch et al. [16] examines the mixing characteristics of jets in an axisymmetric can geometry. Temperature measurements were taken downstream of a row of cold jets injected into a heated cross-stream. The study found that the jet-to-mainstream momentum-flux ratio and orifice geometry significantly impact the mixing patterns in a cylindrical configuration. The results showed that, at a fixed momentum-flux ratio, jet penetration decreases with an increase in slanted slot aspect ratio and an increase in the angle of the slots with respect to the mainstream direction. The study concludes that further investigation is needed to identify optimum mixing conditions when the number of orifices, orifice aspect ratio, and angle are varied over a larger parameter space. Selim, Al Hamad, and Amano [17] investigated the effect of dilution housing geometry on the pressure drop and temperature uniformity. The work explores 4 different slant angles for the dilution housing converging section. Experimental and numerical results found that using a housing slant angle of 45^{o} degrees results in 37% improvement in the temperature uniformity at the exit section, and a 0.5% increase in pressure drop, compared to the baseline case. Gupta et. al. [18] performed an experimental and numerical study on the effect of guide vanes on the temperature uniformity of dilution sections. The authors tested 45^{o} degree spherically swept guide vanes to redirect the dilution zone into the primary stream and therefore, enhance mixing. The tested guide vane orientations include 0^{o}, 30^{o}, 60^{o}, and 90^{o} degrees. Results indicate that guide vanes improve the temperature uniformity by 5-7% depending on the installation orientation. In another work, Gupta et. al. [19] conducted an experimental and numerical study focused on the effect of guide vanes on the temperature uniformity in dilution zones. Four different guide vane orientations were studied, including 0^{o}, 30^{o}, 60^{o}, and 90^{o} degrees. Results show that the 30^{o} guide vane yielded the highest temperature uniformity in the downstream mixed gas. It was found that the average temperature uniformity of this arrangement is 15% higher than that of the baseline case. It was also shown that the added pressure drop was only 1% higher than the baseline case.

Some research focused on improving the temperature uniformity by using passive techniques such as guide vanes and insert bodies. Barringer et al. [20] performed an experimental and numerical study on the improvement of temperature uniformity using passive techniques. The authors have used a large-scale wind tunnel section to simulate the flow conditions of a prototypical combustor and to determine the effects of a representative combustor flow field on the nozzle guide vane. The study aims to understand the flow dynamics and thermal behavior of the combustor and its effects on the downstream turbine. The study found that the dilution jets generate turbulence levels of 15-18% at the exit of the combustor with a length scale that closely matches that of the dilution hole diameter. Also, the total pressure exiting the combustor in the near-wall region neither resembles a turbulent boundary layer nor is it completely uniform, which challenges the commonly made assumptions about the combustor flow. The study provides a detailed analysis of the flow field and thermal behavior, which is important for understanding the performance of gas turbine combustors. El Gammal et al. [21] [22] work describes an experimental study on the effect of streamlined body geometries on the mixing of hot and cold air streams in a gas turbine combustor. The study uses four different streamlined body shapes (teardrop and American football, in two sizes) to enhance the interaction between the hot and cold streams and improve the dilution process. Overall, the study suggests that the use of streamlined body geometries can be an effective way to improve the dilution process in gas turbine combustors. The results of the study indicate that the American football and teardrop shapes with similar dimensions are the most effective in improving the uniformity of the flow while minimizing pressure loss. The study also highlights the importance of controlling dimensionless numbers such as the blockage ratio, profile ratio and Reynolds number to achieve the best results in the dilution process. The work of Amano and Selim [23] focused on developing passive control techniques to improve mixing and temperature uniformity in dilution zones. The authors investigated the effect of guide vanes on the outlet temperature of dilution zones. They found that internal guide vanes provided superior performance to external guide vanes. Also, the work concludes that internal guide vanes with 30o orientation resulted in 14% improvement in outlet temperature uniformity.

Other studies have explored various jet shapes, such as circular, elliptical, square, diamond, and triangular, with different orientations and aspect ratios (AR) in order to optimize mixing performance in subsonic and supersonic flows [24]. Some recommends to use noncircular geometries, such as high aspect ratio elliptical and blunt square jets in subsonic flows and equilateral triangle and diamond jets in supersonic conditions [25]. Another study recommended the use of isosceles triangle jets in a crossflow with a Reynolds number of 15,000 using hot tungsten wire measurements to evaluate the centerline mean flow and turbulence characteristics [26]. Zhang et al. [27] investigated experimentally and numerically the same effect of molecular weight (helium and nitrogen) at constant jet-to-crossflow momentum ratio, and observed that the velocity gradient between the jet and primary flow plays a crucial role in breaking up large-scale vortices and improving mixing with helium, and increasing penetration with nitrogen.

Other research delved into the impact of temperature ratio on the cooling effectiveness and temperature uniformity in heat transfer applications [28] [29] [30]. Gustafsson and Johansson [31] conducted a parametric study to assess the temperature distribution on effusion-cooled plates in combustion chamber conditions. the authors investigated variable temperature ratios, air velocity ratios and geometric dimensions. The authors found that temperature ratios and velocity ratios between cold and hot air streams to be the most critical variables. They also found a nearly linear relationship between the temperature ratio and surface temperature. Soghe et. al. [32] conducted a numerical study to assess the effects of temperature ratio on the cooling performance of jet impingement applications. This research focuses on low-pressure turbine applications. The work presents CFD simulations that are validated against experimental data. The authors investigated temperature ratios between 1.105 to 2.05. The work concludes that the local and average Nusselt numbers are indirectly proportional to the temperature ratio, with variation in the Nusselt number as high as 35% across different temperature ratio cases. Zhao et. al. [33] conducted a numerical study on the cooling effectiveness and temperature uniformity in steam-cooled turbine blades. The authors investigated different variables including inlet temperature, pressure ratio, and temperature ratio. the study found that the outlet pressure does not significantly affect the cooling performance. Also, they found that as the temperature ratio increases from 0.6 to 0.7, the temperature non-uniformity decreases by 30.08%, and the cooling efficiency increases by 7.35%.

CHAPTER 3 – EXPERIMENTAL SETUP AND METHODOLOGIES

The experiment was designed to simulate the mixing process of hot (main stream) and cold (secondary stream) gases in dilution sections like those found in gas turbine engines, albeit in a non-reacting fashion and at relatively lower temperature and pressure values compared to gas turbine engines in the industry. The aim of the experiment is to assess different methods to improve the temperature uniformity of mixed (downstream) gases by employing passive geometry modification techniques. This experiment aims to shed light on the flow kinetics and heat transfer in low temperature dilution mixing sections, and for inspiring new research in reacting high-turbulence testing of gas turbine dilution sections. The experimental design was based on recommended geometries from literature. The measurement points are positioned to facilitate appropriate resolution measurements of pressure and temperature at different sections of the experiment setup.

3.1. Experiment Setup and Components

The experiment is designed to emulate the non-reacting mixing of hot and cold gases in dilution zones. The experiment setup is inspired by and based on that given by Barringer et al. [20] while being modified into a circular cross-section to resemble more closely the designs found in the industry. The experiment apparatus is comprised of different sections fabricated from 18 inch-gauge galvanized steel with a total length of 4.675 m. **Figure 3** shows the experimental rig, while **Figure 4** demonstrates the experimental rig dimensions.

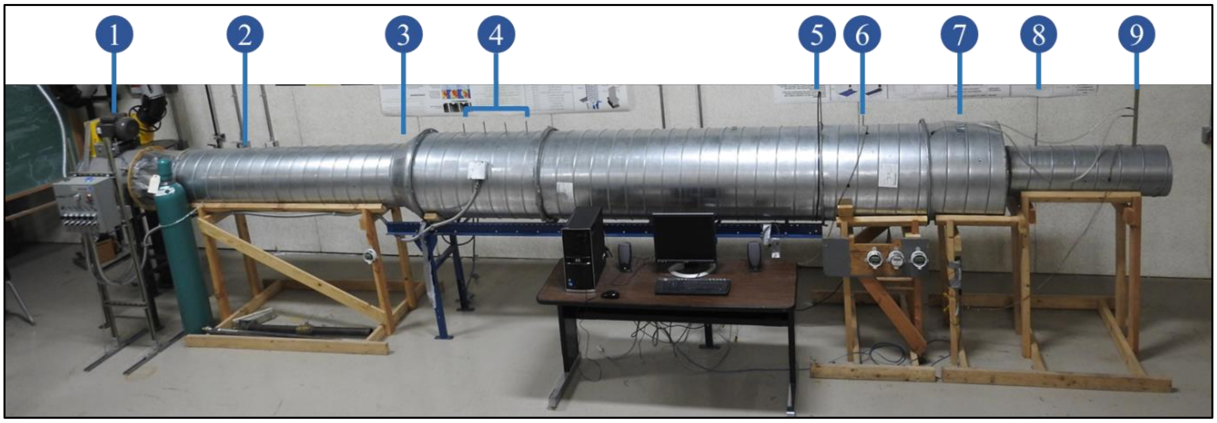

Figure 3: Experimental rig sections. (1) Blower, (2) First damper, (3) Second damper, (4) Electric heating elements, (5) Upstream pitot tube, (6) Upstream thermocouples, (7) Test section, (8) Downstream thermocouples, (9) Downstream pitot tube

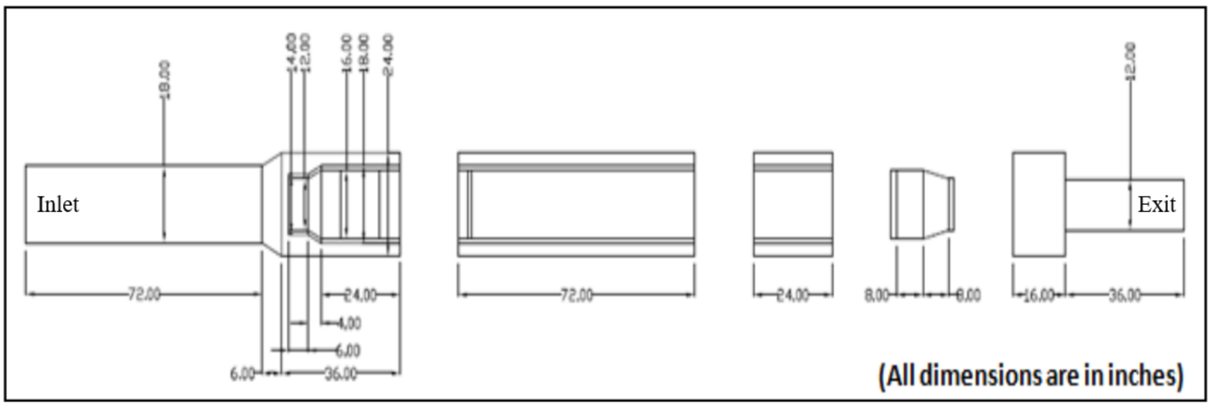

Figure 4: experimental rig dimensions

First, the upstream section contains a 3 HP fan that provides a total stream of air at a flow rate of 1.727 m^3/s at ambient temperature. Then, two volume dampers are used to control the air flow split between the primary and secondary flow sections that follow. The primary flow section has a circular cross-sectional area with a diameter of 0.4064 m, and is equipped with two sets of fin-strip heating coils. The first heating coil set is comprised of four 1950 W and 240 V at a diameter of 0.225 m. The other set is comprised of three 3700 W and 240 V at a diameter of 0.368 m.

Therefore, the heating strips have a combined capacity of 19 kW. The purpose of these heating strips is to heat the primary stream of air to emulate the hot gases stream entering the dilution zone. The secondary stream is directed by the volume dampers into an annular section with an annulus radius of 0.0762 m. The air passing through the secondary stream section is maintained at ambient temperature. A cladding is designed between the hot and cold gas sections, which is made from glass wool at a thickness of 2.54 cm. The aim of the glass wool cladding is to insulate the hot and cold sections and maintain temperature control in the upstream sections before the dilution zone mixing section. After splitting the main fan flow into primary and secondary streams, each of these streams flows separately for about 3.35 m to allow for the hot air to be heated evenly and for the flows to develop. Then, the flows meet in the dilution shell section, which is comprised of two parts. **Figure 5** shows the dilution zone shell in the experiment rig.

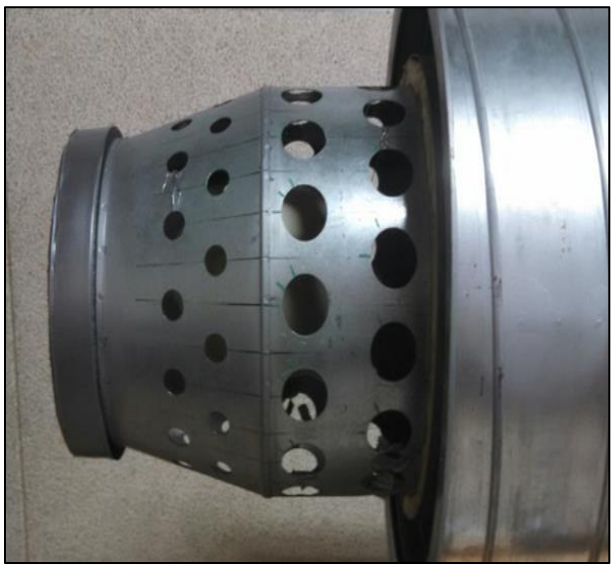

Figure 5: Dilution test section in the experiment rig

The first part of the dilution shell is a cylinder with a cross section diameter of 0.4064 m and a length of 0.2032 m. This part contains two sets of 16 large dilution holes, each. The large dilution holes have a diameter of 5 cm distributed evenly along the perimeter of the section, and the center-to-center distance between the two large dilution hole arrays is 10 cm. The second part of the dilution shell is a converging section with conical frustum geometry of 17^{o} slant angle and a length of 0.2032 m. This converging region contains two arrays of equally distributed small dilution holes, each with a diameter of 2.5 cm, and the center-to-center distance between the two small dilution hole arrays is 5 cm. In this region, mixing happens as the secondary cold stream passes through the dilution holes to mix with the primary hot stream that is flowing into the inner section of the dilution shell section. This section is housed by an 18-inch-gauge galvanized steel duct with a diameter of 0.6096 m. Finally, after mixing happens in the dilution zone, the mixed gases pass through to the outlet pipe section, which has a diameter of 0.3048 m and a total length of 0.9144 m.

3.2. Instruments and Measurement Techniques

The experiment contains different measurement points at the upstream and downstream areas of the dilution zone test section. Pitot tube measurements are used to measure static and total pressure at several measurement points across the pipe radius. These measurements allow us to calculate the velocity before and after the dilution test section. Equally distributed sets of thermocouples are installed in the upstream and downstream measurement points. The thermocouples are used to record the temperature profiles in the radial direction for the hot and mixed gas streams. The thermocouples are connected to a data acquisition system to record the measurements. The ambient temperature and barometric pressure are recorded during the experiment runs.

3.2.1. Pressure Measurement

Static and total pressure measurements were employed to calculate the radial velocity profile before and after the dilution test section. The pressure measurements were collected via pitot tubes attached to a Fluke 922 Airflow Micromanometer. The reported accuracy of the Fluke 922 device is within 1% and 2.5% for pressure and velocity, respectively. **Figure 6** demonstrates the used Fluke manometer.

Figure 6: Fluke 922 Airflow Meter/Micromanometer *[34]*

The first measuring point is at 45 cm before the dilution test section, in which the pitot tube is lowered to take seven measurements for each the static and total pressure, each measurement at a different location across the radius of the primary stream section. The total pressure of the secondary stream is recorded. Another pitot tube on a slider system is installed 20 cm before the end of the exit pipe. The total and static pressure are recorded at seven different locations along the radius of the exit pipe.

By measuring the static and total pressure profiles for the primary and exit stream sections, we can obtain the velocity profile for these sections at different radial locations. The velocity profile is used to calculate velocity averaged mass flow rate for these sections, by which we can calculate the secondary stream flow mass flow rate, mean velocity, as well as the static pressure through the measurement of total pressure that happens for the secondary stream flow.

3.2.2. Temperature Measurement

Two sets of thermo couples were used to record the temperature across the radial direction for the upstream and downstream sections of the dilution test section. First, the upstream section has six thermocouples distributed along the radial direction at a separating distance of 3.8 cm. This measurement technique takes advantage of the flow and heat transfer symmetry in this case. One more thermo couple is installed at the annulus cold section to record the cold stream temperature, and the result is corroborated with ambient temperature measurements by the Fluke 922 Micromanometer. Five (5) thermocouples are installed 20 cm before the exit of the mixed stream pipe. These thermocouples are installed with an even distribution along the radial direction, with a separation distance of 2.5 cm**. Figure 7** shows the installed thermocouples along the threaded rod for the outlet pipe.

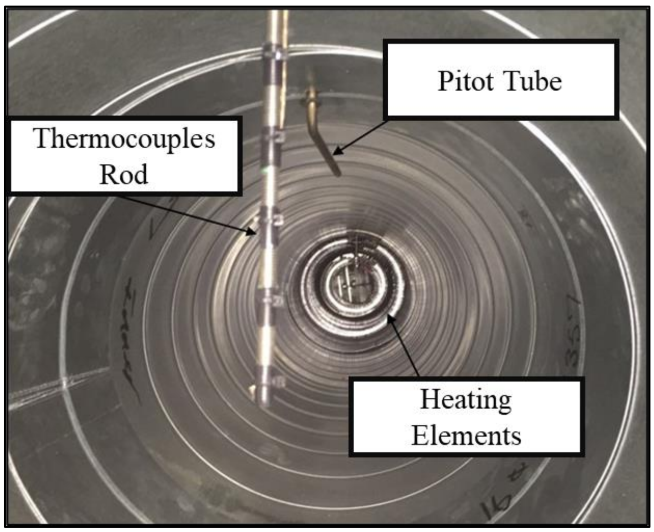

Figure 7: Downstream measurement location in the experimental rig

All thermocouples are of Modine 30-gage Ni-Cr K-type with a reported uncertainty within 2.2^{o}C. The thermocouples are connected to two 8-channel OMEGA data acquisition systems. The thermocouples are calibrated before each experimental run via the InstaCal V 6.73 software with a calibration accuracy of 0.25^{o}C, and the recorded data are accessed via the DAQami V 4.2.1 software, both of which licensed by the Measurement Computing Corporation (MCC). **Figure 8** shows the OMEGA data acquisition system, while **Figure 9** shows the user interface of the software used to calibrate the thermocouples.

Figure 8: Omega 8-channel data acquisition system *[35]*

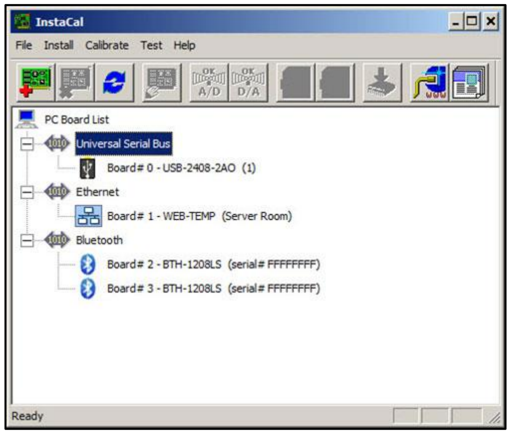

Figure 9: InstaCal calibration software *[36]*

3.3. Testing Procedure

An experiment run starts with recording the ambient temperature via the Fluke 922 Micromanometer. The barometric pressure is also recorded for the testing site via the National Weather Service website [37]. The ambient temperature is recorded every 30 minutes throughout the experiment, and the recorded values are averaged. All 12 thermocouples are calibrated at the beginning of experiments via the InstaCal software. After calibrating the thermocouples and recording the ambient temperature and pressure values, the volume dampers are adjusted based on the required flow specifications. Then, the fan and the heating elements are switched on. After that, the same conditions are maintained for about 30 minutes to ensure that steady state is attained. Then, measurements of the static and total pressure are taken at the upstream section for 7 locations along the radial direction. After that, the same static and total pressure measuring procedure is applied for the pitot tube at the downstream (outlet pipe) position. Then, the temperature recording is taken for the 6 thermocouples distributed along the radial direction at the upstream primary flow section, as well as for the one thermocouple for the upstream secondary flow annular section. Finally, the same temperature recording procedure is used for the 5 radially distributed thermocouples along the radial direction for the outlet pipe.

3.4. Experimental Cases

Experimental runs are conducted to establish a benchmark for comparison and validation of CFD simulations. The first run is performed to establish a baseline, in which the dilution section geometry is unmodified. The second run is performed to establish a baseline for the jet extender geometry, in which the length of the jet extender is 20 mm, and the diameter matches that of the large dilution holes (5 cm). It should be noted that for the cases of jet geometry modifiers, the modifier pieces for the jet extender are installed on the second array of 16 large dilution holes. **Figure 10** shows one piece of the geometry parts, and **Figure 11** shows the installation of geometry parts on the dilution holes in the experiment rig.

Figure 10: dilution hole jet extender

Figure 11: Dilution hole nozzle jet area modifier

As for the experiment conditions, the volumetric damper is opened fully to allow for full flow conditions, which resemble the required flow split of 45% and 55% for the primary (hot stream) and secondary (cold stream) flows, respectively. The heating elements are operated at full capacity for all cases to increase the primary (hot stream) flow temperature as much as possible. The secondary (cold stream) flow temperature is maintained at ambient temperature. Each experimental run follows the same procedure as outlined in **section 3.3**. It should be noted that the inlet (hot stream) flow temperature varies slightly based on the ambient conditions on the experiment run day. Also, the flow coming from the air blower is uniform, and due to the relatively short travel time, the primary (hot stream) flow and secondary (cold stream) flow are both mostly uniform. The barometric pressure also varies slightly across experimental run days. Therefore, there is a slight variation in the velocity measurements as it is based on pressure measurements that are influenced by the barometric pressure.

3.5. Analysis Procedure

As outlined in **section 3.2.1**, the velocity profiles at the inlet sections are calculated through pressure measurements across the radius of the primary flow pipe and the secondary flow annulus. According to experimental measurements, the velocity profiles at the inlet sections are found to be fairly uniform, which warrants assuming a velocity inlet boundary condition and constant flow properties across the inlet cross section. The mean axial velocity is determined through integrating the mass flux across the cross-sectional area of the inlet sections, as shown by **equation (1)**. The average temperature at the inlet boundaries is evaluated via the integral of the thermal energy across the cross-sectional area, as shown by **equation (2)**. The velocity and temperature profiles are benchmarked using the ideal values by evaluating the mass and energy conservation formulations, provided by **equation (3)** and **equation (4)**, assuming there are no significant changes in potential and kinetic energies.

$$\dot{m} = \int_{A_c} \rho v(r,x) dA_c \approx 2\pi \int_0^R v(r,x) r dr = \rho V_a A_c \tag{1}$$

$$\dot{q} = \int_{A_c} \rho v C_p T dA_c = \dot{m} C_p \bar{T} \tag{2}$$

$$(\rho V_a A)|_p + (\rho V_a A)|_s = (\rho V_a A)|_m \tag{3}$$

$$(\dot{m} C_P \bar{T})|_p + (\dot{m} C_P \bar{T})|_s = (\dot{m} C_P \bar{T})|_m \tag{4}$$

The mean velocity and mean temperature are calculated by **equation (5)** and **equation (6)**, respectively. The density is calculated by the ideal gas law, given by **equation (7)**.

$$v_m = \frac{\int_{A_c} \rho v(r,x) dA_c}{\rho A_c} = \frac{2}{R^2} \int_0^R v(r,x) r dr \tag{5}$$

$$T_m = \frac{\int_{A_c} \rho v c_p T(r,x) dA_c}{\dot{m} c_p} = \frac{2}{v_m R^2} \int_0^R v T(r,x) r dr \quad \textbf{(6)}$$

$$\rho = \frac{P}{R_{air} T} \quad \textbf{(7)}$$

Where, ρ is the density, A_c is the cross sectional area, c_p is the specific heat capacity at constant pressure, and R is the pipe radius. P is the pressure, R_{air} is the specific gas constant for air (287.05 $J \cdot kg^{-1} \cdot K^{-1}$), and T is the temperature in Kelvin.

The mixture fraction (f) is used to quantify the discrepancy of the primary stream temperature profile relative to the equilibrium temperature, as shown by **equation (8)**. Such that, f is evaluated at every thermocouple point along the radial direction. The same equation is used to evaluate the equilibrium mixture fraction (f_{eq}) by plugging the equilibrium temperature (T_{eq}) in **equation (8)**, which will be used later to normalize temperature uniformity gains for different flow conditions.

$$f = \frac{T - T_s}{T_p - T_s} \quad \textbf{(8)}$$

The temperature uniformity along the radius span of the outlet pipe is quantified using the normalized mixture fraction (f^*), which reflects the discrepancy between the mixture fraction of measured temperatures and the ideal mixture fraction of equilibrium temperature. The normalized mixture fraction is given by **equation (9)**. When plotting (f^*) versus the normalized radius, a steep profile of (f^*) represents high temperature difference between the pipe wall and the pipe center. Ideally, higher temperature uniformity along the radial direction is attained when two conditions are present. First, a smaller temperature difference between the pipe wall and pipe center. Second, a smaller difference between the measured temperatures and the equilibrium temperature.

$$f^* = \frac{f - f_{eq}}{f_{eq}} \quad \textbf{(9)}$$

The temperature uniformity index [38] (λ_T), given by **equation (10)**, is a scalar quantity defined to quantify the distribution of temperature values across a surface. If the temperature is uniform across the surface, then the temperature uniformity index is equal to 1. Generally, Lower values of the temperature uniformity index is an indication of a low temperature uniformity across the surface.

$$\lambda_T = 1 - \frac{\sum \left| T_f - \bar{T} \right| A_f}{2|\bar{T}| \sum_f A_f} \tag{10}$$

Where, $\bar{T}$ is the surface average temperature, $T_f$is the temperature value at each individual surface mesh face, and A_f is the area of the surface mesh face.

The usefulness efficiency (η) [22], given by **equation (11)**, gives insights into the net effect of the design while considering the change in temperature uniformity and the added pressure drop.

$$\eta = \frac{\lambda_T|_{baseline} - \lambda_T}{1 - \lambda_T|_{baseline}} \Bigg/ \left(\frac{\Delta P|_{baseline} - \Delta P}{\Delta P|_{baseline}} \right)^2 \tag{11}$$

Where, λ_T is the temperature uniformity index, and ΔP is the pressure drop. The usefulness efficiency shows the relevance of the magnitude of power loss represented by ΔP, which is significant for the cost efficiency definition. The usefulness efficiency is used as a relative metric to compare different designs, where higher values indicate a notable temperature efficiency gain to the incurred power loss.

3.6. Experimental Uncertainty and Errors

The experimental error was estimated by considering the uncertainties of the measuring devices, which were obtained from the manufacturer's specification sheets. The error in the thermocouple measuring device is 2.2 ^{o}C and the error in the pressure measuring device is 1% $\pm$ 1 Pa. Therefore, the error in the inlet and outlet pressure for each individual point measurement is given by **equation (12)**.

$$\delta P = \sqrt{(0.01 \times P_i)^2 + 1} \tag{12}$$

Where, P_i is the pressure value at the measuring point. The velocity is calculated at each measurement point by using the dynamic pressure measurement along with the calculated density at the temperature point. Therefore, the velocity at each point along the radius is calculated by **equation (13)**.

$$v_i = \sqrt{2 \times Pd_i/\rho_i} \tag{13}$$

Where, Pd_i is the dynamic pressure measurement, and ρ_i is the density value at the measurement point. Therefore, the error in the velocity measurement at each measuring point is given by **equation (14)**.

$$\delta v_i = \sqrt{\left(\frac{\partial v}{\partial Pd}\delta Pd\right)^2 + \left(\frac{\partial v}{\partial \rho}\delta \rho\right)^2 + (\delta v_r)^2} \tag{14}$$

Where, $\frac{\partial v}{\partial Pd}$ is the partial differential of velocity in terms of dynamic pressure, δPd is the error in dynamic pressure, $\frac{\partial v}{\partial \rho}$ is the partial derivative of velocity in terms of density, $\delta \rho$ is the error in density, and δv_r is the error due to uncertainty in measurement location.

The mean velocity and mean temperature are calculated by **equation (5)** and **equation (6)**, respectively. Therefore, the error in the mean velocity is given by **equation (15)**, and the error in mean temperature is given by **equation (16)**.

$$\delta v_m = \sqrt{\sum\left(r_{avg}.v_{avg}.\Delta r.\sqrt{\left(\frac{\delta r_{avg}}{r_{avg}}\right)^2+\left(\frac{\delta v_{avg}}{v_{avg}}\right)^2+\left(\frac{\delta\Delta r}{\Delta r}\right)^2}\right)^2} \quad \textbf{(15)}$$

$$\delta T_m = \sqrt{\sum\left(r_{avg}.v_{avg}.T_{avg}.\Delta r.\sqrt{\left(\frac{\delta r_{avg}}{r_{avg}}\right)^2+\left(\frac{\delta v_{avg}}{v_{avg}}\right)^2+\left(\frac{\delta T_{avg}}{T_{avg}}\right)^2+\left(\frac{\delta\Delta r}{\Delta r}\right)^2}\right)^2} \quad \textbf{(16)}$$

Where, r_{avg} is the average radius between the discretized points, given by $0.5 \times (r_{i+1} + r_i)$, and v_{avg} is the average velocity between the discretized points, given by $0.5 \times (v_{i+1} + v_i)$, and Δr is the radius difference between the discretized points. **Table 1** provides a summary of the measurement devices errors and the corresponding errors in the calculated values.

Table 1: Summary of error values in measured and calculated values

Item (x)	**Scope**	**Error Value (δx)**	**Error Percentage**
Temperature (T_i)	Measured	2.2 ^{o}C	4.5% - 7.1%
Pressure (P_i)	Measured	1% $\pm$ 1 Pa	2% - 7%
Density (ρ_i)	Calculated	0.058 – 0.087 kg.m^{-3}	5.1% - 7.6%
Velocity (v_i)	Calculated	1.034 – 1.135 m.s^{-1}	6.6% - 8.8%
Mean Velocity (v_m)	Calculated	0.082 m.s^{-1}	0.59%
Mean Temperature (T_m)	Calculated	1.429 ^{o}C	4.00%

CHAPTER 4 – COMPUTATIONAL METHODS AND PROCEDURES

4.1. CAD Geometry Design and Input Parts

The testing rig CAD model is designed using the Star-CCM+ 3D CAD Modeler tool, and starts from a portion of the upstream section that is located before the test section all the way to the end of the outlet pipe. The CAD model is a to-scale replica of the testing rig, for which the sections and dimensions are outlined in **section 3.1**. **Figure 12** shows the 3D CAD model.

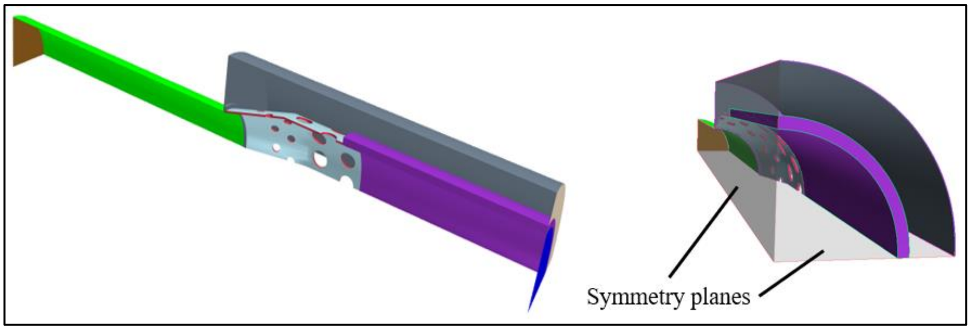

Figure 12: CAD geometry based on symmetry plane division

As shown in **Figure 12**, the geometry is designed to take advantage of the two available symmetry planes in order to reduce the mesh cell count and therefore, the computational costs. Also, **Figure 13** shows the transformed 3D model based on the symmetry planes.

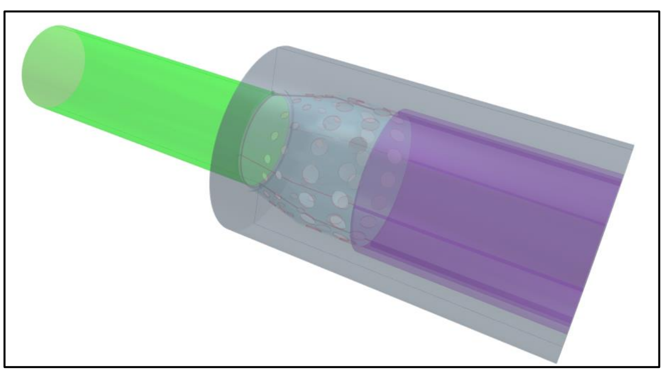

Figure 13: CAD model with 3D transformation using the symmetry planes

The outlined 3D CAD model is the representation of the solid geometry of the testing rig. In order to simulate the fluid flow in the computational domain, the complementary fluid region must be generated. Extracting the fluid volume can be achieved via the Surface Wrapper operation of

Star-CCM+, which creates triangular tessellation surface domain around the CAD surface and extracting the largest internal volume, which corresponds to the fluid region. Several aspects need to be considered to achieve a valid and acceptable surface wrap. First, the cell size must be small enough to capture the nuances and minute details of the geometry. Second, surface curvature capturing parameters need to be tuned to allow for following the circular geometry of the 3D CAD model. Finally, proximity refinement is required to add more surface cells around steep angled geometries and close proximity surfaces. Several metrics are used to assess the adequacy of the wrapped surface including the deviation distance and face quality parameters. The deviation distance is a measure of the closeness of the wrapped surface compared to the original tessellated 3D CAD model. Hence, a smaller deviation distance corresponds to a closely wrapped surface with no significant deformities to the original 3D CAD model. The face quality metric is a measure of the quality of the tessellation triangle, and Star-CCM+ calculates it by **equation (17)**.

$$Face\ Quality = 2 \times r/R \qquad \textbf{(17)}$$

Where, r is the triangle inradius, and R is the triangle circumradius. **Figure 14** illustrates the tessellation triangle radii parameters.

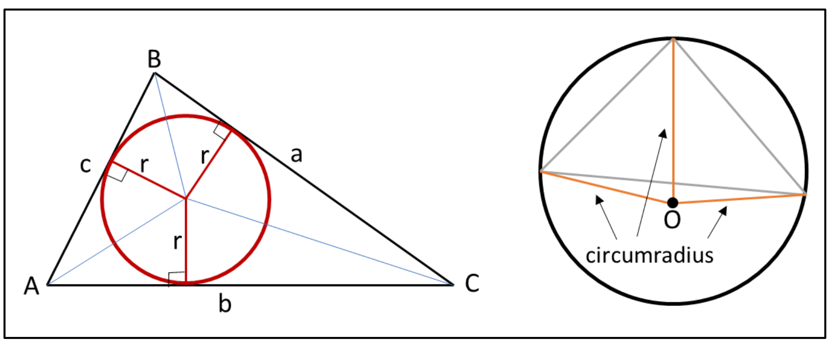

Figure 14: Tessellation triangle inner circle and circumcircle

A higher face quality metric corresponds to a less distorted tessellation triangle, and therefore, higher face quality metrics values are sought after in order to generate a reliable surface tessellation. The face quality parameter is especially important around curved, holed, and complex geometries in order to capture the geometry details with minimal distortion.

Based on the discussed surface tessellation parameters, the wrapping procedure was tuned to yield acceptable quality results. Therefore, the surface tessellation triangle size was set to vary between 0.7 mm to 7.0 mm. Also, the surface curvature was constructed using a minimum of 90 points up to 360 points along any circular section circumference. Finally, surfaces with proximity of at least 1 cm are given extra attention by adding at least 8 surface tessellation triangles across their shared edges. The result of the extracted fluid volume tessellation is presented by **Figure 15.**

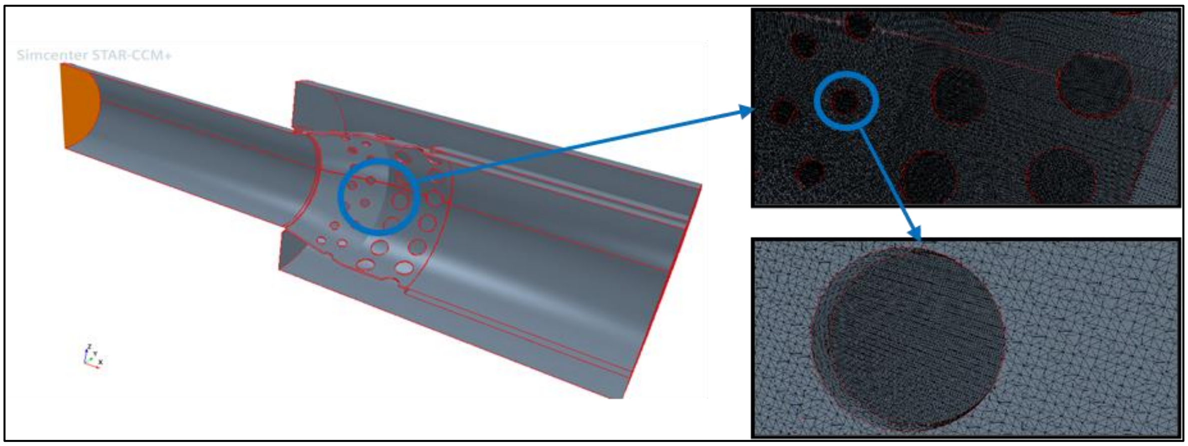

Figure 15: Extracted fluid volume surface wrapper tessellation

The quality of the fluid volume tessellation is checked and reported by **Figure 16** and **Figure 17** which show the tessellation deviation distance and face quality, respectively.

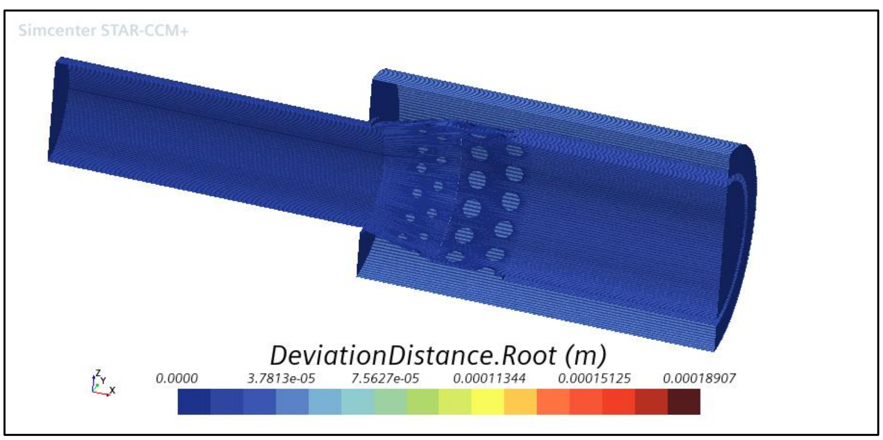

Figure 16: Surface wrapper deviation distance quality metric

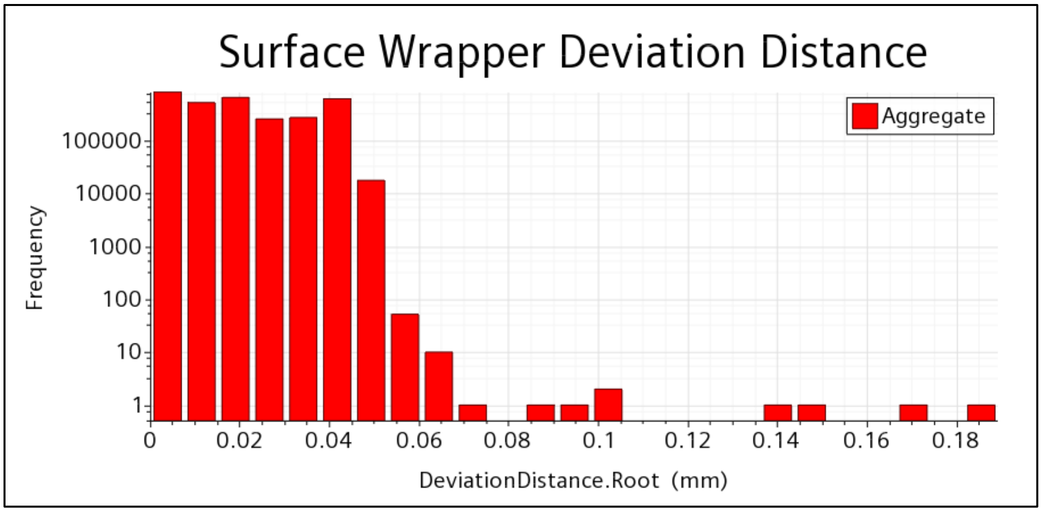

Figure 17: Surface wrapper face quality metric

The extracted fluid region possess acceptable quality metrics as the deviation distance is below the 0.2 mm mark for the majority of the faces, and the face quality metric shows a superior accuracy, such that most of the faces have scores very close to the perfect score (1.0). Therefore, the fluid region surface tessellation is accepted with a total face count of 3,571,730 tessellation faces.

4.2. Meshing Models and Procedures

Volume meshing corresponds to dividing the 3D computational domain into any number of small cells, which is necessary to discretize the computational domain to be able to solve the continuous Navier-Stokes equations of momentum and energy transfer. In this study, Star-CCM+ software is used to generate a volume mesh using the finite volume method. Also, the surface mesher tessellation is based on enhanced quality triangles that spawn across the fluid volume region and fill in the gaps across complex geometry shapes. The volume mesh is generated using polyhedral cells for its efficiency and ability to generate quality cell distribution in unstructured meshes, which is useful for this case to capture the complex geometries. Adaptive and custom meshing is later employed to tailor the volume mesh so that higher cell count of appropriate cell sizes is spawned around walls and complex geometries, and where larger cells sizes are left for the core of the main flow domain away from the walls. This technique enables us to accurately resolve the governing equations around special geometries and close to the walls where the no slip condition is employed and the velocity gradient is usually very steep for turbulent flows. Prism layers (or inflation layers) are crucial to accurately resolve the velocity gradients in the extreme vicinity to the walls. Even if the main flow is turbulent, the boundary layer near the wall is composed of different regions as **Figure 18**.

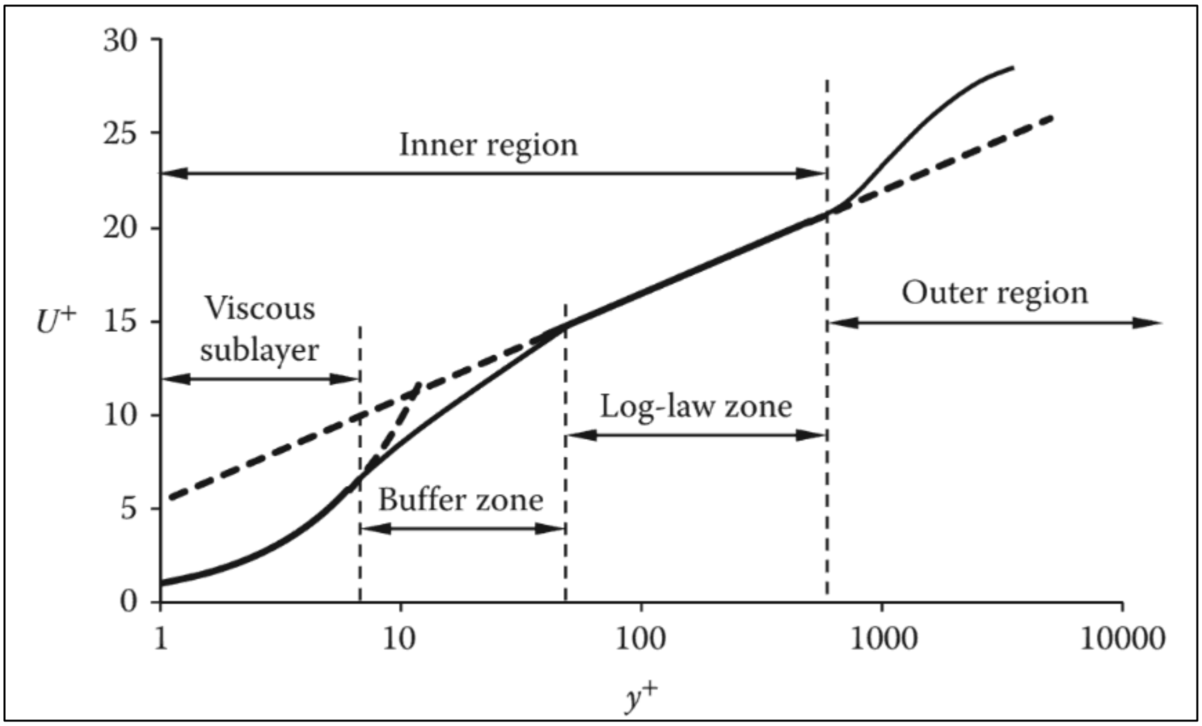

Figure 18: Velocity variation in the turbulent boundary layer over a flat plate *[39]*

In fact, the boundary layer is composed of a viscous sublayer, buffer layer, and logarithmic layer. The boundary layer extends beyond the logarithmic layer to blend in with the main turbulent flow field as part of the outer turbulent region of the boundary layer. In the viscous sublayer, the viscosity effects are dominant as the fluid in that space is very close to the wall. Therefore, this layer can be designated as being laminar in nature. In general, the mean flow velocity within this layer is a function of the layer viscosity, density, wall roughness, and normal distance measured from the wall. This region requires a lot of attention as the velocity gradients for turbulent flows are extremely steep, and requires small cell sizes with high aspect ratios to capture these velocity gradients accurately. The buffer layer and the turbulent logarithmic layer are present in the respective order after the viscous sublayer. The first is where the fluid undergoes transition between the laminar regime in the viscous sublayer to the logarithmic layer, where the flow is equally characterized by both its viscous and turbulent nature. Then, the logarithmic layer is where turbulence dominates, such that the flow field variables change relatively slower than the previous regions in accordance with a logarithmic curve, hence the name of this layer. The Wall Y+ concept is devised to characterize the nature of the fluid regime near to the walls and guide the selection of the turbulence model as well as the wall treatment procedures, which will be discussed shortly. The Wall Y+ can be thought of as the Reynolds number at a specified distance away from the wall towards the core of the flow field. The formula for the Wall Y+ is generally given by **equation (18)** [39]**.**

$$y_+ = \frac{\rho u^*}{\mu} y \tag{18}$$

Where, ρ is the fluid density, μ is the dynamic viscosity, y is the distance from the wall, and u^* is the friction velocity (or velocity scale) which can be calculated using the standard wall functions and the non-iterative method by **equation (19)** or **equation (20)** for the viscous sublayer and the logarithmic layer, respectively [39].

$$u^* = \left[\frac{\mu}{\rho y} |V_t|\right]^{0.5} \tag{19}$$

$$u^* = C_\mu^{0.25} k^{0.5} \tag{20}$$

Where, V_t is the tangential velocity near the wall, c_μ is turbulence model coefficient, and k is the Von Karman constant. It should be noted that the velocity scale can be solved using an iterative method, where the friction velocity is directly estimated from the tangential velocity within the viscous sublayer. As for the logarithmic layer, a log empirical correlation can be used to estimate the friction velocity. However, blended wall functions are usually employed to be able to duly resolve the velocity gradients across the boundary layer throughout all regions of viscous, transition, and turbulent regimes. The blended wall functions are a hybrid technique by which we simultaneously use the known wall functions along with the wall modeling strategy, which relies on modeling the turbulent viscosity as in the case for RANS $k-\varepsilon$ and $k-\omega$ models. The blended wall approach uses the wall modeling strategy in the close proximity of the wall to gain higher accuracy over the traditional wall functions. The blended wall approach employs the traditional wall functions in the further regions away from the wall, where typically, the traditional wall functions are relatively more applicable and produce better results. The blended wall functions are commonly based on Reichardt's law [40] and are given by Equations **(21)** through **(24)**.

$$u^* = \frac{1}{k}\ln(1+ky^+) + C\left(1 - e^{-\frac{y}{y_m^+}} - \frac{y^+}{y_m^+}e^{-by^+}\right) \quad \textbf{(21)}$$

$$C = \frac{1}{k}\ln\left(\frac{E'}{k}\right) \quad \textbf{(22)}$$

$$b = \frac{1}{2}\left(\frac{y^+k}{C} + \frac{1}{y_m^+}\right) \quad \textbf{(23)}$$

$$y_m^+ = max\left(3{,}267(2.64-3.9k){E'}^{1/80}\right) - 0.987 \quad \textbf{(24)}$$

However, in practice, a special type of mesh cells is employed near the wall to enable accurate resolving of velocity gradients, which are steeper in the direction normal to the wall and in the direction of the core flow field. This implies that these cells must satisfy two criteria. First, we can take advantage of a high aspect ratio, in which the cell span is longer in the direction of the flow. Second, these cells must be small enough to accurately model the steep velocity gradients, especially in the viscous sublayer. Therefore, the prism layer (or inflation layer) cell concept emerges. Prism layers are high aspect ratio and typically smaller cells (Relative to those in the flow field), and exists in the vicinity of the wall. Also, prism layers are a group of cells layered on top of one another spawning from the wall and outwards toward the core flow field, hence the naming. Therefore, and in general, there are three parameters that are used to set forth the construction of these prism layers in the volume mesh. First, the first prism layer cell thickness (δ_{min}) which needs to be small enough to reside within the viscous sublayer to capture the steep velocity gradient [41] and relay information to the next prism layers which uses blended wall functions to build the remainder of the velocity profile within the boundary layer. Second, the number of prism layers (N), which needs spawn enough across the boundary layer to at least capture the viscous sublayer and some of the logarithmic layer, where the viscous effects are still in play. Third, the geometric propagation factor (G), which governs the increased spacing or distance from one prism layer to the next. The geometric propagation factor and the number of prism layers are used in tandem to construct the prism layers to have enough thickness and reasonable spacing so that the viscous sublayer and at least a portion of the logarithmic layer are duly captured. In general, **equation (25)** is a simple geometric progression formula that relates the prism layer construction parameters.

$$L = \delta_{min} \frac{(1 - G^N)}{(1 - G)} \tag{25}$$

The prism layer geometric propagation also serves the crucial purpose of blending these smaller cells with the larger cells that typically exists within the main flow field. Failure to do so results in meshes with low quality such that the volume change from one cell to the other is abrupt and too large, which results in solution inaccuracies and most often than not, results in the divergence of the numerical solver. **Figure 19** shows the prism layers used in the following mesh independence studies, with 15 prism layers, total thickness of 1 mm, and a propagation factor of 1.3.

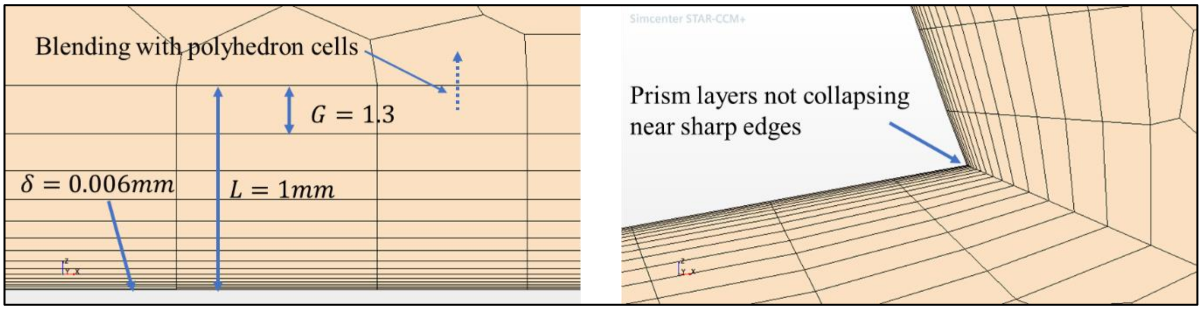

Figure 19: Prism layer construction

As outlined in this section, the use of blended wall functions allows us to resolve the velocity gradients across different regions via multiple equations, each suitable for the region it treats. Based on the All-Wall Y+ Treatment approach taken in this study, the wall Y+ values should generally be outside of the range 5 < Y+ < 30, as this range belongs to the transitional region [41], where the viscous and turbulent effects are equally important. To have confidence in the prescribed treatment approach, we need to maintain a Wall Y+ values in either the low or high ranges, as long as it is outside of the transitional region.

4.3. Boundary Conditions

Setting the right boundary conditions is a crucial step in any CFD simulation. As discussed in **section 4.1**, the CAD geometry was designed to take advantage of two accessible symmetry planes. The inlet and exit boundary conditions are set up to enable using experimental data for validation. The fluid region contains six different boundary conditions of hot or primary stream inlet section (velocity boundary condition), cold or secondary inlet stream (velocity boundary condition), mixed stream exit section (pressure outlet boundary condition), wall boundary conditions near the solid walls, and two symmetry plane boundary conditions. **Figure 20** shows the six different boundary conditions used to set up all simulation studies.

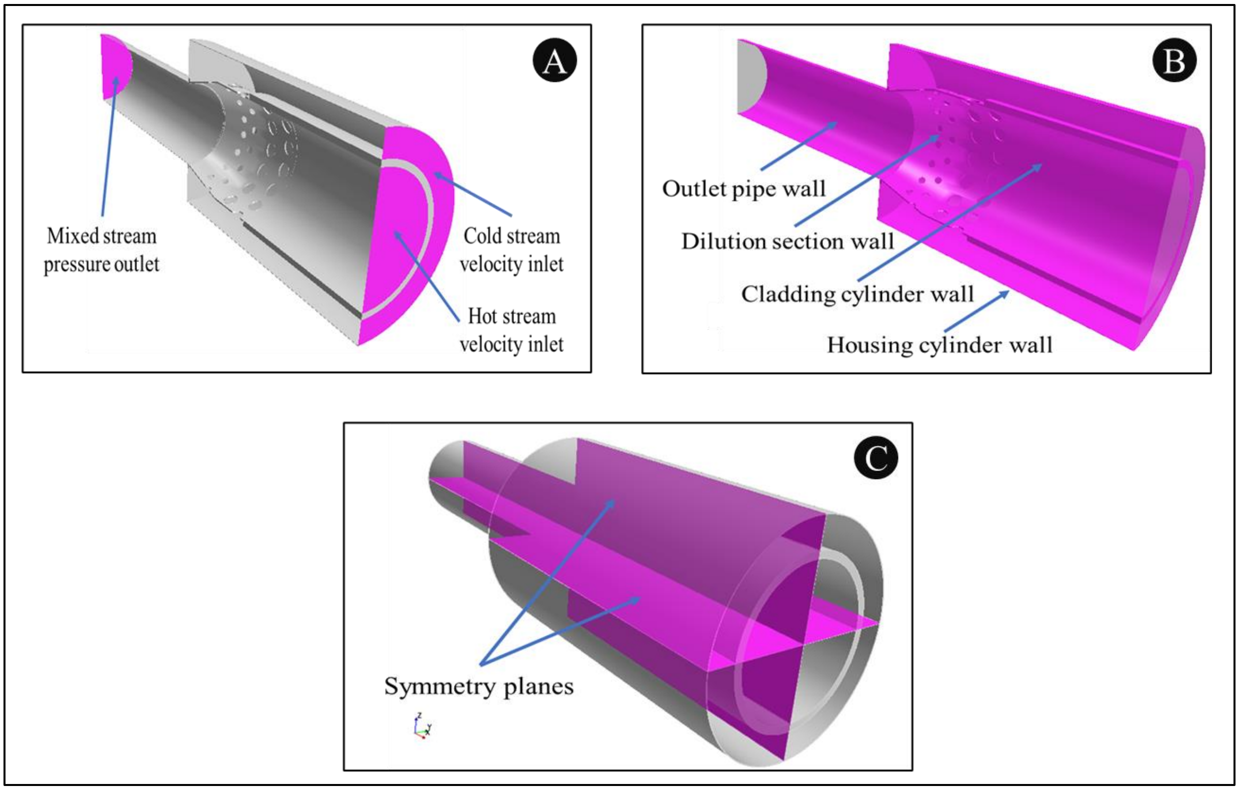

Figure 20: Boundary conditions on half cross section with symmetry plane transformation. (A) Flow inlet/exit boundary conditions, (B) Wall boundary conditions, (C) Symmetry planes boundary conditions

For the mesh independence studies and the validation studies, the inlet velocity profiles are set up according to the calculated inlet velocities from experimental data, which is found to be generally uniform for the hot stream and cold stream inlet sections. The wall boundary conditions represent the adjacent fluid layers near the solid walls, these boundaries are set up with the assumption of adiabatic thermal specification. The main reason behind this assumption is that the hot stream is insulated all the way before the test section with a glass wool insulation of 2.54 cm thickness. Then, the hot and cold streams meet in the test section which is relatively short compared to the other dimensions of the experiment. Given that, and the high stream velocities, the conduction through the dilution section walls can be ignored as the resident time of either stream is very short within the test section, which is a valid approximation for this case. The surface roughness for the wall boundary conditions is set to match that of the material used in the experiment rig, which is galvanized steel with a surface roughness of about 0.15 mm [42].

4.4. Physics Models and Governing Equations

Several CFD models are investigated throughout this study. Mainly to assess the performance of different models, and more importantly, provide an acceptable validation for experimental data while maintaining a reasonable level of complexity and computational costs. As discussed in **section 4.2**, the given 3D CAD model is discretized into smaller 3-dimensional volume cells, 2-dimensional triangular tessellation, and a set of prism layers that grow from the extreme vicinity to the walls in the direction of the main flow field. This discretization in the computational domains allows us to solve the partial differential Navier-Stokes equations, and the supplementary turbulence and pressure equations in the 3D space. The starting point of any fluid flow problem is to understand the Navier-Stokes equations, for which **equation (26)**, **equation (27)**, and **equation (28)** give the generalized tensor form for the continuity, momentum, and energy conservation, respectively [43].

Continuity:
$$\partial\rho/\partial t + (\nabla \cdot \rho v) = 0 \tag{26}$$

Momentum:
$$\rho Dv/Dt = -\nabla p + \mu \nabla^2 v + \rho g \tag{27}$$

Energy:
$$\rho \hat{C}_p DT/Dt = -(\nabla \cdot q) - (\partial \ln \rho / \partial \ln T\,)_p\, Dp/Dt - (\tau : \nabla v) \tag{28}$$

Where, the first term in the continuity equation is the rate of increase of mass per unit volume, while the second term is the net rate of mass addition per unit volume by convection. As for the momentum equation, the first term is the substantial derivative combining the change of velocity with time and the convection term, the second term is for the pressure gradient in the flow field, the third term is the diffusion term, and the last term is for body forces. The first term in the energy equation is for the substantial derivative combining the rate of change in time and by convection transport, the second term is the rate of energy addition per unit volume by heat conduction, the third term is for the total derivative for the rate of work done on the fluid per unit volume by pressure forces, and the last term is for the rate of work done on the fluid per unit volume by viscous forces.

These equations are the pillar of modern fluid dynamics and are used to solve the flow and energy fields while being valid for laminar and turbulent flows. However, solving for the flow field in the laminar regime is much easier as we are afforded a lot of assumptions that allow for a feasible solution, even an analytical one in some situations. Turbulence requires additional care and extra models to be able to resolve the flow field in real-life situations. But first, turbulence can be defined as the chaotic state of flow motion that arises due to disturbances in the flow field. These disturbances are referred to as vortices or turbulent eddies, which are rotational flow structures that come in all shapes and sizes depending on the extent of turbulence and fluid properties. There are different culprits for generating and even amplifying these disturbances. For example, changes in velocity brought by inertial forces results a random motion of some fluid particles or layers, which trickles down the flow field and contribute to turbulence. Another example is the viscous forces that are especially important around blunt or narrowing geometries, which alters the shear stress profile across different fluid layers to ultimately transform the flow from laminar to turbulent. One more example is the surface roughness, which impedes the fluid layers near the object surface, and by which the chaotic motion spreads to the other fluid layers and turbulence is set forth. Interestingly, the last example is a used purposefully in rough golf balls, to transform the air flowing around the ball to the turbulent regime at the same air velocity, and thus, enable the air to traverse further along the backside of the golf ball and allows for a delayed separation. Hence, improving the aerodynamics of the golf ball and allowing it to experience less total drag forces, despite the increased friction forces arising from air traversing more of the ball's surface.

Turbulence is pernicious in nature, in the sense that localized disturbances (or eddies) sap the energy from the main flow field, in which different velocity gradients causes the eddies to deform, which is a process recognized as vortex stretching. As the eddies (or vortices) are deformed, they interact with other fluid layers in the flow field which causes more instabilities to be born, and so on until more localized regions in the flow field are turbulent. This process is called vortex energy cascading, and it affects the flow negatively by extracting some of the energy to feed the rotational structures. Small-scale eddies are mainly governed by the viscous effects, for which the interactions of the small eddies with the main flow field causes the kinetic energy to be dissipated into thermal energy within the flow field.

However, attempting to resolve all eddies in a turbulent flow is one of the greatest undertakings in engineering. Such that, some of the eddies are extremely small and evolve so fast that the required computational domain must be discretized to sizes way beyond the available computing power. This approach is called Direct Numerical Simulation (DNS), and to put things into perspective, the required length scales are extremely small and can easily be in the order of $10\ \mu m$, and the time scales in the order of $100\ \mu s$ [41]. Nevertheless, the engineering ingenuity prevailed by temporarily circumventing these issues via using time-averaged turbulence modeling rather than direct resolving. Through this approach, we can reasonably solve the flow field without focusing our attention on the particularities of individual eddies, and through obtaining solutions that describe the mean flow characteristics and profiles as an average through time. The Reynolds Averaged Navier-Stokes (RANS) model is used in this study, which employs the turbulence modeling through the time-averaged approach for steady state applications.

The model that we need to consider is the RANS $k - \varepsilon$ model. The $k - \varepsilon$ model is used extensively in the Computational Fluid Dynamics (CFD) simulations of industrial applications. The model belongs to the Reynolds-Averaged Navier-Stokes (RANS) family, and it is based on two equations that describe the turbulence kinetic energy (k) and the corresponding dissipation rate (ε). The $k - \varepsilon$ model closure equations are featured in **equation (29)** and **equation (30)** in the two-dimensional cartesian form [41].

$$\boldsymbol{k}: \quad \frac{\partial(\rho k)}{dt} + \frac{\partial(\rho u k)}{\partial x} + \frac{\partial(\rho v k)}{\partial y} = \frac{\partial}{\partial x}\left(\frac{\mu_T \partial k}{\sigma_k \partial x}\right) + \frac{\partial}{\partial y}\left(\frac{\mu_T \partial k}{\sigma_k \partial y}\right) + P - D \tag{29}$$

$$\boldsymbol{\varepsilon}: \quad \frac{\partial(\rho \varepsilon)}{dt} + \frac{\partial(\rho u \varepsilon)}{\partial x} + \frac{\partial(\rho v \varepsilon)}{\partial y} = \frac{\partial}{\partial x}\left(\frac{\mu_T \partial \varepsilon}{\sigma_k \partial x}\right) + \frac{\partial}{\partial y}\left(\frac{\mu_T \partial \varepsilon}{\sigma_k \partial y}\right) + \frac{\varepsilon}{k}(C_{\varepsilon 1} P - C_{\varepsilon 2} D) \tag{30}$$

Where, P is the rate of production of k or ε, and D is the rate of destruction. The turbulent viscosity (μ_T), modeled isotopically, is given by **equation (31)** [41].

$$\mu_T = \frac{\rho C_\mu k^2}{\varepsilon} \tag{31}$$

Where, C_μ is one of the mode's empirical constants, rho is the density, k is the turbulent kinetic energy, and ε is the rate of turbulent energy dissipation. Then, **equation (32)** and **equation (33)** provide the cartesian tensor form for the turbulent kinetic energy and dissipation rate, respectively [41].

$$k = \frac{1}{2} u_i' u_i' \tag{32}$$

$$\varepsilon = \nu_T \overline{\left(\frac{\partial u_i'}{\partial x_j}\right)\left(\frac{\partial u_i'}{\partial x_j}\right)} \tag{33}$$

Given the tensor notation where $i, j = 1, 2, 3$. Also, the eddy viscosity (ν_T) is given by $\nu_T = \mu_T/\rho$. Clearly, one of the model's simplifications is the use of time-averaging. Which entails averaging the flow field over a large number of eddies. As previously explained, this method is utilized to decompose the flow field into its corresponding mean and fluctuating components.

Regardless, this approach is valid in cases where the particularities of the eddies and mixing are not of vital importance, and where the simulation is mainly focused on the averaged flow field features without delineating eddies or turbulence scales. The current study being one example of this application, such that our goal is to approximate the average velocity and temperature profile at steady state conditions, without any particular attention given to the turbulence scales or mixing mechanics. One of the main underlying assumptions of the $k - \varepsilon$ model are isotropy and homogeneity, in which the viscosity and turbulence are assumed to be independent of spatial location or direction. These assumptions allow for the use of scalar transport equations to describe the turbulent kinetic energy (k) and dissipation rate (ε). On the other hand, the $k - \varepsilon$ model comes with its own limitations such as It's limitation to model the flow near the walls and in cases of severe flow separation and transitional flow from the laminar to turbulent regimes. Alternatively, the realizable $k - \varepsilon$ model emerges to improve some of the shortcomings of the standard model, and allow for a robust approach that accommodates more use cases. It is worth noting that the realizable variation in particular is wildly used in the industry due to its reasonable accuracy, limited sensitivity to boundary and initial conditions, and its ability to accommodate adverse pressure gradients and flow separation in a better way as opposed to the standard model variation.

The realizable k-epsilon model uses a modified version of the turbulent viscosity and turbulent dissipation rate, which gives this model an advantage in simulating flows with strong separation and complex geometries. The formulation of the realizable $k - \varepsilon$ model in the cartesian tensor notation is given by **equation (34)**, and **equation (35)** for the turbulent kinetic energy and the dissipation rate, respectively [44] [45] [46].

$$\boldsymbol{k}: \qquad \frac{\partial(\rho k)}{dt} + \frac{\partial(\rho u_i k)}{\partial x_i} = \frac{\partial}{\partial x_j}\left((\mu + \frac{\mu_T}{\sigma_k})\frac{\partial k}{\partial x_j}\right) + G_k + G_b - \rho\varepsilon - Y_M + S_k \qquad \textbf{(34)}$$

$$\boldsymbol{\varepsilon}: \qquad \frac{\partial(\rho\varepsilon)}{dt} + \frac{\partial(\rho u_i \varepsilon)}{\partial x_i} = \frac{\partial}{\partial x_j}\left((\mu + \frac{\mu_T}{\sigma_\varepsilon})\frac{\partial \varepsilon}{\partial x_j}\right) + \frac{C_{1\varepsilon}\varepsilon}{k}(G_k + C_{3\varepsilon}G_b) - \frac{C_{2\varepsilon}\rho\varepsilon^2}{k} + S_\varepsilon \qquad \textbf{(35)}$$

The difference lies in the method of calculating the turbulent viscosity as well as in the generation and destruction terms. Such that, G_k is for the generation of turbulent kinetic energy due to the mean velocity gradients. Also, $G_b$represents the generation of turbulence kinetic energy due to buoyancy forces, Y_M represents the effect of non-homogonous dilatation for compressible turbulent flows. All terms of $C_{1\varepsilon}$, $C_{2\varepsilon}$, and $C_{3\varepsilon}$ are empirical constants of the model, adjustable based on the application. S_k and S_ε represent the source terms. The turbulent Prandtl numbers are given by σ_k and σ_ε for the turbulent kinetic energy and dissipation rate, respectively.

4.5. Numerical Solver, Initialization, and Convergence Criteria

The Computational Fluid Dynamics (CFD) simulations are conducted on Star-CCM+. The numerical solver uses segregated velocity, segregated pressure and segregated energy approach. The velocity under-relaxation factor is 0.7 and the pressure under-relaxation factor is 0.3. The solver uses Algebraic Multigrid (AMG) method, which is very useful in solving large and sparse linear systems. The AMG solver uses Gauss-Seidel scheme with 30 maximum optimization cycles, and a convergence tolerance of 0.1. The realizable k-epsilon ($k-\varepsilon$) turbulence model uses an under-relaxation factor 0.8. The used turbulence coefficients are based on industry standard values [45] [47] [48], where $C_{1\varepsilon}$, $C_{2\varepsilon}$, and $C_{3\varepsilon}$ are equal to 1.44, 1.9, and 0.09, respectively.

The solver uses uniform initialization across the computational domain. The initial velocity value is 4 m/s in the direction of axial flow. The initial static temperature value is the average of hot inlet and cold inlet temperatures.

The solver monitors residuals at every iteration. The solution uses a maximum step stopping criterion of 3,000 iterations, with the aim of allowing residuals to fall below the 10^{-5} mark. The solution is deemed converged when the residuals fall below the prescribed tolerance at the specified maximum iteration criterion. Also, the computational mesh domain is validated against experimental data by comparing the response values (velocity, pressure, and temperature) with the experimental error ranges.

CHAPTER 5 – RESULTS AND DISCUSSION

5.1. Mesh Independence Study

A mesh independence study is performed to ensure that the numerical solution, under the specified physics models, is independent of the mesh discretization. The objective of this study is to select a mesh refinement size that would give us reasonable accuracy and speed without being affected by the higher-order dropped terms in the discretization equation. Several metrics can be used to assess the adequacy of the further refined meshes. First, mesh quality plays a major role in assessing the adequacy of our considered meshes. For example, several metrics such as cell quality, skewness angle, face validity, face quality, and volume change allow us to qualitatively compare different levels of mesh refinement in order to achieve a stable mesh that allows for convergence, which is discussed in more detail in **section 4.2**. Second, comparing the response among different levels of refinement can show us the extent of response change as the mesh becomes more refined. Such that, mesh independence can be validated if the response change becomes more negligible as the mesh becomes more refined. Third, the discretization error can be further investigated by comparing the extents of the response for different levels of mesh refinement against a reference mesh, which is commonly known as the infinity norm. Fourth, mesh independence can generally be assessed by comparing the convergence rate of different levels of refinement, where the convergence rate is faster for a finer mesh under robust models such as that used in this study. Finally, mesh independence can be assessed by comparing the turbulent viscosity profile at different sections of interest, and validating that the profiles change becomes more negligible as we consider finer mesh settings.

The mesh independence study will start with an elementary study by comparing eight (8) levels of mesh cell refinement for the flow baseline case and the jet extender case. The mesh independence study utilizes the realizable k-e model discussed in **section 4.4**, for which we will use the experimental results to validate the numerical models and the mesh refinement response. All meshes are constructed with a minimum prism layer thickness of 0.5 mm at 15 levels of inflation layers and a geometric propagation factor of 1.3. The used settings of the prism layers ensure that the viscous sublayer and at least a notable portion of the logarithmic layer are captured by the 15 levels of inflation layers used. The prism layer settings allow us to obtain a Wall Y+ values of less than 1.0, which is necessary to ensure that the used Two Layer Wall Y+ Treatment model is within the acceptable Wall Y+ values. Finally, the adequacy of the prism layer settings is assessed by visualizing the turbulent viscosity field and ensuring that our prism layers capture the viscous regions while propagating smoothly into the flow field, especially for the finest of meshes. A more detailed discussion on these considerations is furnished in **section 4.2**.

After completing the elementary mesh independence study for the realizable k-epsilon model, one more mesh refinement case is considered by using custom controls that allow for larger cell sizes in the main flow field away from the walls, and smaller cell sizes near the walls and complex geometries. This approach enables us to retain the accuracy of the higher mesh refinement while allowing for reducing the total cell count, which will ultimately result in less computational costs.

Table 2 outlines a summary of the elementary mesh independence study components, where N is the number of prism layers, δ_{Tmin} is the minimum total prism layer thickness, and G is the geometric propagation factor.

Table 2: Elementary mesh independence study scenarios

Index	Model	Target cell size (mm)	Minimum cell size (mm)	Prism layer settings	Cell count
1	Realizable k-ε	12.5	12.5	N = 15, δ_{Tmin}= 1 mm, G = 1.3,	199,300
2		8.839	8.839		385,395
3		6.25	6.25		807,757
4		4.419	4.419		1,755,805
5		3.125	3.125		4,357,545
6		2.21	2.21		11,063,375
7		1.563	1.563		26,286,021
8		1.105	1.105		70,407,171

It is worth noting that the selection of the coarsest size for the elementary mesh study is half the diameter of the smallest dilution hole, which will ensure that the smallest cell is comparable to small geometry dimensions. Otherwise, inaccuracies will arise due to inapplicable mesh cell sizes that cannot reasonably represent the flow field and the simulated geometry. Starting from the coarsest mesh size, the refinement levels are scaled at each level by a factor of $\sqrt{2}$, which is not too aggressive and allows for assessing the adequacy of mesh refinement at reasonable step sizes.

The quality of different mesh refinements is assessed by evaluating different metrics including the cell skewness angle, cell quality, cell face quality, and cell volume change. Therefore, **Figure 21**, **Figure 22**, and **Figure 23** present boxplots for the outlined mesh independence levels volume mesh cell quality, volume change, and skewness angle, respectively.

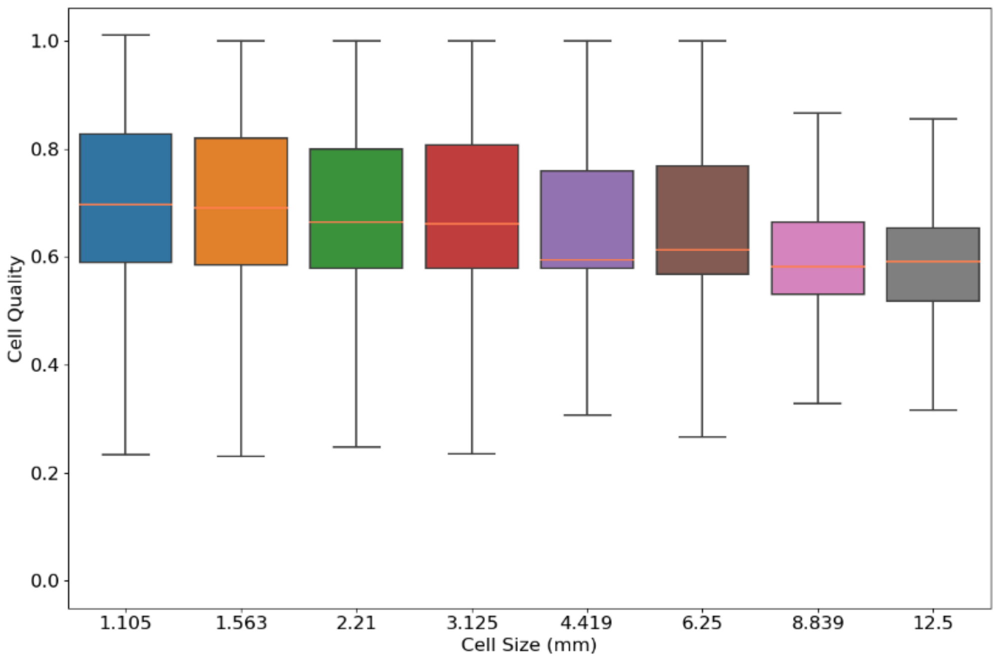

Figure 21: Boxplot for Cell Quality metric for elementary mesh independence study levels

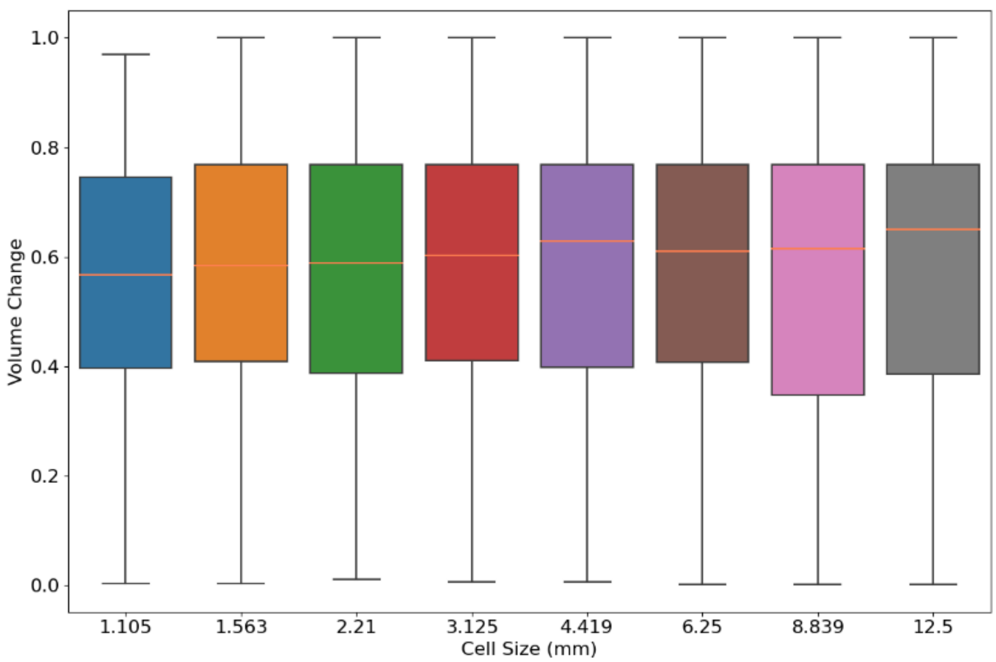

Figure 22: Boxplot for Volume Change metric for elementary mesh independence study levels

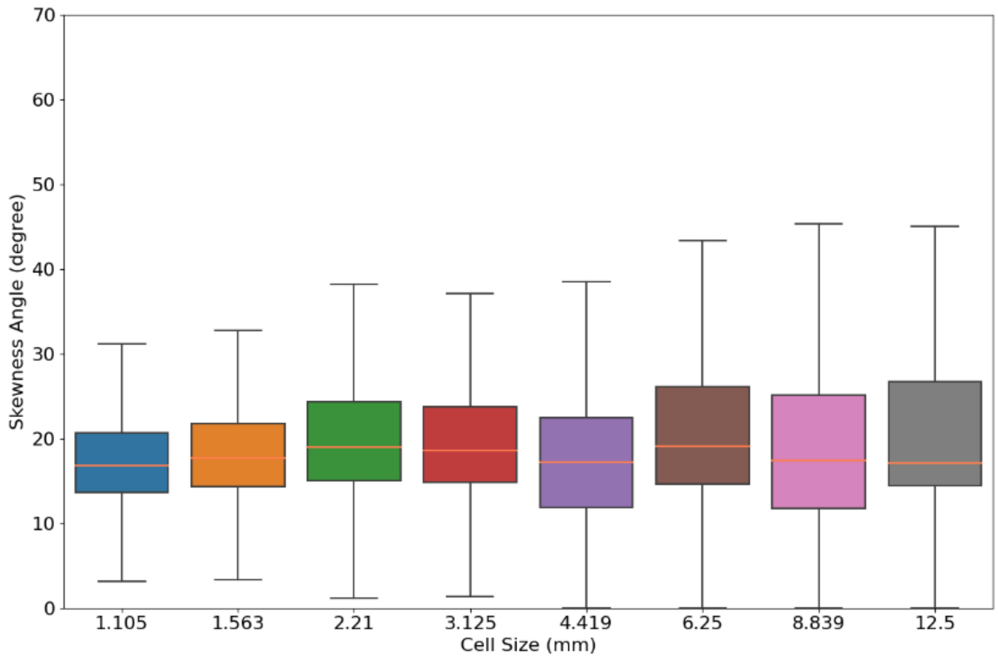

Figure 23: Boxplot for Skewness Angle metric for elementary mesh independence study levels

As seen in **Figure 21**, the cell quality of the volume mesh shows a general trend of improvement as the mesh gets finer. Improvement in the cell quality is characterized by higher concentration of data points on the higher end of the spectrum as well as higher median values. It should be noted that cell quality is a holistic quality metric that gives an overall idea about the validity of volume mesh cells. **Figure 22** outlines the volume change quality metric for different refinement levels. Improvement in the volume change of cells is judged by a higher concentration of data points on the higher end. However, volume change improvement is mainly observed going from a very coarse mesh to the next refinement level, and not much improvement after that level. This is due to two reasons. First, the mesh generator uses 3 optimization cycles to minimize any jumps in volumes among neighboring cells, and consequently improve the volume change metric. Second, the target and minimum cell sizes are identical for all mesh independence levels, which minimizes the chances of having large jumps among neighboring cells. Nevertheless, the focus should be on the interquartile range of the data, which shows a decreasing trend as the mesh is refined further. The volume change of refined cells is within the desirable levels for a valid and numerically stable mesh.

Figure 23 outlines the skewness angle metric for different levels of refinement. Improvement in skewness angle is achieved when the maximum extent (shown by the higher whisker) gets smaller. Improvement is indicated by a reduction in the interquartile range, which shows a better uniformity of datapoints among the mesh volume cells. Evidently, finer meshes demonstrate this trend by possessing lower highs and by having a smaller interquartile range. The minute different in higher extent trend between the last two finest meshes is miniscule, which is the product of needing further topology optimization cycles owing to the large number of cells at the finest mesh level. It is not necessary to obtain a perfect finest mesh, the purpose of these figures is to show a general trend of improvement as the mesh gets finer. Hence, from the preceding quality metric figures, we can observe a general improvement in the mesh topology quality as the mesh gets finer, which is a good indication of mesh stability and a sign of approaching mesh independence. **Table 3** presents the mean values of each of the prescribed quality metrics for all refinement levels, which buttresses the observations noted earlier. Additionally, more figures in the appendix are given to show histograms for the cell quality, volume change, and skewness angle quality metrics.

Table 3: Mean values of quality metrics for the different levels of elementary mesh independence study

cell size (mm)	Mean Cell Quality	Mean Skewness Angle (degree)	Mean Volume Change
12.5	0.57	24.15	0.56
8.839	0.59	21.34	0.54
6.25	0.63	21.72	0.56
4.419	0.63	18.62	0.57
3.125	0.67	20.09	0.57
2.21	0.67	20.18	0.56
1.563	0.69	18.54	0.57
1.105	0.70	17.61	0.56

The flow-averaged velocity and temperature responses at the outlet section are used to compare the response of the elementary levels of refinement as well as assess mesh independence via performing a Richardson extrapolation. The Richardson extrapolation is a numerical technique that is used to evaluate a function at a specified point given the values of nearby points. Which will provide us with information about the response value at the zeroth cell size. The aim of this task is to ensure that the solution becomes independent at higher level refinements. Also, we will obtain the zeroth cell size that corresponds to the ultimate level of refinement, which represents an approximation of the continuous response function. **Figure 24** presents the mean velocity response and the for the different levels of elementary mesh refinement.

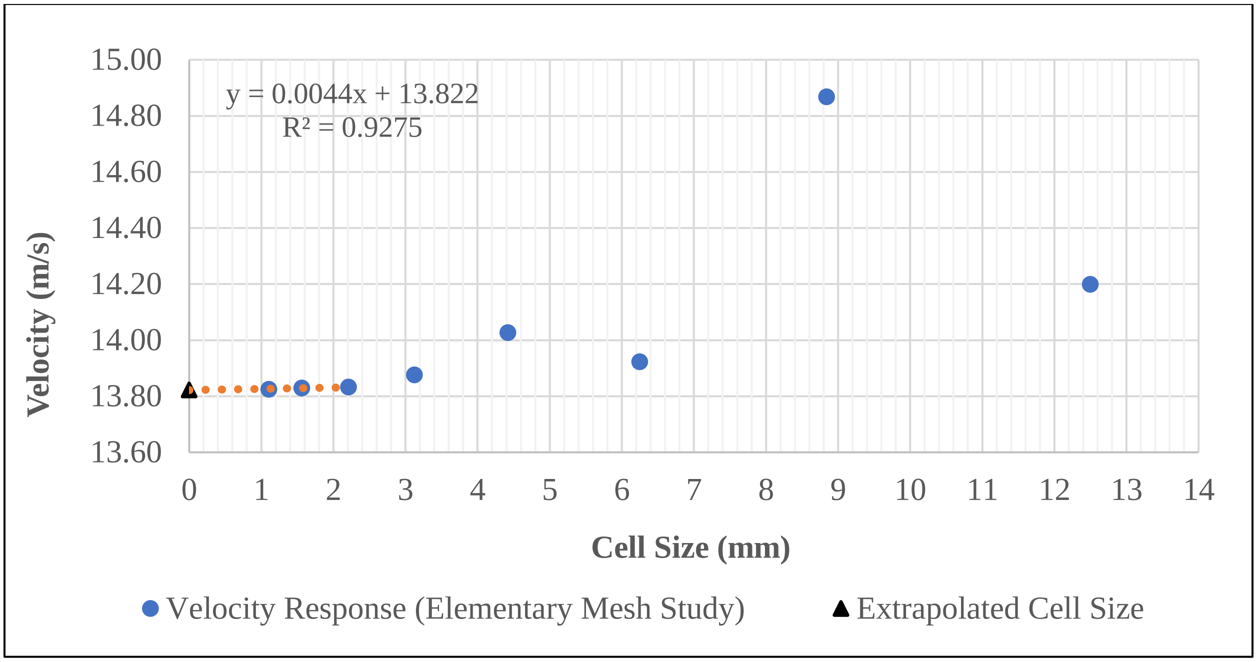

Figure 24: Velocity response across different levels of elementary mesh refinement and the extrapolated zeroth cell size

From **Figure 24**, we can observe that as we increase mesh refinement, the response change diminishes, which is an indication that the solution becomes more mesh independent at higher levels of refinement. We can estimate the zeroth base size response value, which corresponds to 13.825 m/s if we further refine the mesh to an infinitesimal size. It is worth noting that in terms of absolute error, the course meshes are not doing very bad. However, this is because the elementary refinement study took a reasonable coarse mesh size that is commensurate with the smallest geometry scale.

As for the heat transfer response, the temperature profile is evaluated at the downstream section near the exit of the testing rig. The flow-averaged surface temperature at the same location is evaluated for all elementary refinement levels. Results from the elementary mesh study show that the mean surface temperature at the downstream section is within 3.5% for fine refinement levels. That is, we only observe a somewhat notable change in velocity at that location, but the temperature response is very close to the experimental values even at coarser meshes. There are two main factors that may have resulted in this observation. The temperature field depends on the heat transfer process, which is relatively slower as opposed to fluid dynamics. Hence, the change in temperature field response may not be as rapid as that of the velocity field. Second, the already reasonable coarse mesh size may be enough to capture the details of the temperature field governed by the advection and diffusion terms. Therefore, the lower-resolution mesh refinement is enough to capture the heat transfer aspects and is already satisfying the mesh independence at those refinement levels. The error compared to experimental data in the downstream total pressure of the elementary study cases changes from about 9% to 7.5% from the coarsest mesh to the finest, respectively. Resolving the total pressure at different locations requires accurate velocity field solutions and static pressure linkage, which ultimately depend on the cell base size and more importantly on resolving the velocity profile near the walls using prism layers. Also, changes in the total pressure follow the same trend as the changes in the velocity response as we further refine the mesh. Hence, an error in the order of 7% is deemed acceptable, so long as we achieved mesh independence in velocity, temperature, and total pressure.

Figure 25 and **Figure 26** present the response profiles for the finest mesh along outlet pipe normalized radius for the velocity and temperature, respectively. **Figure 27** and **Figure 28** present heatmaps for the finest mesh for the velocity and temperature responses, respectively.

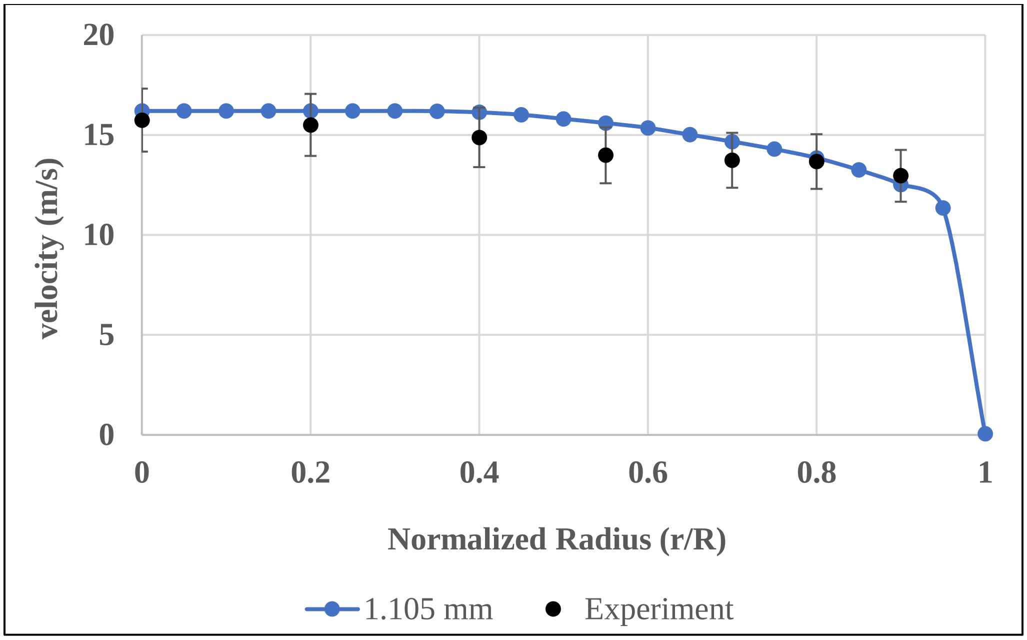

Figure 25: Velocity response along the normalized outlet pipe radius for the finest mesh level

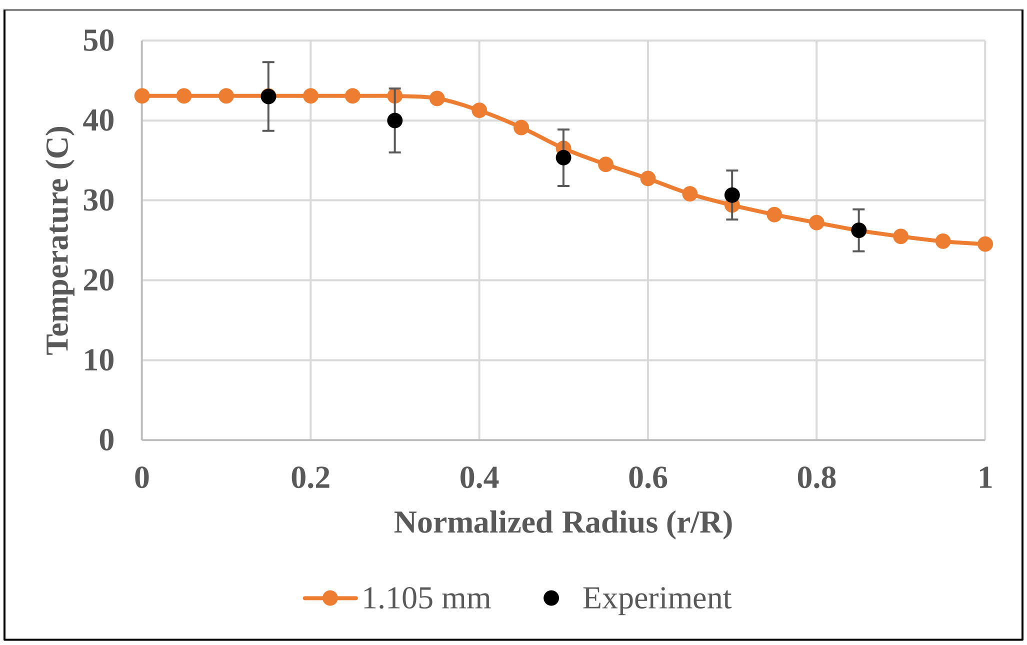

Figure 26: Temperature response along the normalized outlet pipe radius for the finest mesh level

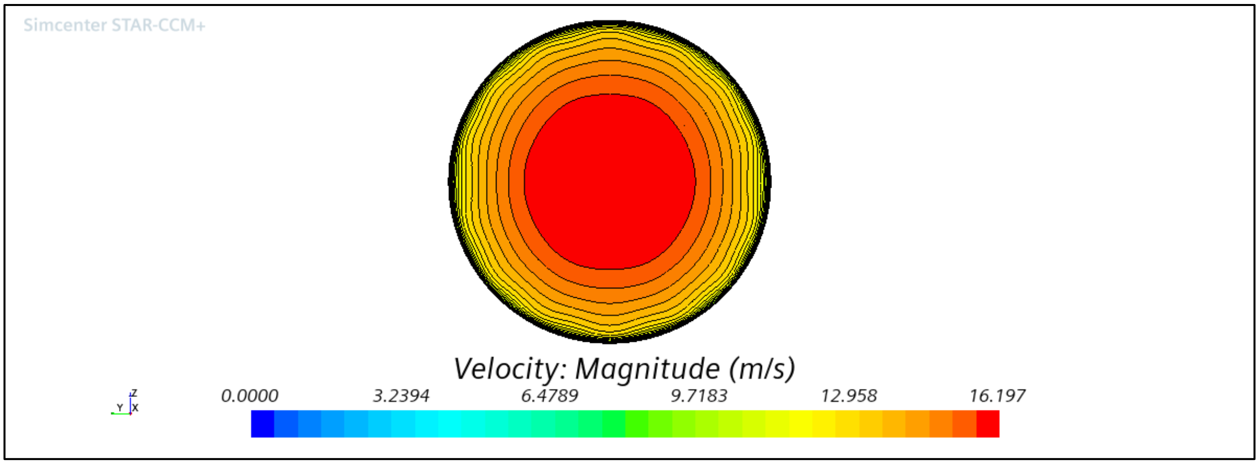

Figure 27: Velocity response on the exit plane for the finest mesh level

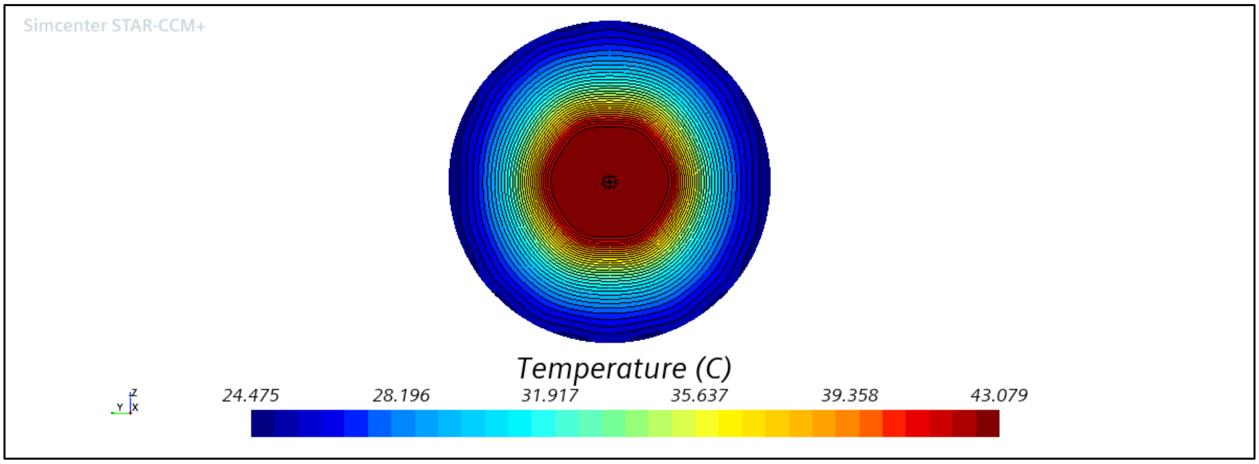

Figure 28: Temperature response on the exit plane for the finest mesh level

The mean temperature error diminishes with finer meshes. The finest mesh attained an error of 2.84% in the mean temperature error. The trendline of mean temperature error is nearly linear as shown by **Figure 29**.

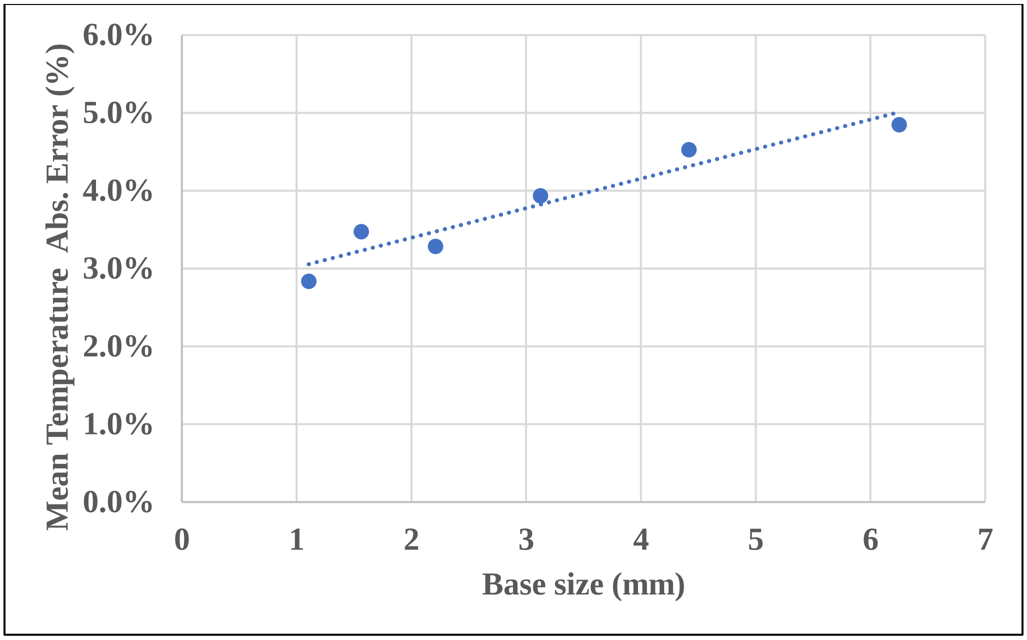

Figure 29: Mean temperature error percentage across different refinement levels within the finer meshes range

All mesh independence studies were performed up to 3,000 iterations to ensure convergence by minimizing residuals and observing stability in the continuity, momentum, energy, and turbulence equations. Residuals for the momentum, continuity, turbulent kinetic energy (TKE) are below 10^{-9}. The residual in the energy equation stabilized at 2×10^{-7}, while the residual for the turbulent dissipation rate (TDR) stabilized at 5.8×10^{-5}. These residual values indicate convergence and a stable solution in all pertinent equations. **Figure 30** shows the residuals plot for the finest mesh.

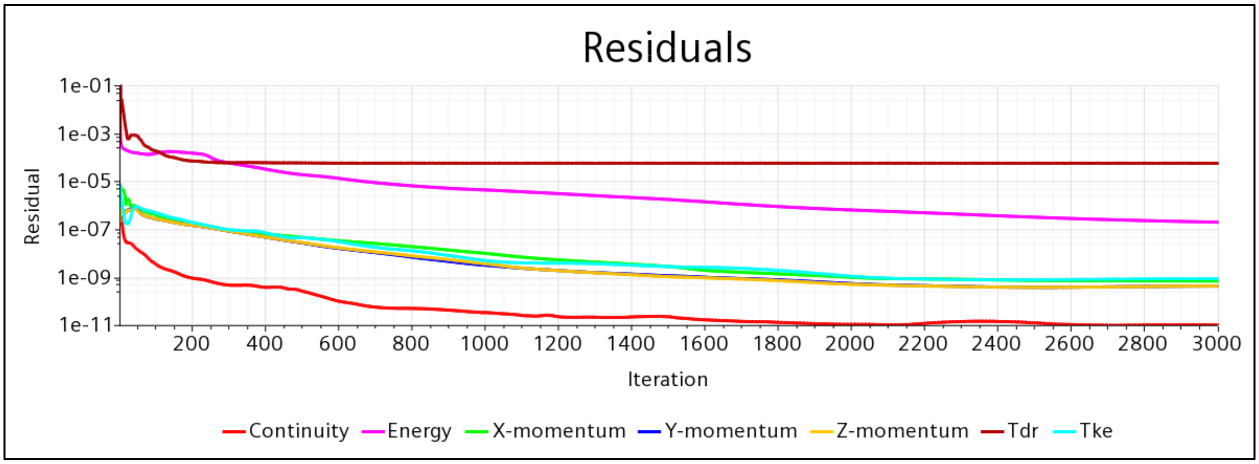

Figure 30: Residuals plot for the finest mesh in the mesh independence study. Presents the residual for the following equations: continuity, energy, x-momentum, y-momentum, z-momentum, turbulent dissipation rate (TDR), and turbulent kinetic energy (TKE)

Prism layers should be able to span enough of the boundary layer to capture the viscous sublayer as well as blend smoothly with the cells in the main flow field, as discussed in more detail in **section 4.2**. One way of assessing the performance of prism layers is to inspect the turbulent viscosity profile in the spanwise direction of the flow. **Figure 31** provides the turbulent viscosity heatmap across a section in the flow direction for the finest mesh case.

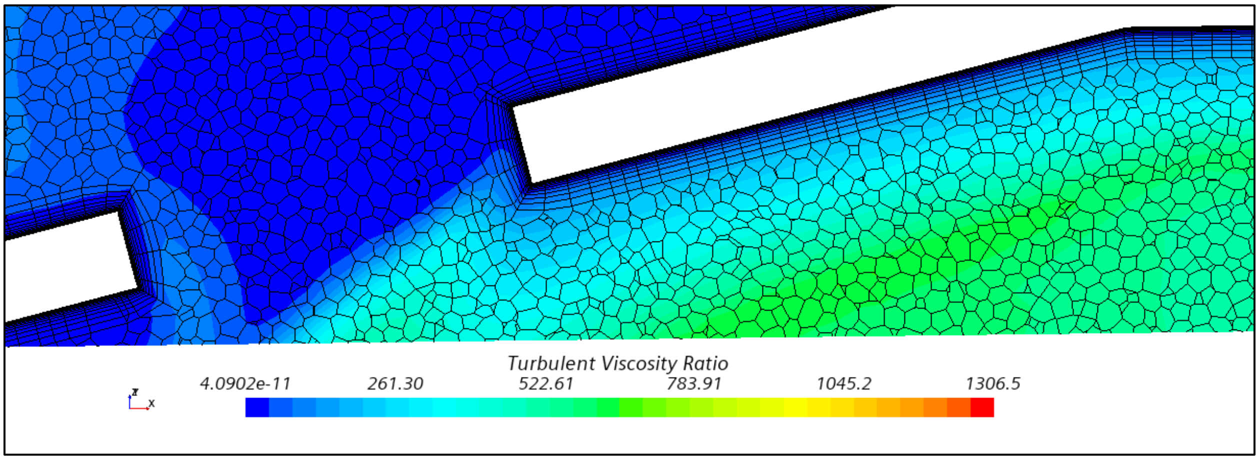

Figure 31: Turbulent viscosity ratio around a dilution hole to demonstrate the span of the used prism layers

Based on the elementary mesh independence study, we can conclude a satisfying mesh independence trend close to the mark of 2 mm in cell size. Different refinement levels can be employed at different locations in the CFD computational domain. This approach enables us to reduce the computational time while attaining further accuracy by reducing the cell size near the walls and complex geometries, while allowing for larger cell sizes at the core of the flow field. To achieve this, a customized mesh of sizes spanning between 3.0 mm and 0.3 mm is employed as shown in **Figure 32** and **Figure 33.** The same prism layer settings of the elementary mesh independence study are retained. The shown customized mesh, which will be referred to as the elected mesh, is a compromise on the accuracy versus computational costs, with a total cell count of 9.7 million cells. The error between the response attained by the finest elementary mesh and the elected mesh is calculated as 0.28%, 0.77%, 0.12% for the exit section average velocity, temperature, and total pressure, respectively. Hence, the elected mesh be will used from now to validate against experimental data and simulate new design cases as mesh independence in velocity, temperature, and total pressure is attained.

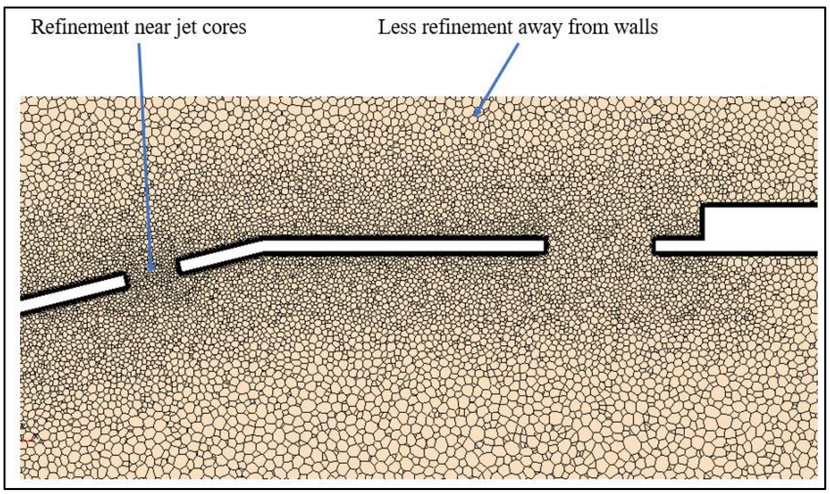

Figure 32: Mesh refinement around the test section for the elected mesh

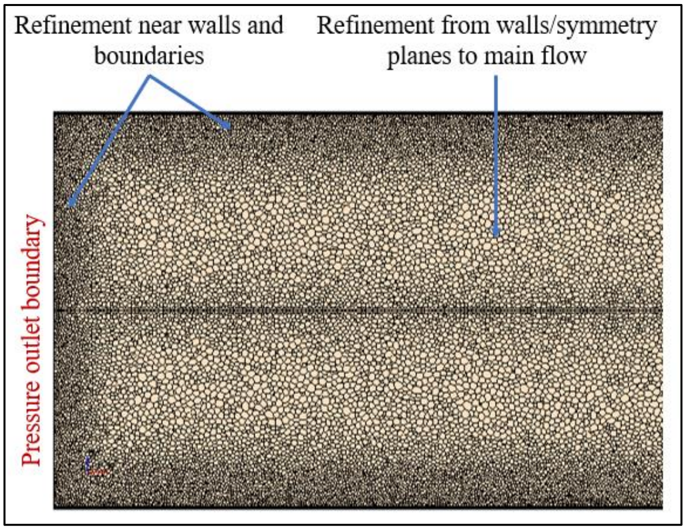

Figure 33: Mesh refinement around the outlet boundary for the elected mesh

5.2. Experimental Results, Numerical Model Validation and Factor Analysis

As outlined in **section 3.3** and **section 3.4**, the experiments are performed to maximize the heat transfer to the hot stream air with adequate insulation between the hot stream and cold stream until both streams meet at the test section. The experiments were conducted for the baseline case of unmodified geometry holes as well as jet extender geometry.

Following the mesh independence study, the elected mesh (with 9.7 million cells) is validated against experimental results, and used to carry out further numerical cases. **Figure 34** and **Figure 35** present the velocity profile response and temperature profile response versus experimental data for the unmodified geometry, respectively. The error in the mean velocity and mean temperature is 0.78% and 3.63% compared to experimental data, respectively. The average one-to-one error in the velocity profile is 5.78%, and the average one-to-one error in the temperature profile is 3.52%. The error in the average outlet section pressure is 7.6%.

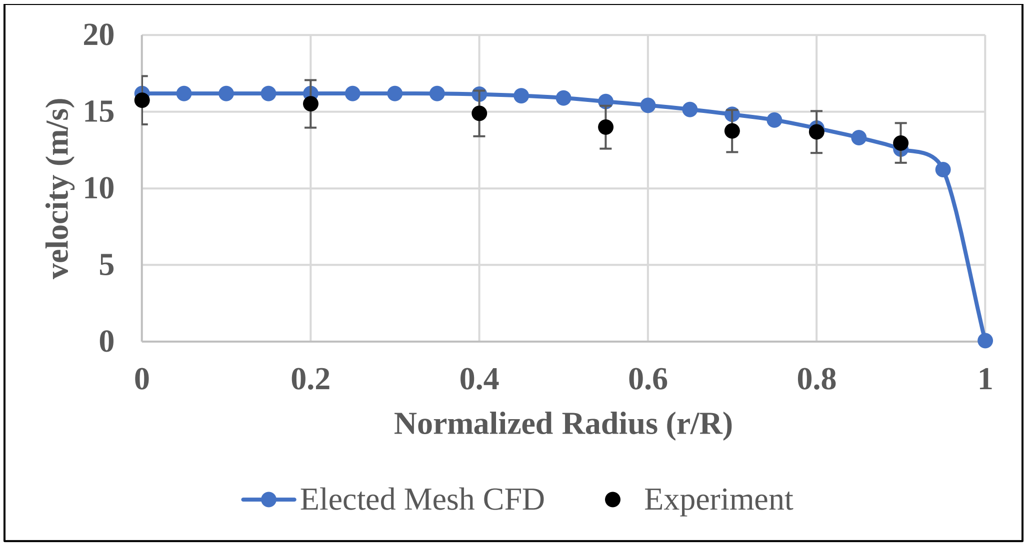

Figure 34: Unmodified geometry validation - Elected mesh velocity profile response versus experimental data

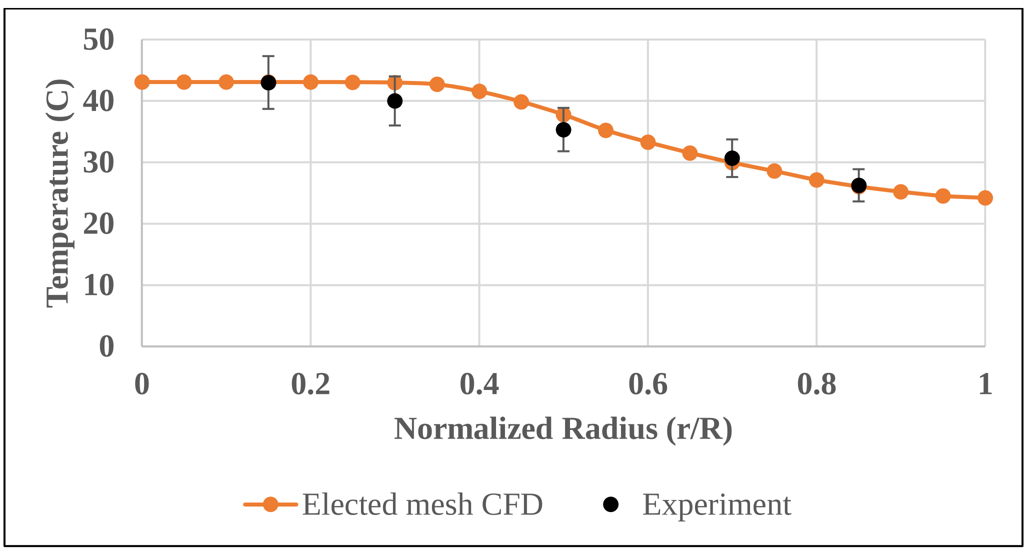

Figure 35: Unmodified geometry validation - Elected mesh temperature profile response versus experimental data

The same elected mesh is used to validate the models against experimental data for jet extender geometry. **Figure 36** and **Figure 37** present the velocity profile response and temperature profile response versus experimental data for the jet extender geometry, respectively. The error in the mean velocity and mean temperature is 0.24% and 3.21% compared to experimental data, respectively. The average one-to-one error in the velocity profile is 5.74%, and the average one-to-one error in the temperature profile is 2.11%. The error in the average outlet section pressure is 6.99%.

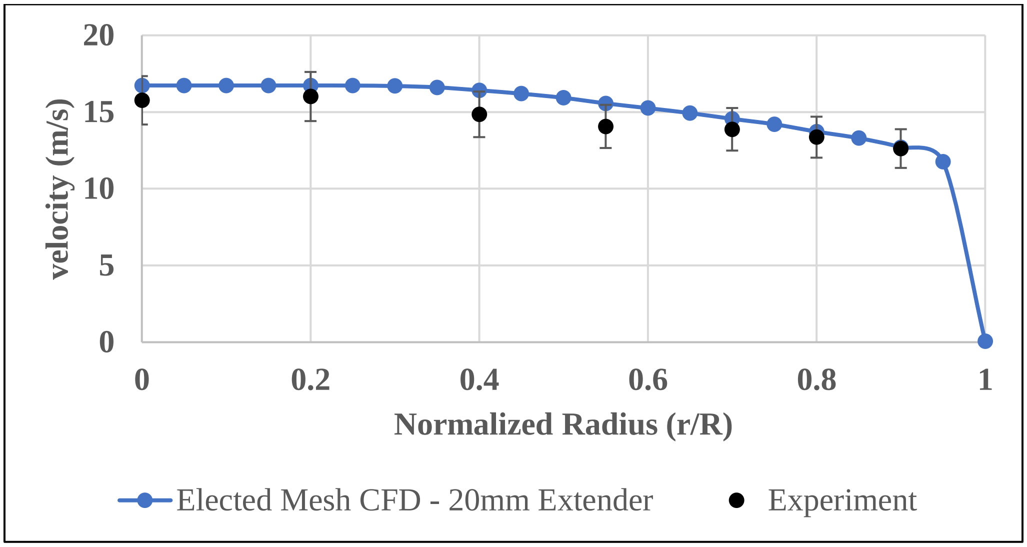

Figure 36: Extender (20 mm length) geometry validation - Elected mesh velocity profile response versus experimental data

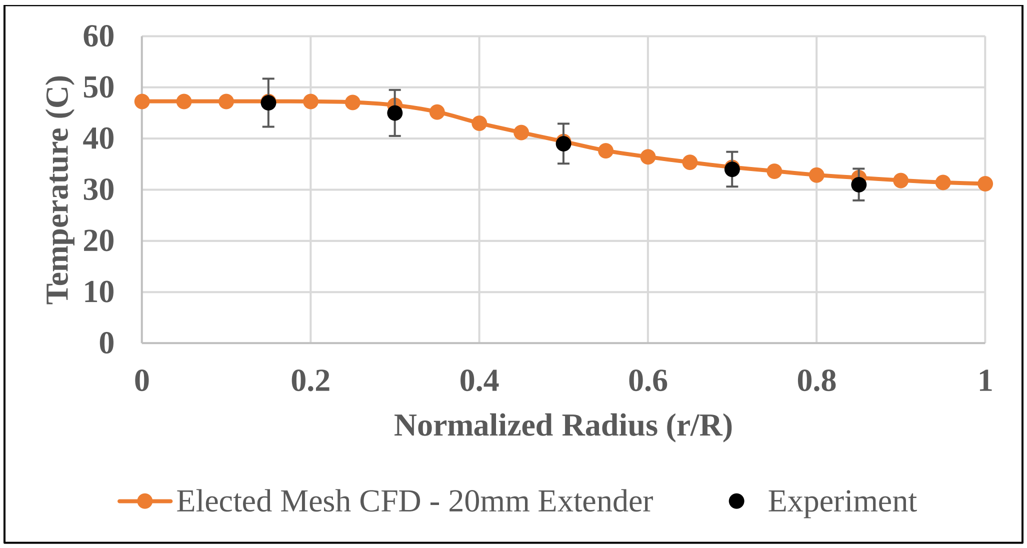

Figure 37: Extender (20 mm length) geometry validation - Elected mesh temperature profile response versus experimental data

The factor analysis study aims to uncover the strength of factors on the outlet section temperature uniformity and usefulness efficiency. This is a 2-level factor analysis, considering the temperature ratio (TR), Reynolds number, and jet extender length. The Reynolds number low and high numbers are 32,000 and 85,000, respectively. The temperature ratio low and high numbers are 1.5 and 2.5, respectively. The jet extender length low and high numbers are 5 mm and 25 mm, respectively. **Figure 38** presents a cube plot showing the 2-level factor analysis scenarios.

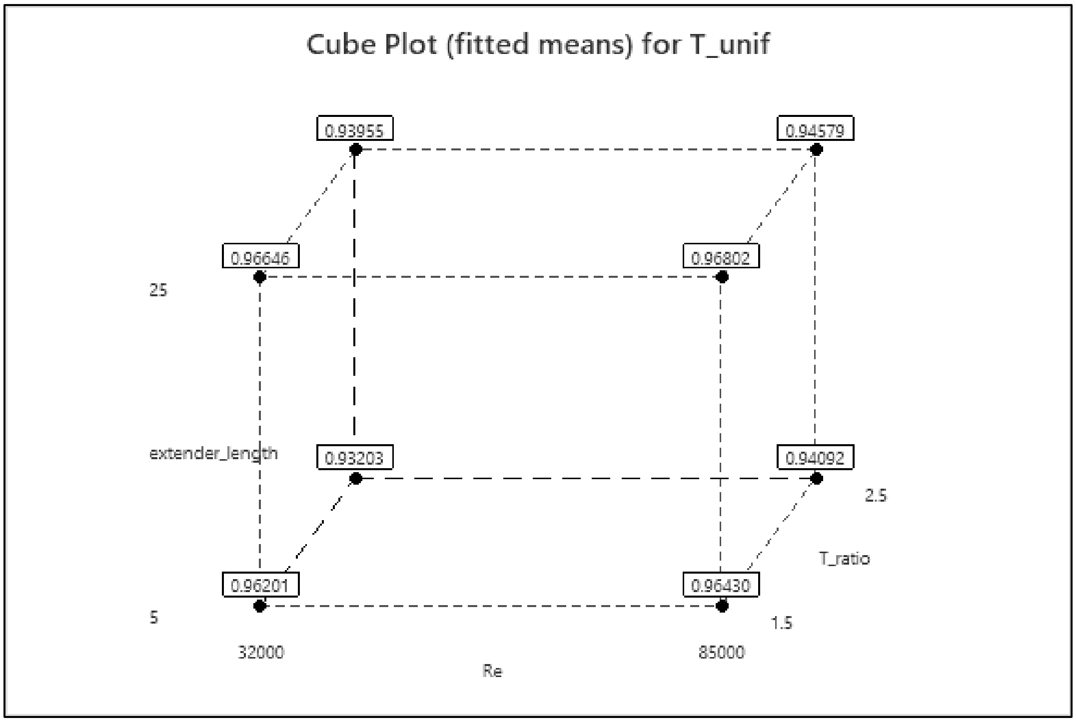

Figure 38: Factor analysis cube plot showing 2-level factorial scenarios

The factor analysis study uncovered the strength of effect of different factors as well as the confounding nature among these factors. **Figure 39** presents the effect pareto chart for the 2-level factor analysis. The jet extender length is the strongest factor affecting the usefulness efficiency, followed by the temperature ratio and then the inlet sections Reynolds number. Some confounding effect can be observed with lower effect compared to primary effects of each variable. These observations are underscored by **Figure 40**, which shows the main effect of variables, and **Figure 41**, which shows the confounding effect among variables.

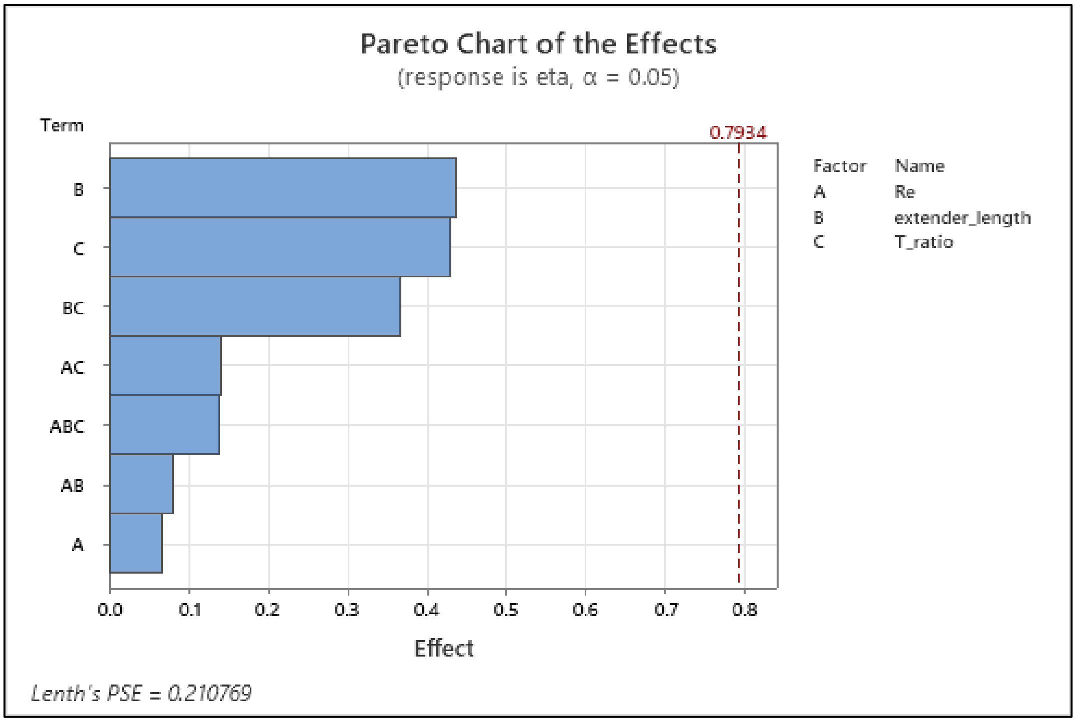

Figure 39: Pareto chart for the effect of factors in the 2-level factor analysis study

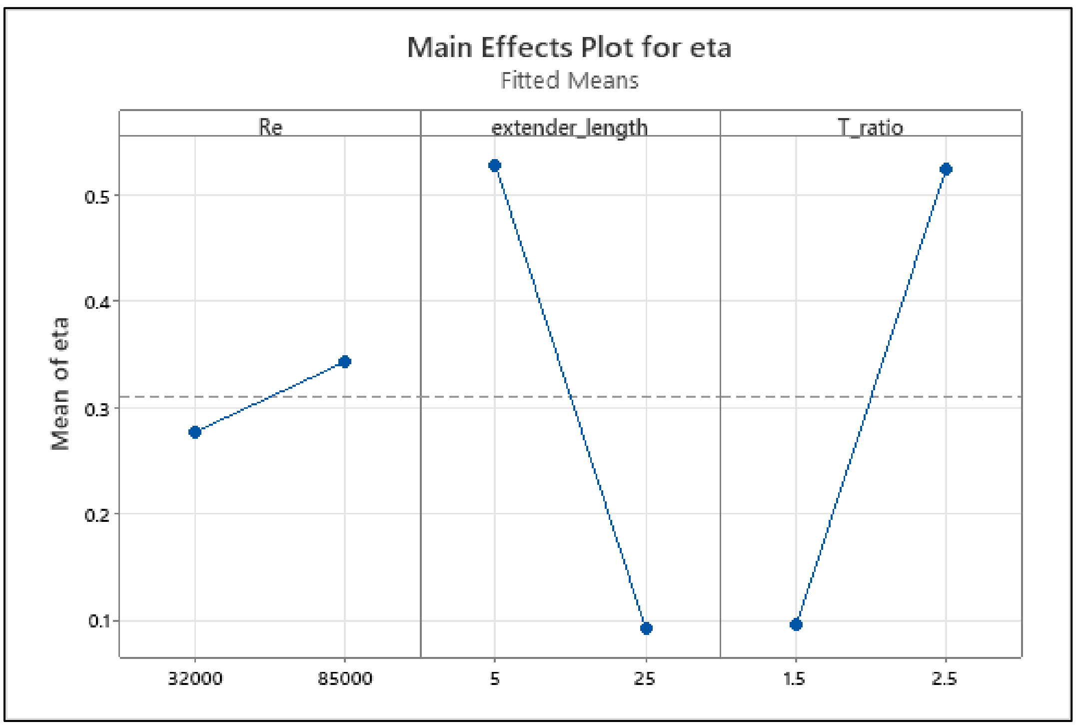

Figure 40: Main effect plot, showing the strength of factor on the response as part of the 2-level factor analysis study

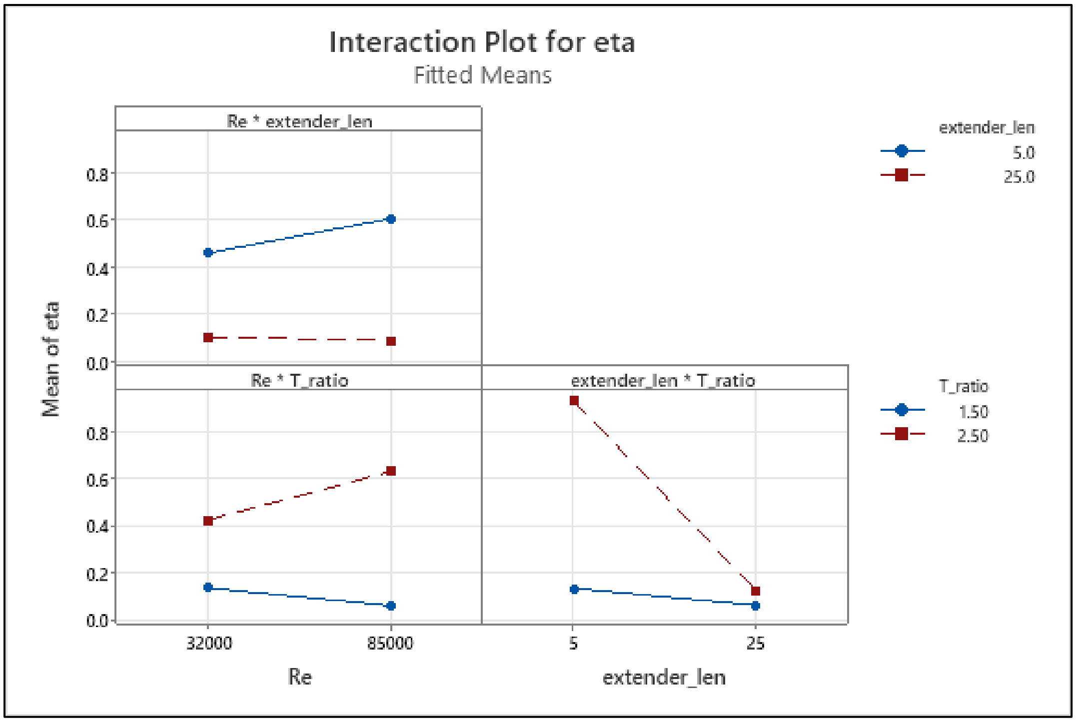

Figure 41: Interaction plot of the 2-level factor analysis, showing the confounding effect of variables on the usefulness efficiency response

Based on the factor analysis study, we can observe that the temperature uniformity and extender length are the strongest factors affecting the usefulness efficiency. It is also observed that the Reynolds number holds less significance on the usefulness efficiency, compared to the other factors. Therefore, we will consider the temperature uniformity and extender length as the two main factors in the upcoming sensitivity studies.

A sensitivity study is performed on the baseline geometry, and outlines the temperature uniformity index response versus Reynolds number and temperature ratio. The results of this sensitivity study for the baseline geometry are outlined by **Table 4**. **Figure 42** presents the temperature uniformity index for the baseline geometry sensitivity study cases. For each temperature ratio, the relation between the temperature uniformity index and the Reynolds number appears to be nearly linear. **Figure 43** shows the pressure drop for the baseline cases sensitivity study, which appears to be nearly parabolic for all temperature ratios.

Table 4: Baseline sensitivity study results

Reynolds Number	Temperature Ratio	Cold Inlet Temperature (C)	Hot Inlet Temperature (C)	Temperature Uniformity Index	Pressure Drop (Pa)
32,000	1.5	26.5	176.3	0.962	21
42,000	1.5	26.5	176.3	0.962	37
54,000	1.5	26.5	176.3	0.963	58
64,000	1.5	26.5	176.3	0.963	83
75,000	1.5	26.5	176.3	0.964	113
85,000	1.5	26.5	176.3	0.964	147
32,000	2	26.5	326.2	0.941	28
42,000	2	26.5	326.2	0.943	49
54,000	2	26.5	326.2	0.944	77
64,000	2	26.5	326.2	0.945	111
75,000	2	26.5	326.2	0.946	151
85,000	2	26.5	326.2	0.947	196
32,000	2.5	26.5	476.0	0.931	31
42,000	2.5	26.5	476.0	0.933	54
54,000	2.5	26.5	476.0	0.935	85
64,000	2.5	26.5	476.0	0.936	122
75,000	2.5	26.5	476.0	0.938	166
85,000	2.5	26.5	476.0	0.939	217

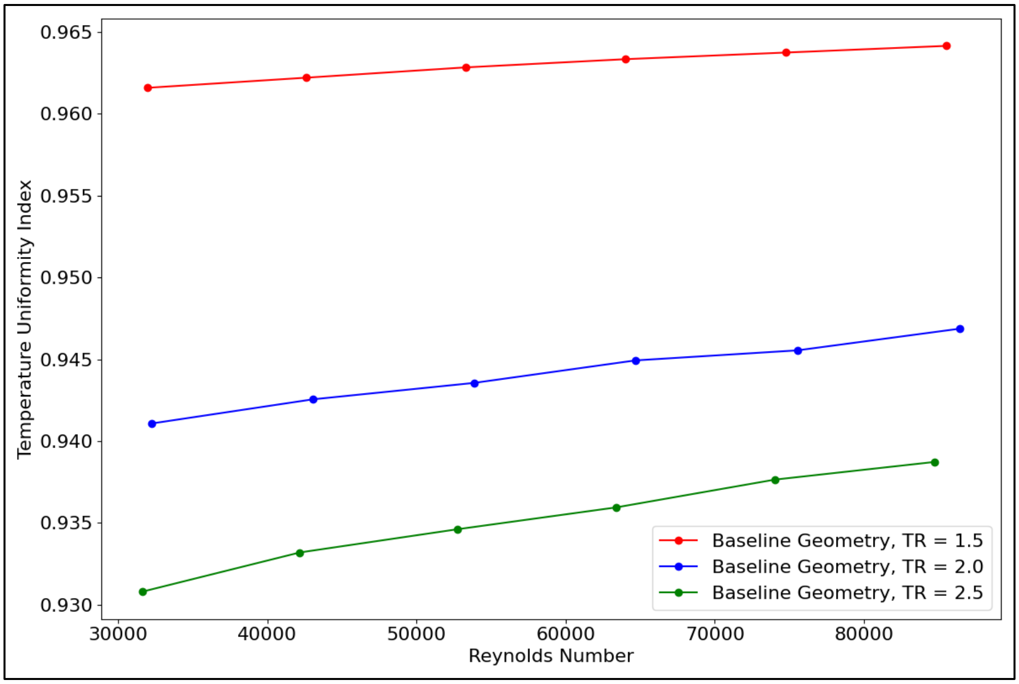

Figure 42: Baseline geometry sensitivity study of the temperature uniformity index versus Reynolds number, with contour lines for the temperature ratio

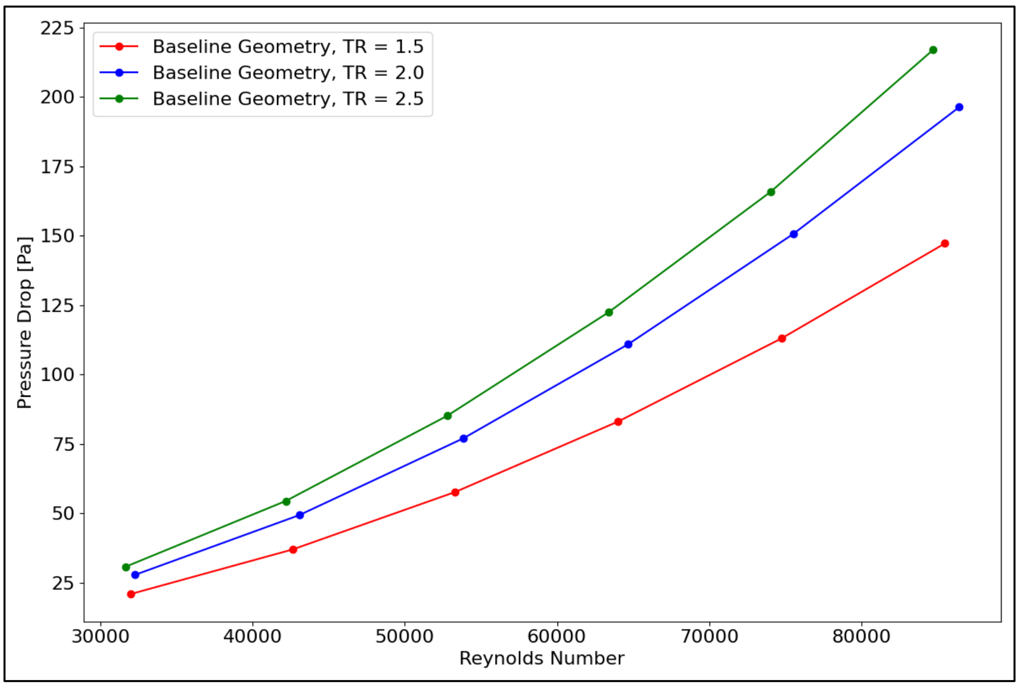

Figure 43: Baseline geometry sensitivity study of the pressure drop versus Reynolds number, with contour lines for the temperature ratio

5.3. Parametric Study on Using Dilution Jet Extenders

This section outlines the performance of jet extenders in terms of temperature uniformity and pressure loss as outlined by the usefulness efficiency. First, **Figure 44** and **Figure 45** show the surface mesh and the volume cell mesh, respectively, of a sample jet extender case of 50 mm diameter, and 20 mm cylinder length.

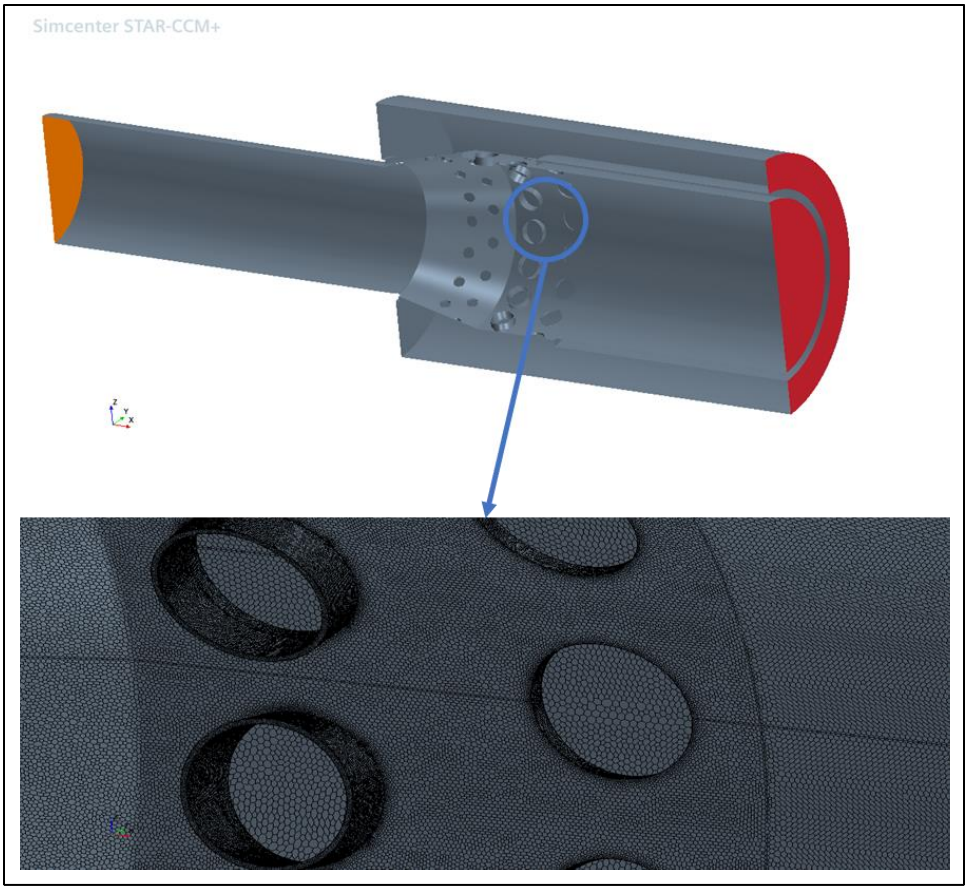

Figure 44: Surface mesh using the elected mesh settings for the jet extender baseline geometry

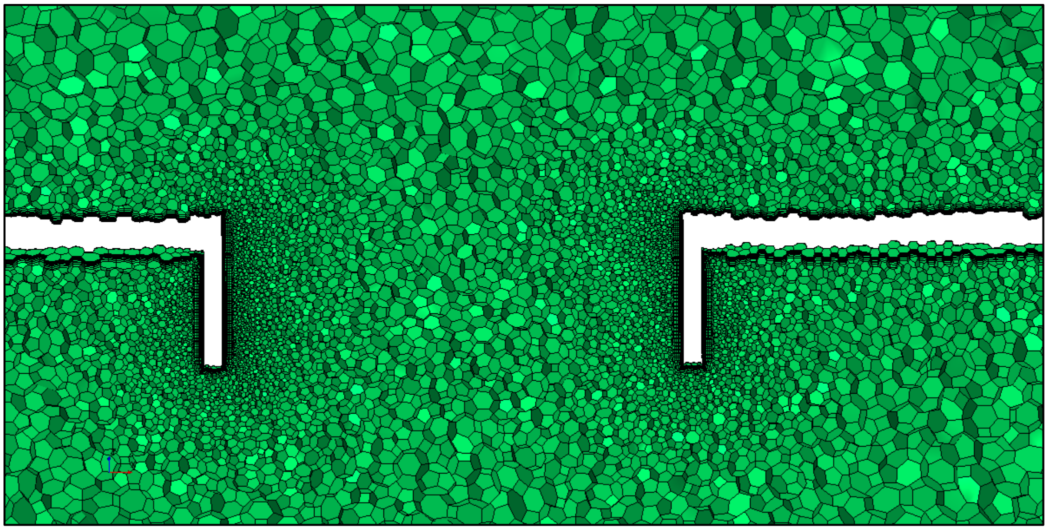

Figure 45: Volume cell mesh showing the level of detail around and within the dilution jet extender area as well as the non-collapsing prism layers around the wall surfaces

A sensitivity study investigates the effect of temperature ratio and extender length of several variables including the usefulness efficiency, pressure drop, temperature uniformity index, normal velocity, and jet mass flow rate. The case study focuses on the outlined temperature ratios of 1.5, 2.0, and 2.5. Also, the investigated extender lengths include 5mm, 10mm, 15mm, 20mm, and 25mm. All of these cases are performed at a constant Reynolds number of 54,000. **Table 5** provides a summary of the jet extender sensitivity study results. **Figure 46** presents the temperature uniformity index versus extender length at varying temperature ratios. **Figure 47** presents the pressure drop versus extender length at varying temperature ratios. **Figure 48** presents the usefulness efficiency versus extender length at varying temperature ratios. The usefulness efficiency has an inverse power-law relation with the extender length. The usefulness efficiency changes slightly at low temperature ratios and extender lengths. The appendix section presents sensitivity study results for the jet mass flow rate, usefulness efficiency curves, and change percentage in temperature and pressure.

Table 5: Sensitivity study for the jet extender cases, benchmarked to the baseline geometry cases. Study parameters: Reynolds number = 54,000, cold inlet temperature = 26.5 ºC (299.65 K)

Extender Length (mm)	Temperature Ratio	Temperature Uniformity Index	Pressure Drop (Pa)	Temperature Uniformity Improvement %	Pressure Drop Inc.%	Usefulness Efficiency
5	1.5	0.963	60.6	0.93	5.09	3.60
10	1.5	0.964	64.3	2.74	11.63	2.02
15	1.5	0.965	68.2	6.68	18.28	2.00
20	1.5	0.966	71.2	9.54	23.50	1.73
25	1.5	0.967	73.7	10.80	27.84	1.39
5	2	0.944	80.8	0.88	4.96	3.56
10	2	0.946	85.6	4.12	11.20	3.29
15	2	0.947	90.2	6.58	17.16	2.23
20	2	0.950	94.1	11.33	22.26	2.29
25	2	0.951	97.1	13.02	26.15	1.91
5	2.5	0.936	89.0	2.26	4.63	10.51
10	2.5	0.938	94.2	5.93	10.80	5.08
15	2.5	0.940	99.3	8.15	16.71	2.92
20	2.5	0.943	103.1	12.26	21.15	2.74
25	2.5	0.944	106.3	14.90	25.02	2.38

y(x, TR=1.5) = 0.0002x + 0.9622, R2=0.9744. y(x, TR=2.0) = 0.0004x + 0.9423, R2 = 0.9845. y(x, TR=2.5) = 0.0004x + 0.9341, R2 = 0.9936

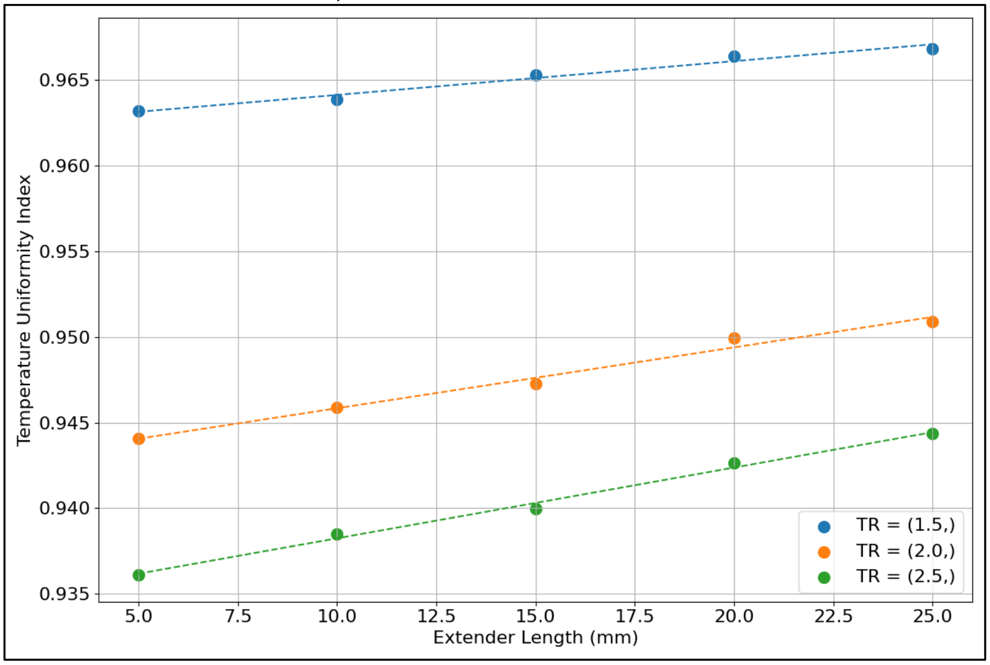

Figure 46: Temperature uniformity index versus extender length at varying temperature ratios (Re = 54,000).

y(x, TR=1.5) = 0.6613x + 57.678, R2=0.992. y(x, TR=2.0) = 0.8229x + 77.2420, R2 = 0.992. y(x, TR=2.5) = 0.8697x + 85.3400, R2 = 0.99

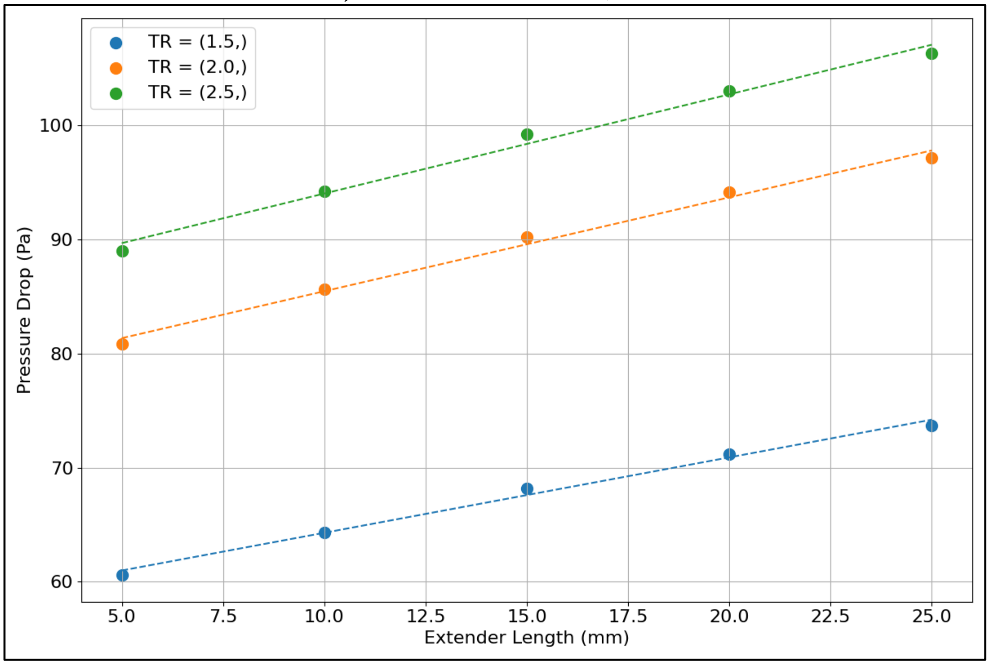

Figure 47: Pressure drop versus extender length at varying temperature ratios (Re = 54,000).

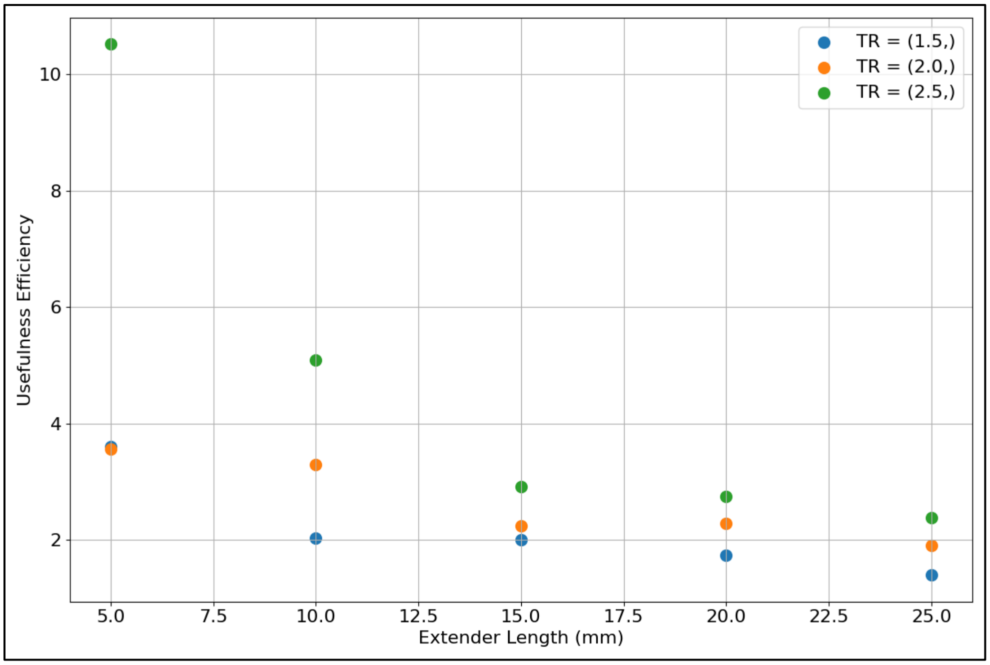

Figure 48: Usefulness Efficiency versus extender length at varying temperature ratios (Re = 54,000).

Jet extenders provide protection for the dilution jets and enable the jet core to develop and get ejected into the main flow at a further distance, depending on the extender length. To quantify this effect, we can observe the variation in the axial velocity within the main flow. **Figure 49** illustrates the coordinate system and direction of the axial velocity within the main flow. **Figure 49** is a front view of the dilution can, where dilution jet extenders are highlighted in pink. The same figure also demonstrates the z-axis of the jet core coordinate system, pointing toward the main flow. An increased axial velocity (in the z-direction) indicates higher penetration of dilution jets into the main flow.

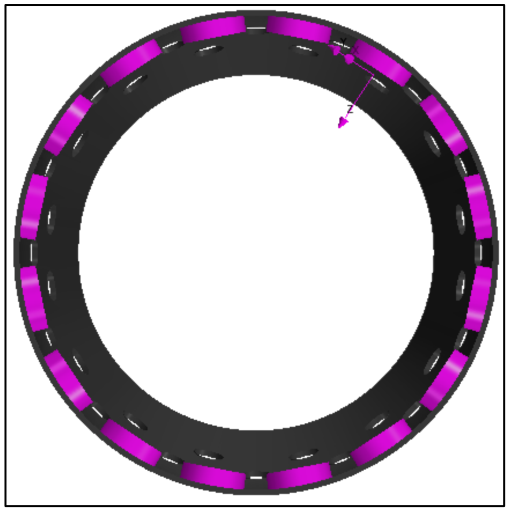

Figure 49: Front view of the dilution can, showing the z-axis aligned with the jet axial velocity that penetrates the main flow

Figure 50 shows the jet average axial velocity versus extender length, at different temperature ratios values. The average jet axial velocity appears to change linearly with the jet extender length. The change in jet axial velocity is also linear with the temperature ratio, at the same jet extender length. Higher axial jet velocities allow the jet to penetrate deeper into the main flow. Thereby, enable higher mixing and a better temperature uniformity index.

y(x, TR=1.5) = 0.0292x + 1.3991, R2=0.999. y(x, TR=2.0) = 0.0308x + 1.8489, R2 = 0.995. y(x, TR=2.5) = 0.0343x + 2.0403, R2 = 0.995

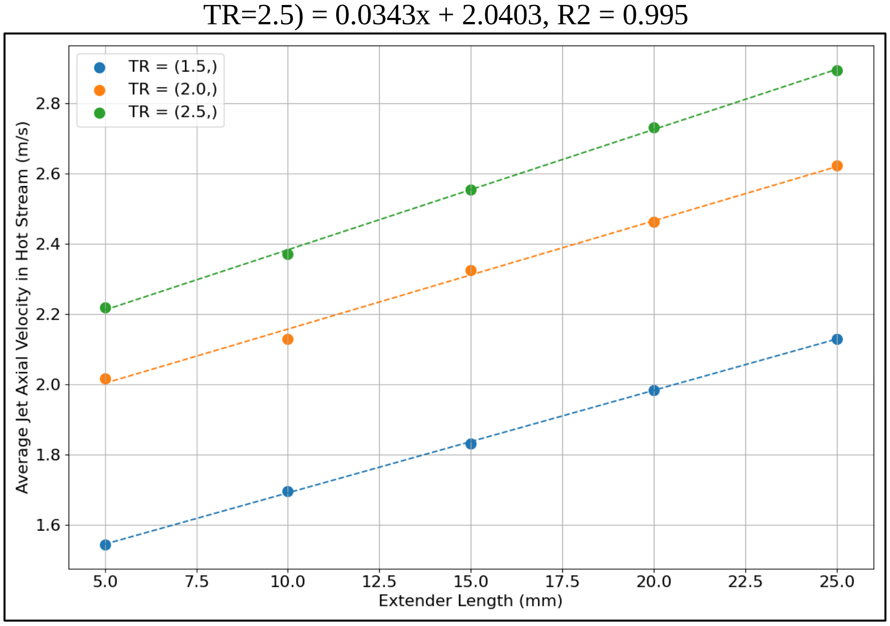

Figure 50: Jet axial velocity (m/s) versus extender length (mm) at different temperature ratio values (Re = 54,000).

The increase in jet axial velocity penetration into the main flow can be visualized by **Figure 51**, which shows the velocity heat map of the test section side-view. High jet penetration is observed with longer jet extenders. Also, this effect translates into an increase in the velocity of the outlet section, as jet extenders enable the dilution jet core to develop further and ameliorate the effect of cross flow by the hot stream. The increased penetration of dilution jets into the main flow allows the temperature to blend further and promote a high temperature uniformity. **Figure 52** shows the effect of dilution jet penetration on the outlet surface temperature. High lengths of jet extenders flatten the hot temperature core at the outlet section, compared to the baseline case without jet extenders.

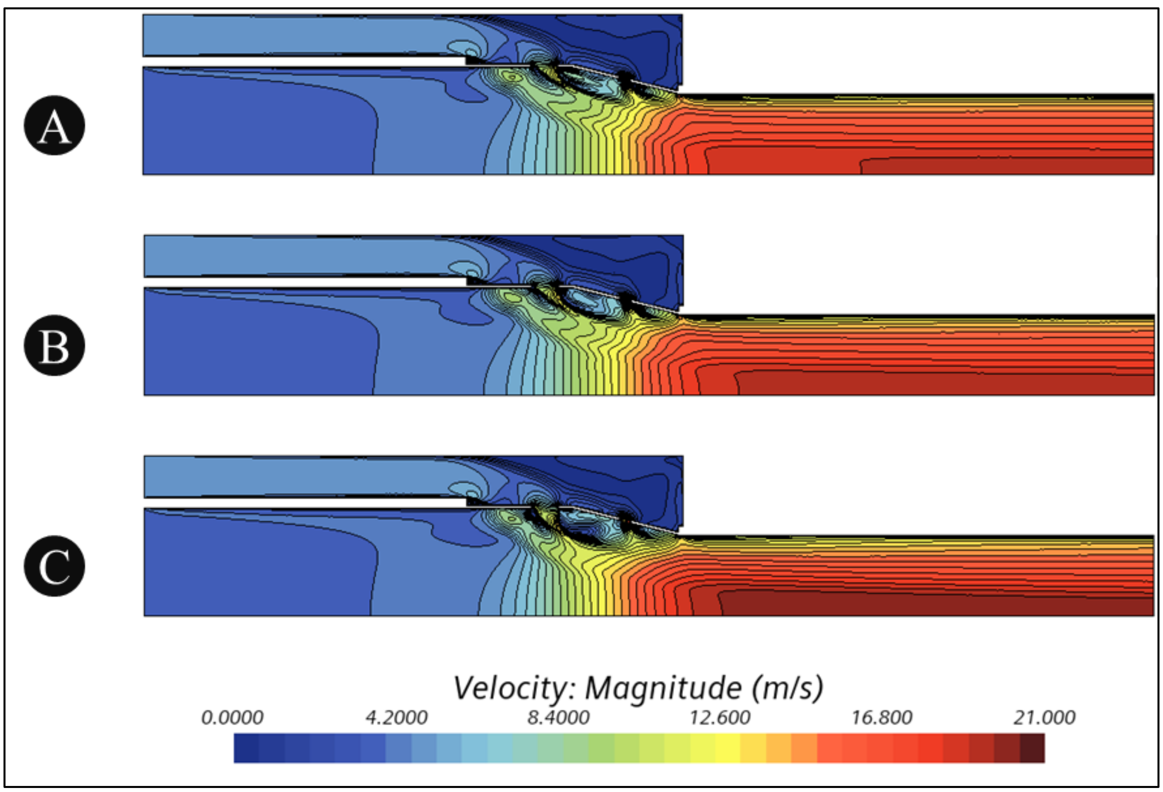

Figure 51: Side-view of the test section, showing velocity heat map at TR = 1.5. (A) baseline case at Re = 54,000, (B) 5mm jet extender at Re = 54,000, (C) 20 mm jet extender at Re = 54,000

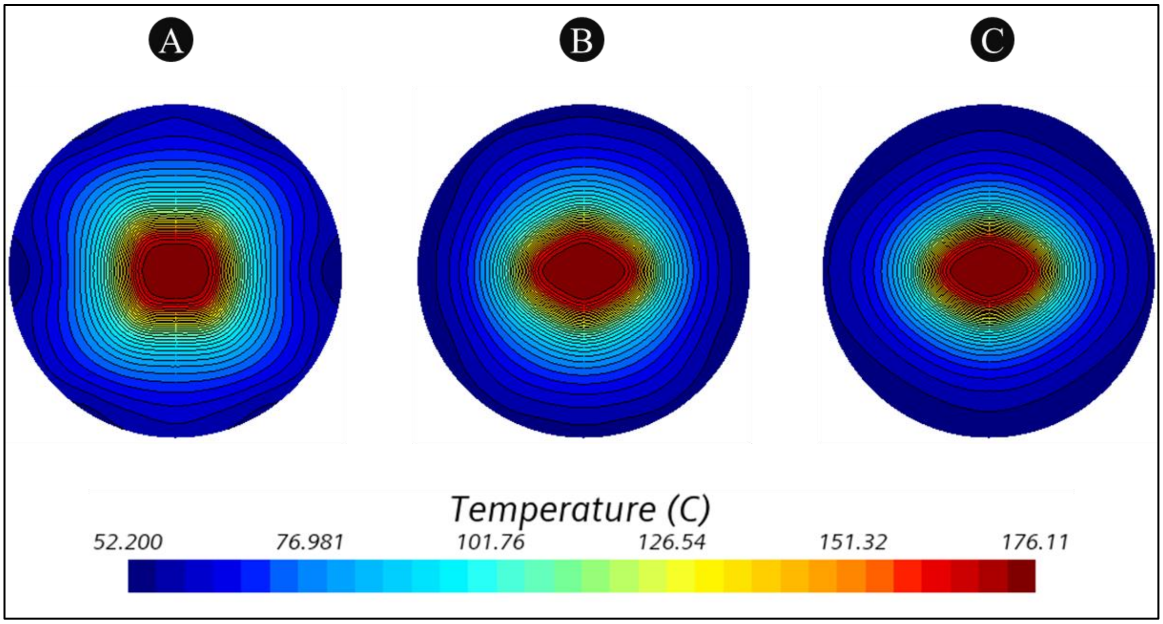

Figure 52: Front-view of the outlet surface, showing temperature heat map at TR = 1.5. (A) baseline case at Re = 54,000, (B) 5mm jet extender at Re = 54,000, (C) 20 mm jet extender at Re = 54,000

Figure 53 presents a sliced view of the dilution jet core, from the cold air inlet (top circular section) to 6 cm below the dilution jet hole. As evident by **Figure 53**, the k-component of velocity is reduced in the case of jet extender cases, which means that the dilution jet maintains its perpendicular velocity toward the main flow. Also, this figure is evidence of the reduced effect of crossflow on the dilution jets that are protected by the jet extender surface.

The normalized mixture fraction (f^*) is used to gauge the temperature uniformity across the radius of the outlet pipe. **Figure 54** presents the normalized mixture fraction versus the normalized radius (r/R) for different jet extenders lengths, temperature ratio of 1.5, and Reynolds number of 54,000. We can observe the contraction of the normalized mixture fraction with jet extenders, which indicates better temperature uniformity and a closer temperature profile to the equilibrium temperature, compared to the baseline case. The appendix contains similar figures for the normalized mixture fraction at temperature ratios of 2.0 and 2.5.

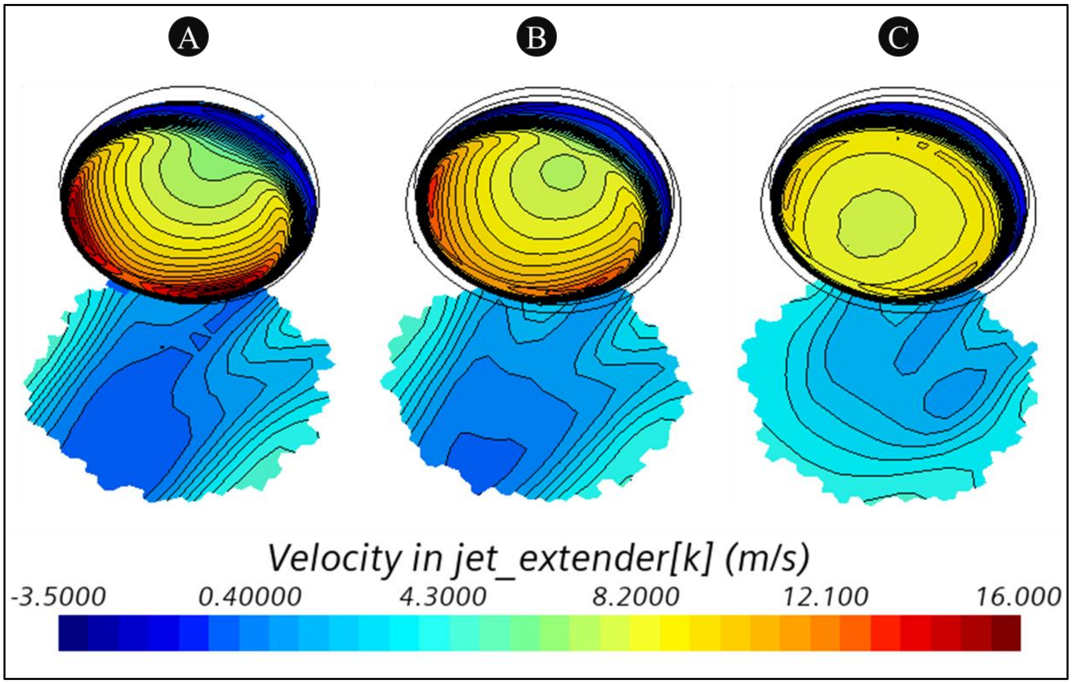

Figure 53: Sliced view of dilution jet core, showing k-component velocity (+ve in direction of primary flow) at TR = 1.5. (A) baseline case at Re = 54,000, (B) 5mm jet extender at Re = 54,000, (C) 20 mm jet extender at Re = 54,000

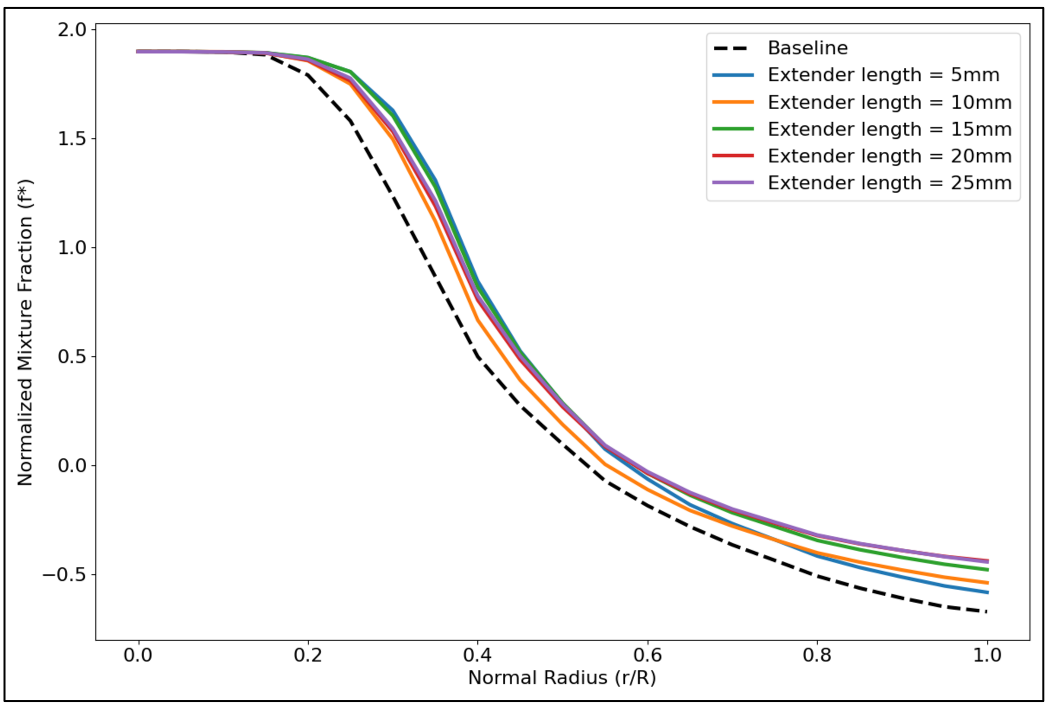

Figure 54: Normalized Mixture Fraction (f*) versus normal radius (r) for the baseline case and varying jet extender lengths (TR = 1.5, Re = 54,000)

From the previous figures, it can be seen that the jet extenders provide several functionalities. First, it protects the converging section small dilution hole jets from dissipating and being swept away by the main flow field that precedes it. Hence, allowing for a better cooling reach on the circumference of the outlet pipe. Second, the dilution holes that are equipped with the jet extender are being protected from the previous flow, and allows the jet to develop further and reach deeper into the main flow field. Therefore, enabling higher penetration of the jet stream and reducing the amount of wasted kinetic energy as a result of multiple jet rows sweeping forward pushing the consequent jets into the walls and away from the main flow field. Ultimately, the extended jet modifiers are shown to enhance the temperature uniformity of the downstream mixed gases, and reduce energy dissipating within the dilution test section. **Figure 55** shows the enhanced temperature uniformity in the perspective of normalized mixture fraction heat map for the baseline and jet extender cases.

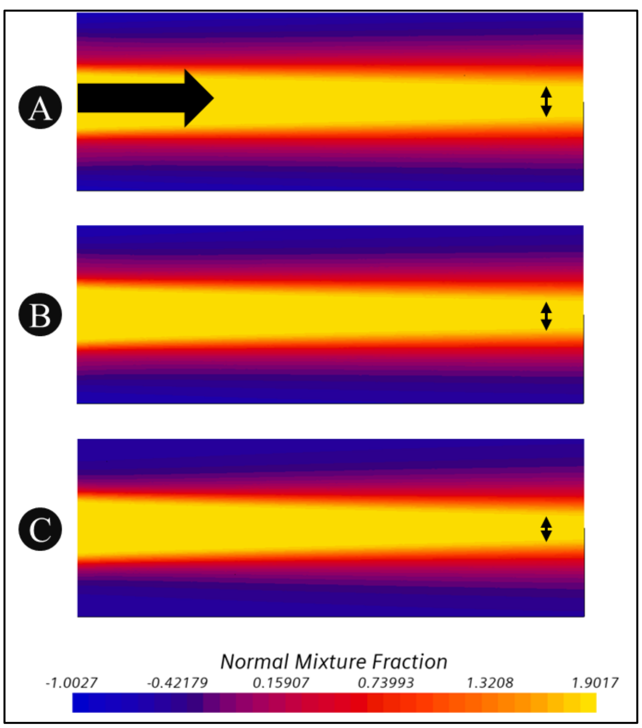

Figure 55: Sideview planar cross section of the outlet pipe, showing the normalized mixture fraction at TR = 1.5. Black arrow in direction of axial flow (A) baseline case at Re = 54,000, (B) 5mm jet extender at Re = 54,000, (C) 20 mm jet extender at Re = 54,000

5.4. Parametric Study on Using Dilution Jet Area Modifiers

The jet area modifiers are geometry parts installed on the second array of large dilution holes. Each of these parts resembles a converging nozzle, where the exit area is smaller than the inlet area. The area ratio (A_2/A_1) is defined to control the dimensions of the jet area modifier parts. Where, A_2 is the part inlet area, and A_1 is the part exit area. **Figure 56** illustrates the jet area modifiers at different lengths and area ratios.

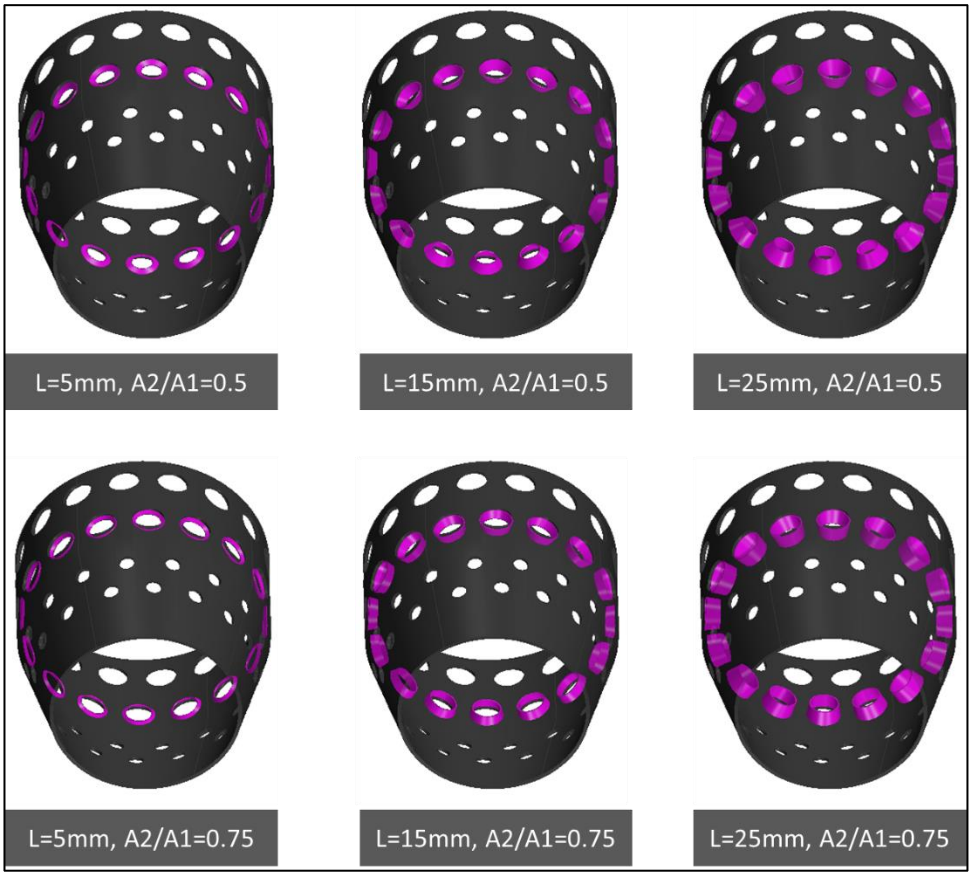

Figure 56: Jet area modifiers installed on the dilution can

The aim of these parts is to twofold. First, protect the dilution jet from the crossflow of the primary stream and the spent air from the subsequent array of dilution holes. This allows the dilution jet to flow a little further without being impeded by crossflow. Second, the area modifier part accelerates the dilution jet flow, aiming to lead to higher penetration into the main flow and thereby, better mixing. A sensitivity study explores the performance of area modifier parts at different lengths (5mm, 15mm, and 25mm), and area ratios (0.5 and 0.75). **Table 6** summarizes the sensitivity study results for the jet area modifier parts.

Table 6: Sensitivity study for the jet area modifier cases, benchmarked to the baseline geometry cases. Study parameters: Reynolds number = 54,000, temperature ratio = 1.5, cold inlet temperature = 26.5 °C (299.65 K)

Extender Length (mm)	Area Ratio (A2/A1)	Temperature Uniformity Index	Pressure Drop (Pa)	Temperature Uniformity Improvement %	Pressure Drop Inc.%	Usefulness Efficiency
5	0.5	0.974	82.58	29.43	43.25	1.57
5	0.75	0.967	70.67	10.89	22.61	2.13
15	0.5	0.974	86.03	29.78	49.25	1.23
15	0.75	0.967	73.63	10.23	27.74	1.33
25	0.5	0.974	87.96	29.52	52.60	1.07
25	0.75	0.968	79.38	12.80	37.72	0.90

Results indicate that the length of the jet area modifier does not affect the temperature uniformity index. However, the added pressure drop has a nearly linear relation with the length of the jet area modifier. The half area (A2/A1=0.5) jet modifier results in slightly higher temperature uniformity factor, but with an average increase of 12.9% in pressure drop, compared to the three-quarters area (A2/A1=0.75) jet modifiers. In all cases, the jet area modifier resulted in a higher temperature uniformity compared to the standard jet extender cases. However, jet area modifiers yield a more substantial pressure drop compared to the standard jet extender cases. **Figure 57** presents the velocity on a cross section of the outlet pipe. The prescribed figure illustrates the increase of velocity magnitude in the cases of jet extenders. This is ascribed to the reduced energy dissipation due to cross flow. Also, jet area modifier result in a slightly increased velocity compared to the standard extender, especially around the area of dilution jet holes. **Figure 58** outlines the effect of jet area modifiers in terms of outlet pipe temperature, versus standard extenders and the baseline geometry.

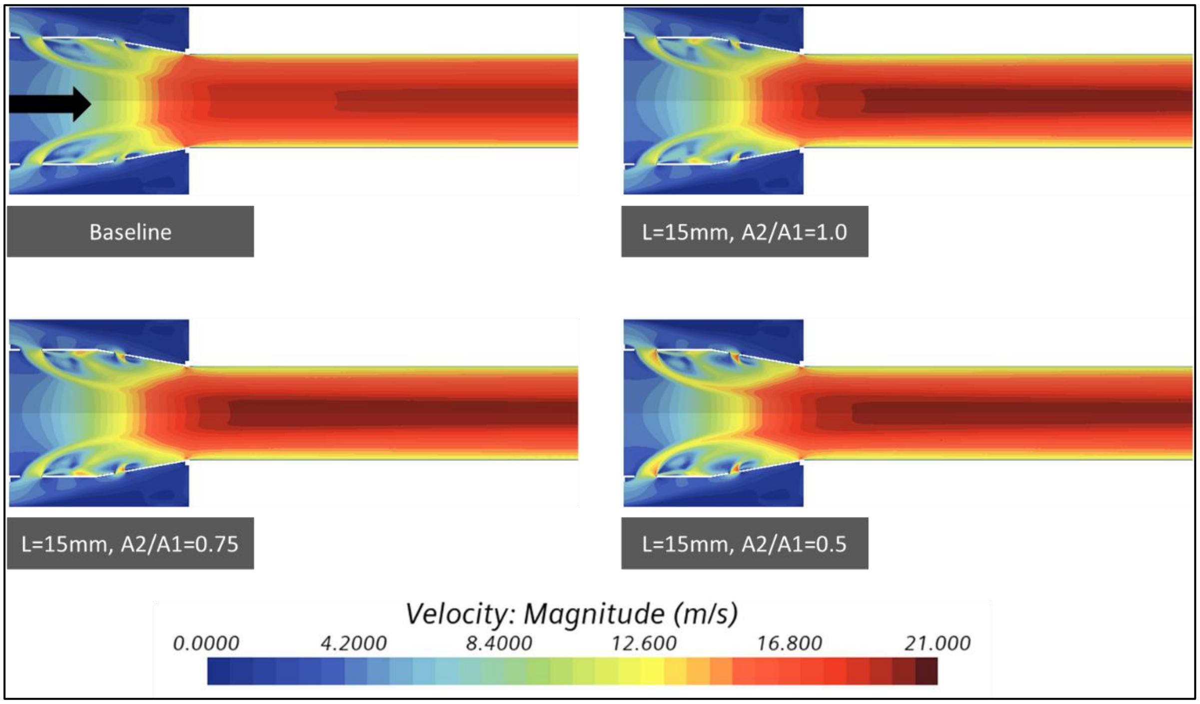

Figure 57: Sideview planar cross section, showing the velocity magnitude at TR = 1.5 and Re = 54,000 for baseline, 15mm extender, 15mm jet area modifier with 0.75 area ratio, and 15mm jet area modifier with 0.50 area ratio. Black arrow in direction of axial flow

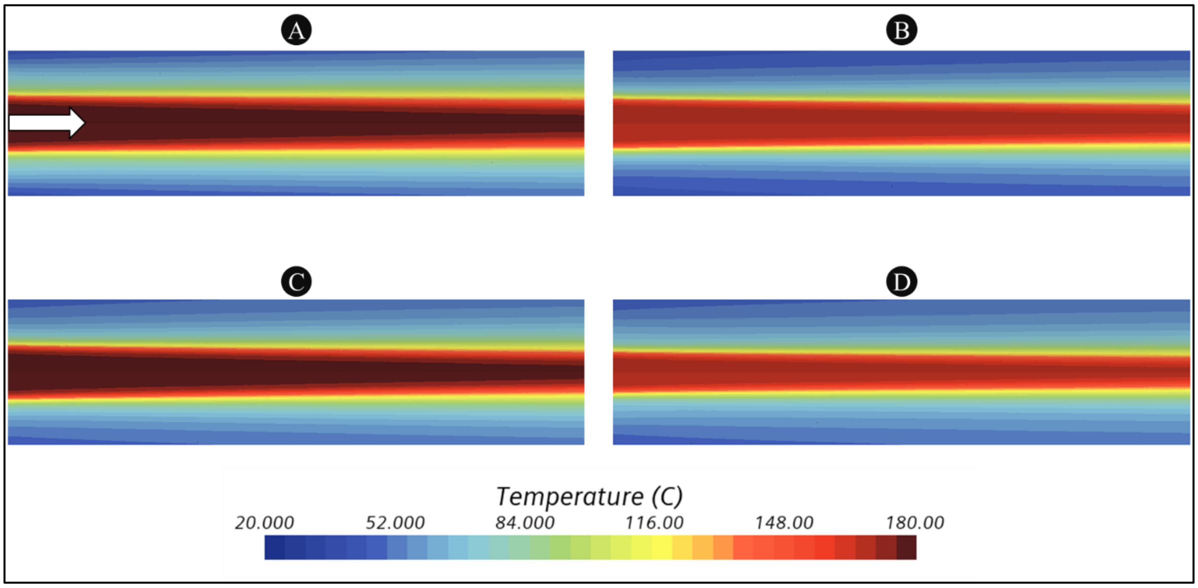

Figure 58: Sideview planar cross section of the outlet pipe, showing the temperature at TR = 1.5 and Re = 54,000. White arrow in direction of axial flow (A) baseline case, (B) 15mm jet extender with A2/A1 = 1.0, (C) 15mm jet extender with A2/A1 = 0.75, and (D) 15mm jet extender with A2/A1 = 0.5

The previous figures illustrate the superior performance of jet area modifiers in terms of temperature uniformity and the outlet mean temperature, especially jet area modifiers with small area ratios. **Figure 59** illustrates the normalized mixture fraction for the baseline and extender cases with different area ratios. All jet extender cases showcase a more compact normal mixture fraction curve (upper and lower ends are closer to 1). This is evidence of a higher temperature uniformity. Also, the jet area modifier with area ratio equal to 0.5 results in the profile closest to 1.0, which is indicative of temperatures close to the equilibrium temperature.

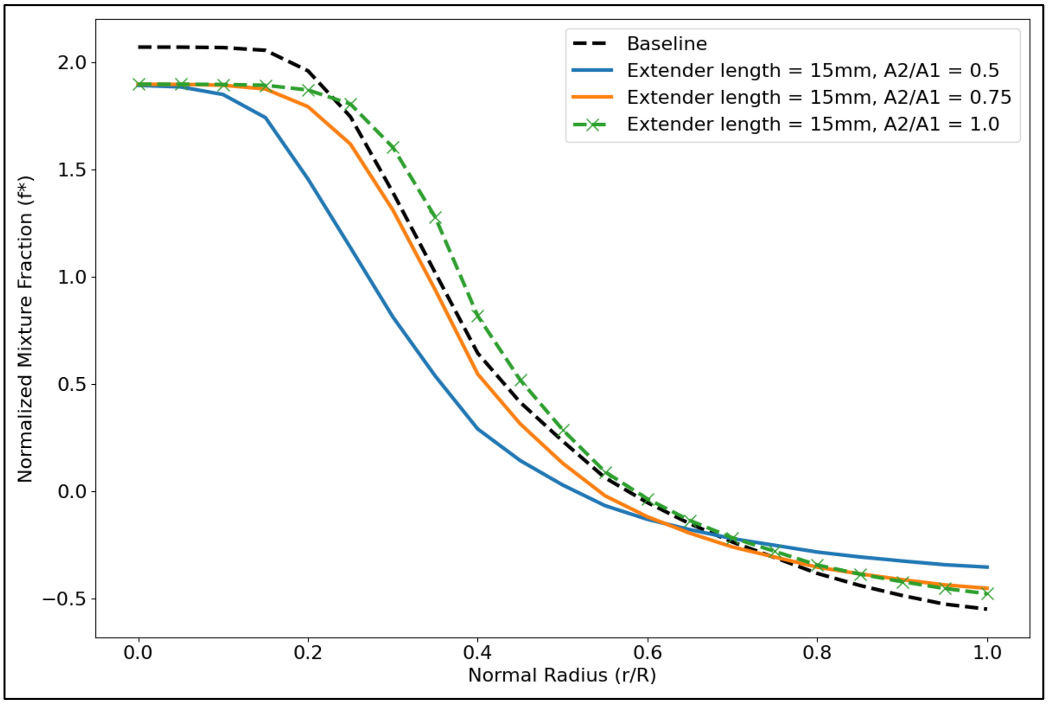

Figure 59: Normalized Mixture Fraction (f*) versus normal radius (r) for the baseline case and 15 mm jet extender length and area ratios of 0.50, 0.75, and 1.0 (TR = 1.5, Re = 54,000)

5.5. Turbulence Models Case Study

The realizable $k - \varepsilon$ model is known for its robustness and capability in modeling turbulent flows with moderate to high adverse pressure gradients. To gain more confidence in the model, we validated the model against experimental data. The realizable $k - \varepsilon$ model performed very well and produced results within the experiment error ranges. To gain more confidence in the model, and understand how other models would perform, we will present a case study that models the same experimental conditions. This turbulence model case study explores the performance of the $k - \omega\ (SST)$ and Reynolds Stress Transport (RST) turbulence models. We will utilize the same elected mesh, outlined in **section 5.1** and **section 5.2**. Also, all models are tested under the same boundary conditions, segregated fluid and energy solvers, and steady state approach. The RST model assumes anisotropy in turbulence quantities and models pressure-strain interactions. The RST model is favorable in modeling highly turbulent flows and recirculating flows. However, the RST model is complex, computationally expensive, and requires great attention to boundary and initial conditions to facilitate convergence. The $k - \omega\ (SST)$ turbulence model offers strong modeling capabilities in boundary layers and with flow separation. It offers a balance between the standard $k - \varepsilon$ and standard $k - \omega$ models. Nonetheless, the $k - \omega\ (SST)$ model struggles with strong adverse pressure gradients. It has a stronger tendency to diverge, compared to the realizable $k - \varepsilon$ mode, if the initial conditions, boundary conditions, and solver are not fine-tuned and set up properly.

Figure 60 presents the outlet section velocity profile comparison of all tested models against experimental data for the baseline case presented in **section 5.2. Figure 61** presents the outlet section temperature profile for all models against experimental data, under the same conditions.

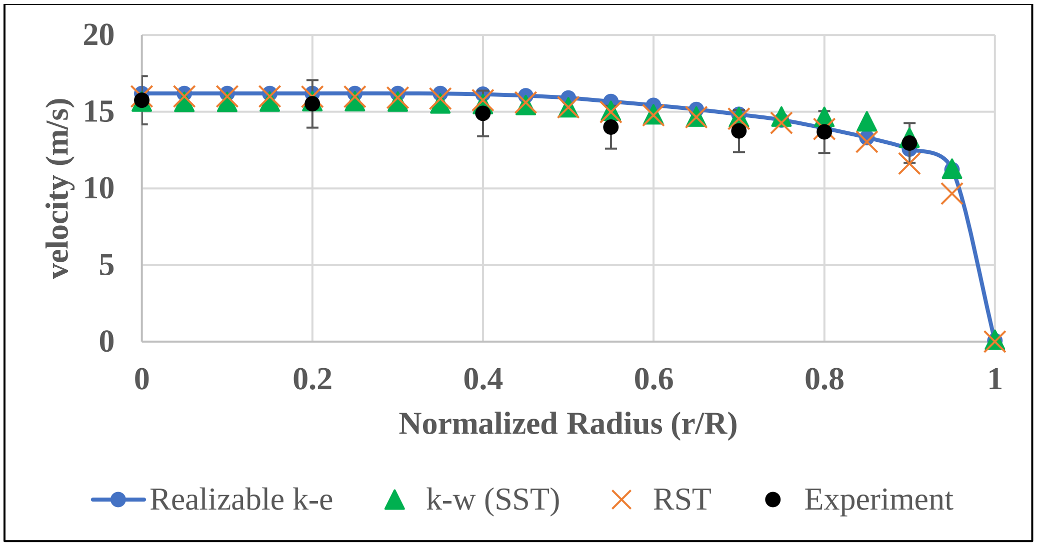

Figure 60: Velocity profile at the exit section for experimental data, k-e model, k-w (SST) model, and RST model, under baseline experimental conditions outlined at section 5.2.

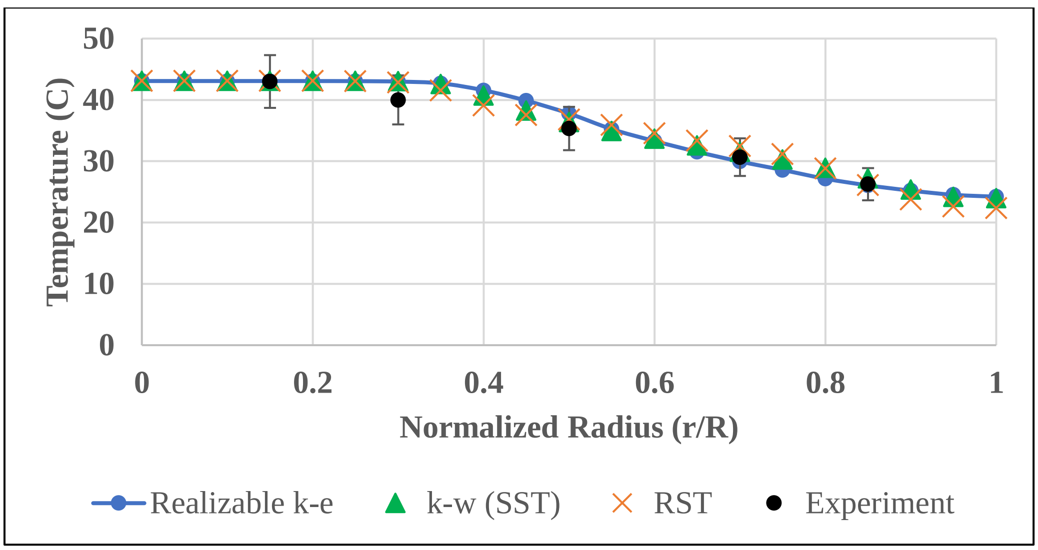

Figure 61: Temperature profile at the exit section for experimental data, k-e model, k-w (SST) model, and RST model, under baseline experimental conditions outlined at section 5.2.

The previous figures demonstrate that the $k - \omega\ (SST)$ and RST turbulence models fall within experimental error values for the outlet section velocity and temperature profiles. The $k - \omega\ (SST)$ yielded mean velocity error and mean temperature error of 1.02% and 4.12%, respectively. The average outlet pressure error is 3.96% for the $k - \omega\ (SST)$ model. The RST model resulted in a mean velocity error and mean temperature error of 2.03% and 3.57%, respectively. The average outlet pressure error is 3.79% for the RST turbulence model. **Figure 62** illustrates a sideview velocity heatmap for all models for the simulated case. **Figure 63** illustrates a sideview temperature heatmap for all models for the simulated case.

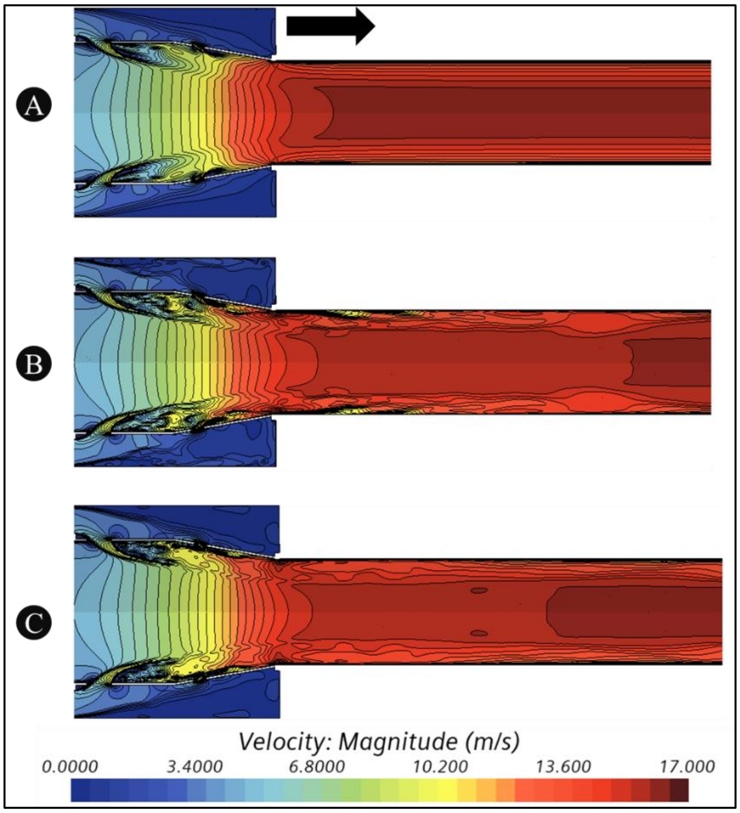

Figure 62: Sideview planar cross section of the outlet pipe, showing the velocity results from three turbulence models for the baseline case outlined in outlined at section 5.2. Flow in direction of black arrow (A) realizable k-e, (B) k-w SST, (C) RST

It can be seen that the error in between the realizable $k - \varepsilon$ and $k - \omega$ (SST) models in terms of velocity is minimal except for the cell very close to the wall. This can be ascribed to the known early separation trait of the omega model, which alters the flow speeds near the walls. The $k - \omega$ (SST) results are satisfactory and accepted as validation against the realizable $k - \varepsilon$ model for three reasons. First, this study is not concerned with the separation mechanics or eddies around the walls. Second, the affected cells are a small portion of the radial outlet pipe span, and do not significantly influence the mean values, which are the main interest of this study. Third, the error between the two prescribed models in terms of one-to-one is within experimental error ranges. The error between the realizable $k - \varepsilon$ and the RST model is minimal and falls within the experimental error ranges. Hence, the realizable $k - \varepsilon$ model holds up well against the other models and offers superior robustness, speed, and user-friendliness.

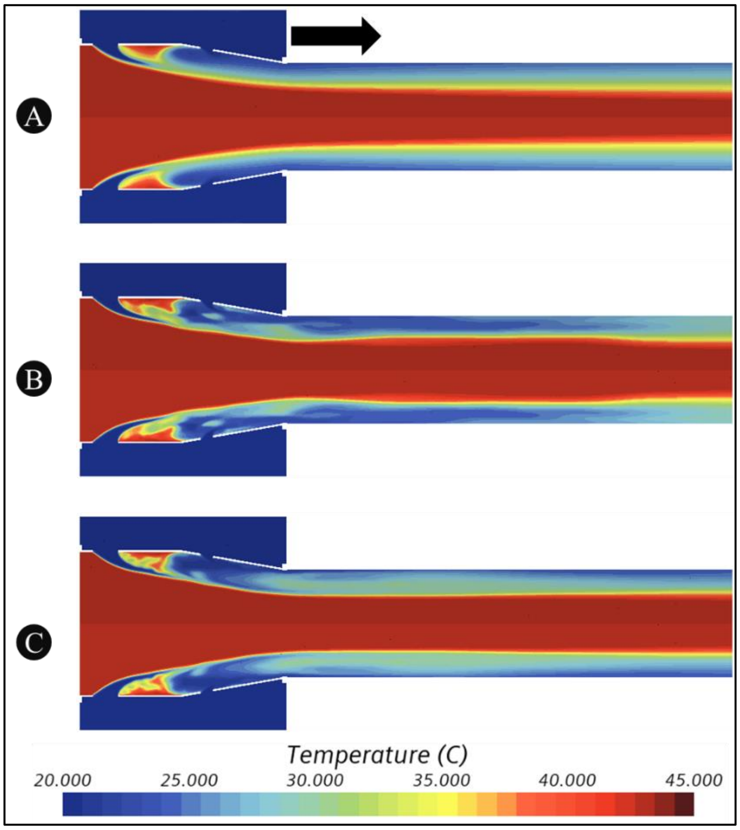

Figure 63: Sideview planar cross section of the outlet pipe, showing the temperature results from three turbulence models for the baseline case outlined in outlined at section 5.2. Flow in direction of black arrow (A) realizable k-e, (B) k-w SST, (C) RST

CHAPTER 6 – CONCLUSIONS AND FUTURE WORK

This work studies the effect of passive geometries on the temperature uniformity downstream of gas turbines dilution zones. The experimental setup simulates the non-reacting hot and cold air mixing in a dilution chamber, with inlet Reynolds number in the range of 40,000 – 95,000. Several CFD models were investigated and validated against experimental results. The proposed passive geometries include dilution jet extender parts that are installed on the large dilution holes. These jet extender parts vary in length between 5mm to 25mm, with increments of 5mm. The second proposed geometry is called the jet area modifier parts. These parts are converging nozzle parts installed on the inner side of the large dilution holes. The converging nozzle parts have lengths of 5mm, 15mm, and 25mm. Also, the converging nozzle parts have large to small area ratios of 0.5 and 0.75. The presented research investigates the effect of different factors on temperature uniformity at the downstream of dilution zones. The studied factors include temperature ratio, jet extender length, and Reynolds number. Then, sensitivity studies are presented to understand the correlation between jet extender lengths, area ratio, temperature ratio, temperature uniformity index, usefulness efficiency, and pressure drop. The main takeaways of this work are as follows:

Parametric Studies and Sensitivity:

- Based on the mesh independence study, the error compared to experimental data in high refinement mesh is 0.50%, 3.50%, and 7.50% in mean velocity, mean temperature, and average pressure, respectively. All error values are within the experimental error analysis ranges.
- The presented factorial analysis study found that the usefulness efficiency is mostly affected by the extender length followed closely by the temperature ratio.
- The Reynolds number does not have a significant effect on the usefulness efficiency, because of the parabolic rise in pressure drop compared to the linear rise in temperature

uniformity at higher Re numbers. The added pressure drop overtakes and equalizes any improvements in temperature uniformity.

- The temperature uniformity index is reduced with the increase in temperature ratio. Because the temperature gradient is high at higher temperature ratios, which requires stronger turbulence to mix the streams and attain adequate temperature uniformity.

- The temperature uniformity index has a nearly linear relation with Re. This is due to the linearity between velocity magnitude and Re, and since advection is the most prominent means of quantity transport in turbulent flows.

- Pressure drop increases with the increase in temperature ratio. There is a larger difference in viscosity and density between the hot and cold streams, which when mixed, the overall viscosity of mixed gas increases and induces pressure loss.

- Pressure drop has a nearly parabolic relation with Re. Because the velocity magnitude is linear with Re, and the velocity magnitude relates parabolically to the pressure delta in the Darcy-Weisbach relation.

Jet Extenders:

- Jet extenders result in a higher axial velocity component in the dilution jet stream. This axal velocity component is perpendicular to the crossflow stream. The relation between the jet axial velocity component varies linearly with the jet extender length. Since jet extenders protect the dilution jets from cross flow, it allows the dilution jets to develop and be ejected into the core of the main flow at a higher axial velocity. Longer jet extenders allow for a higher travel time without being impeded by crossflow, and the travel distance is directly proportional to the jet velocity.

- The improvement in temperature uniformity index (TUI), compared to baseline, is directly proportional to the temperature ratio. This is because the baseline temperature uniformity is less at higher temperature ratio, which gives the jet extenders a higher effect in increasing the dilution jet penetration, and thereby, mixing.
- The improvement in TUI is in the range of 0.90%-14.9%. It exhibits a nearly linear relation with jet extender length. Higher jet extenders protect the dilution air from crossflow and allow for deeper penetration into the main flow, and thereby, allows for better mixing.
- The added pressure drop is slightly higher for lower temperature ratio. This is because the baseline pressure drop at low temperature ratios is lower, which is susceptible to increase due to added friction by the passive geometry surfaces.
- The added pressure drop is in the range of 4.6% - 27.8%. It exhibits a nearly linear relation with jet extender length. This is because the pressure drop increases linearly with the geometry length scale in the Darcy-Weisbach relation.
- The usefulness efficiency ranges from 1.4 to 10.5. It exhibits a nearly inversely power-law relation to jet extender length. This is ascribed to the linear increase in temperature uniformity but with the stronger squared increase in added pressure drop, as defined by the relation.
- Longer jet extenders result in a more contracted normal mixture fraction (f^*) curve. This is because of the enhanced penetration of dilution jets into the main flow.
- The mass flow rate of dilution jets slightly decreases by a maximum of 10% as the jet extender length is increased. This is because longer jet extenders cause a higher friction in the flow, which results in redirecting the flow away from the holes equipped with jet extenders.

Jet Area Modifiers:

- Jet area modifiers cause a contraction in the normal mixture fraction (f^*) curve compared to baseline and same-length jet extenders. This is due to the increased velocity of dilution jets and enhanced jet penetration. This observation is confirmed by the more contracted f^* curve in smaller area ratio jet modifiers.
- In all cases, jet area modifiers performed poorly compared to same-area jet extenders. This is due to the disproportional pressure loss compared to any gains in temperature uniformity.

Turbulence Models:

- All turbulence models (realizable $k{-}\varepsilon$, $k{-}\omega$ (SST), and RST) are well-validated against experimental data. The realizable $k - \varepsilon$ model proves effective in simulating the high Reynolds number case when primary and secondary stream mixing happens in the dilution zone. The error with respect to experimental data ranges from 0.5% to 2.03% for mean velocity, 3.5% to 4.12% for mean temperature, and 3.79% to 7.5% for average pressure.
- The RST model performed slightly outside of the experimental error ranges in terms of mean velocity. This might be ascribed to the sensitivity of the RST model, and the need for high refinement mesh. In general, this demonstrates an aspect of the cost of the RST model.

Future work

- Testing the effect of guide vanes in combination with jet extenders at different temperature ratios and Reynolds number.
- Investigating the effect of streamlined bodies in the form of small-scale spherical or teardrop shape within the outlet pipe.
- Studying equipping the outlet pipe with stator-like guide vanes that redirect outer cold streams into the core of the flow.

REFERENCES

[1] G. Chintala and P. Gudimetla, "Optimum material evaluation for gas turbine blade using reverse engineering (RE) and FEA," *Procedia Eng,* vol. 97, p. 1332–1340, 2014, 10.1016/j.proeng.2014.12.413.

[2] B. MacIsaac and R. Langton, Gas Turbine Propulsion Systems, Nashville, TN: John Wiley & Sons, 2011, p. 55.

[3] Rolls Royce, *The Jet Engine,* 5 ed., Nashville, TN: John Wiley & Sons, 2015, p. 64.

[4] Federal Aviation Administration, *Airplane flying handbook: Faa-h-8083-3c,* New York: Skyhorse Publishing, 2022.

[5] M. P. Boyce, Gas Turbine Engineering Handbook, Woburn, MA: Butterworth-Heinemann, 2012, 10.1016/c2009-0-64242-2.

[6] D. J. Roddy, Advanced power plant materials, design and technology, Boca Raton, FL: CRC Press, 2010.

[7] R. J. Roback and R. P. Dring, "Hot streaks and phantom cooling in a turbine rotor passage: Part 1 - separate effects," *Journal of Turbomachinery,* vol. 115, no. 4, pp. 657-666, 1993, 10.1115/1.2929300.

[8] J. Busby, D. Sondak, B. Staubach and R. Davis, "Deterministic stress modeling of hot gas segregation in a turbine," *Journal of Turbomachinery,* vol. 122, no. 1, pp. 62-67, 2000, doi.org/10.1115/1.555428.

[9] I. Qureshi, A. D. Smith, K. S. Chana and T. Povey, "Effect of temperature nonuniformity on heat transfer in an unshrouded transonic HP turbine: An experimental and computational investigation," *Journal of Turbomachinery,* vol. 134, no. 1, p. 011005, 2012, 10.1115/1.4002987.

[10] A. M. Basol, P. Jenny, M. Ibrahim, A. I. Kalfas and R. S. Abhari, "Hot streak migration in a turbine stage: Integrated design to improve aerothermal performance," *Journal of Engineering for Gas Turbines and Power,* vol. 133, no. 6, pp. 1-10, 2011, 10.1115/1.4002349.

[11] M. G. Adams, P. F. Beard, M. R. Stokes, F. Wallin, K. S. Chana and T. Povey, "Effect of a Combined Hot-Streak and Swirl Profile on Cooled 1.5-Stage Turbine Aerodynamics: An Experimental and Computational Study," *Journal of Turbomachinery,* vol. 143, no. 2, pp. 1-21, 2021, 10.1115/1.4049103.

[12] R. S. Amano, A. Gupta, M. S. Ibrahim and B. Wiegand, "Numerical and experimental study of the effect of momentum-flux ratio on temperature uniformity in the combustor," in *11th International Energy Conversion Engineering Conference*, San Jose, CA, 2013, 10.2514/6.2013-3935.

[13] R. M. Morris, J. A. Snyman and J. P. Meyer, "Jets in crossflow mixing analysis using computational fluid dynamics and mathematical optimization," *Journal of Propulsion and Power,* vol. 23, no. 3, pp. 618-628, 2007, 10.2514/1.22136.

[14] R. S. Amano, A. Gupta, M. S. Ibrahim, A. Rux, M. Lang and T. Moll, "Numerical investigation and experimental lab setting-up for analysis of gas turbine combustor dilution process," in *Volume 5: 6th International Conference on Micro- and Nanosystems; 17th Design for Manufacturing and the Life Cycle Conference*, Chicago, Illinois, 2012, 10.1115/detc2012-71526.

[15] A. Alkhalidi, R. Amano and A. Chavoshi, "Experimental analysis of the dilution process in a gas turbine combustor simulator," in *51st AIAA Aerospace Sciences Meeting including the New Horizons Forum and Aerospace Exposition*, Grapevine (Dallas/Ft. Worth Region), Texas, 2013, 10.2514/6.2013-599.

[16] M. S. Hatch, W. A. Sowa, G. S. Samulersen and J. D. Holdeman, "Geometry and flow influences on jet mixing in a cylindrical duct," *Journal of Propulsion and Power,* vol. 11, no. 3, pp. 393-402, 1995, 10.2514/3.23857.

[17] O. M. Selim, S. Al Hamad and R. S. Amano, "Experimental and numerical study on the effect of annular combustor design on thermal uniformity jet in crossflow," *Journal of energy resources technology,* vol. 144, no. 10, pp. 1-27, 2022, 10.1115/1.4053982.

[18] A. Gupta, M. S. Ibrahim, B. Wiegand and R. Amano, "Computational and experimental study of enhanced mixing in a gas turbine combustor using guide vanes," in *ASME 2013 Heat Transfer Summer Conference*, Minneapolis, Minnesota, 2013, 10.1115/HT2013-17186.

[19] A. Gupta, M. S. Ibrahim and R. S. Amano, "Experimental study of novel passive control methods to improve combustor exit temperature uniformity," *Heat Mass Transfer,* vol. 51, no. 1, pp. 23-32, 2015, 10.1007/s00231-014-1357-6.

[20] M. D. Barringer, O. T. Richard, J. P. Walter, S. M. Stitzel and K. A. Thole, "Flow Field Simulations of a Gas Turbine Combustor," *Journal of Turbomachinery,* vol. 124, no. 3, pp. 508-516, 7 2002, 10.1115/1.1475742.

[21] T. ElGammal and R. S. Amano, "Swirlers effectiveness in the thermal uniformity of turbulent transverse jet mixing," in *55th AIAA Aerospace Sciences Meeting*, Grapevine, Texas, 2017, 10.2514/6.2017-1833.

[22] T. Elgammal and R. S. Amano, "Effectiveness of Central Swirlers in the Thermal Uniformity of Jet-in-Crossflow Mixing," *ASME. Journal of Energy Resources Technology,* vol. 140, no. 10, pp. 1-11, 2018, 10.1115/1.4040075.

[23] R. S. Amano and O. Elsayed, "Control methods to improve combustor exit temperature uniformity," *AIAA Scitech 2019 Forum,* pp. 1-15, 2019, 10.2514/6.2019-1773.

[24] M. Salewski, D. Stankovic and L. Fuchs, "Mixing in circular and non-circular jets in crossflow," *Flow, Turbulence and Combustion,* vol. 80, no. 2, pp. 255-283, 2008, 10.2514/6.2019-1773.

[25] W. Huang, J. Liu, L. Jin and L. Yan, "Molecular weight and injector configuration effects on the transverse injection flow field properties in supersonic flows," *Aerospace Science and Technology,* vol. 32, no. 1, pp. 94-102, 2014, 10.1016/j.ast.2013.12.006.

[26] J. Mi, G. J. Nathan and R. E. Luxton, "Centreline mixing characteristics of jets from nine differently shaped nozzles," *Experiments in Fluids,* vol. 28, no. 1, pp. 93-94, 2000, 10.1007/s003480050012.

[27] Y. Zhang, W. Liu, B. Wang, Y. Zhao and D. Zhang, "Investigation of injectant molecular weight effect on the transverse jet characteristics in supersonic crossflow," *Acta Astronautica,* vol. 114, pp. 101-111, 2015, 10.1016/j.actaastro.2015.05.008.

[28] J.-J. Niu, C.-L. Liu, S. Fu, H.-Y. Liu, J.-F. Lin, X.-H. Bai and L. Zhou, "Experiment investigation of impingement/effusion cooling on overall cooling effectiveness and temperature gradients of afterburner heat shields in a high-performance aircraft engine," *Experimental thermal and fluid science,* vol. 139, no. 110698, p. 110698, 2022, 10.1016/j.expthermflusci.2022.110698.

[29] G. Xie, C.-L. Liu, L. Ye, R. Wang, J. Niu and Y. Zhai, "Effects of impingement gap and hole arrangement on overall cooling effectiveness for impingement/effusion cooling," *International journal of heat and mass transfer,* vol. 152, no. 119449, p. 119449, 2020, 10.1016/j.ijheatmasstransfer.2020.119449.

[30] C.-L. Liu, G. Xie, R. Wang and L. Ye, "Study on analogy principle of overall cooling effectiveness for composite cooling structures with impingement and effusion," *International journal of heat and mass transfer,* vol. 127, no. Part B, pp. 639-650, 2018, 10.1016/j.ijheatmasstransfer.2018.07.085.

[31] K. M. B. Gustafsson and T. G. Johansson, "An experimental study of surface temperature distribution on effusion-cooled plates," *Journal of engineering for gas turbines and power,* vol. 123, no. 2, pp. 308-316, 2001, 10.1115/1.1364496.

[32] R. Da Soghe, C. Bianchini, J. D'Errico and L. Tarchi, "Effect of temperature ratio on jet impingement heat transfer in active clearance control systems," *Journal of Turbomachinery. Transactions of the ASME,* vol. 141, no. 8, pp. 1-8, 2019, 10.1115/1.4043217.

[33] Z. Zhao, L. Xi, J. Gao, L. Xu and Y. Li, "Numerical study on cooling performance of a steam-cooled blade based on response surface method," *Applied sciences,* vol. 13, no. 11, p. 6625, 2023, 10.3390/app13116625.

[34] Fluke Corporation, "Fluke 922 Airflow Meter/Micromanometer," [Online]. Available: https://www.fluke.com/en-us/product/building-infrastructure/indoor-air-quality-testing/fluke-922. [Accessed 12 12 2022].

[35] Omega Engineering Inc., *M5344 user manual,* Omega Engineering Inc., 2014.

[36] Measurement Computing Corporation, "InstaCal," Measurement Computing Corporation, [Online]. Available: https://www.mccdaq.com/daq-software/instacal.aspx. [Accessed 12 12 2022].

[37] N. O. a. A. A. US Dept of Commerce, "National Weather Service," [Online]. Available: https://www.weather.gov/. [Accessed 17 12 2022].

[38] H. Weltens, H. Bressler, F. Terres, H. Neumaier and e. al., "Optimisation of Catalytic Converter Gas Flow Distribution by CFD Prediction," in *International Congress & Exposition*, Warrendale, PA, 1993, 10.4271/930780.

[39] B. K. Sultanian, Gas Turbines: Internal Flow Systems Modeling, Cambridge, England: Cambridge University Press, 2018.

[40] H. Reichardt, "Vollständige Darstellung der turbulenten Geschwindigkeitsverteilung in glatten Leitungen," *Zamm-zeitschrift Fur Angewandte Mathematik Und Mechanik,* vol. 31, pp. 208-219, 1951, 10.1002/zamm.19510310704.

[41] J. Tu, K. Inthavong and G. Ahmadi, Computational fluid and particle dynamics in the human respiratory system, New York, NY: Springer, 2012.

[42] J. W. Mitchell and J. E. Braun, Principles of Heating, Ventilation and Air Conditioning in Buildings, Nashville, TN: John Wiley & Sons, 2014.

[43] R. B. Bird, W. E. Stewart and E. N. Lightfoot, Transport Phenomena, Revised 2nd Edition, John Wiley & Sons, 2006.

[44] ANSYS, ANSYS FLUENT User Guide v12, vol. 123, 2011.

[45] T.-h. Shih, J. Zhu and J. L. Lumley, "A Realizable Reynolds Stress Algebraic Equation Model," in *Symposium on Turbulence Shear Flows*, Kyoto, 1993.

[46] W. Rodi, Engineering Turbulence Modelling and Experiments 6, vol. 6, Elsevier Science & Technology, 2005.

[47] H. Versteeg and W. Malalasekera, An introduction to computational fluid dynamics: The finite volume method, 2 ed., Philadelphia, PA: Prentice Hall, 2007.

[48] B. E. Launder and B. I. Sharma, "Application of the energy-dissipation model of turbulence to the calculation of flow near a spinning disc," *Letters in heat and mass transfer,* vol. 1, no. 2, pp. 131-137, 1974, 10.1016/0094-4548(74)90150-7.

[49] G. F. C. Rogers, H. Cohen, P. Straznicky, A. Nix and H. I. H. Saravanamuttoo, Gas Turbine Theory, 7 ed., London, England: Pearson Education, 2017.

APPENDIX

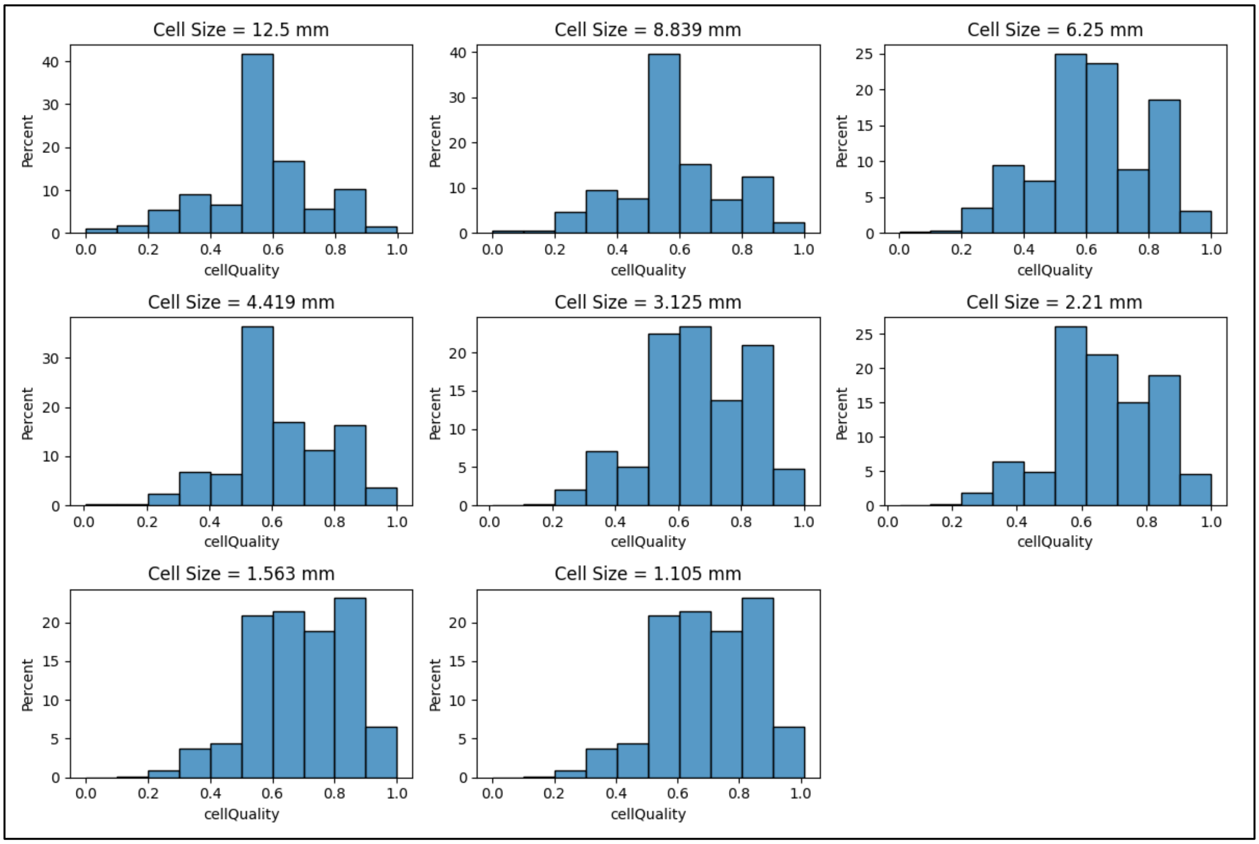

Figure 64: Mesh quality metrics - cell quality histogram plots for different cell sizes in the mesh independence study

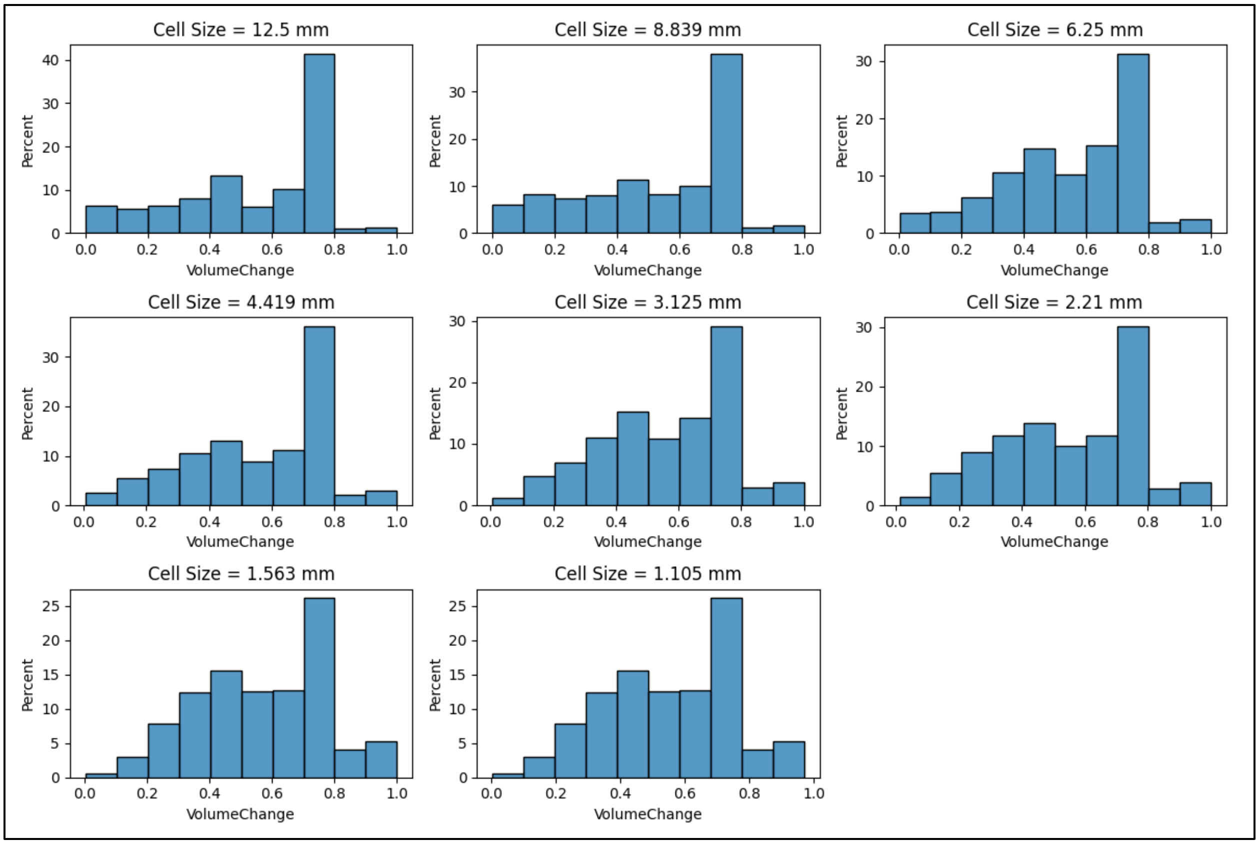

Figure 65: Mesh quality metrics – volume change histogram plots for different cell sizes in the mesh independence study

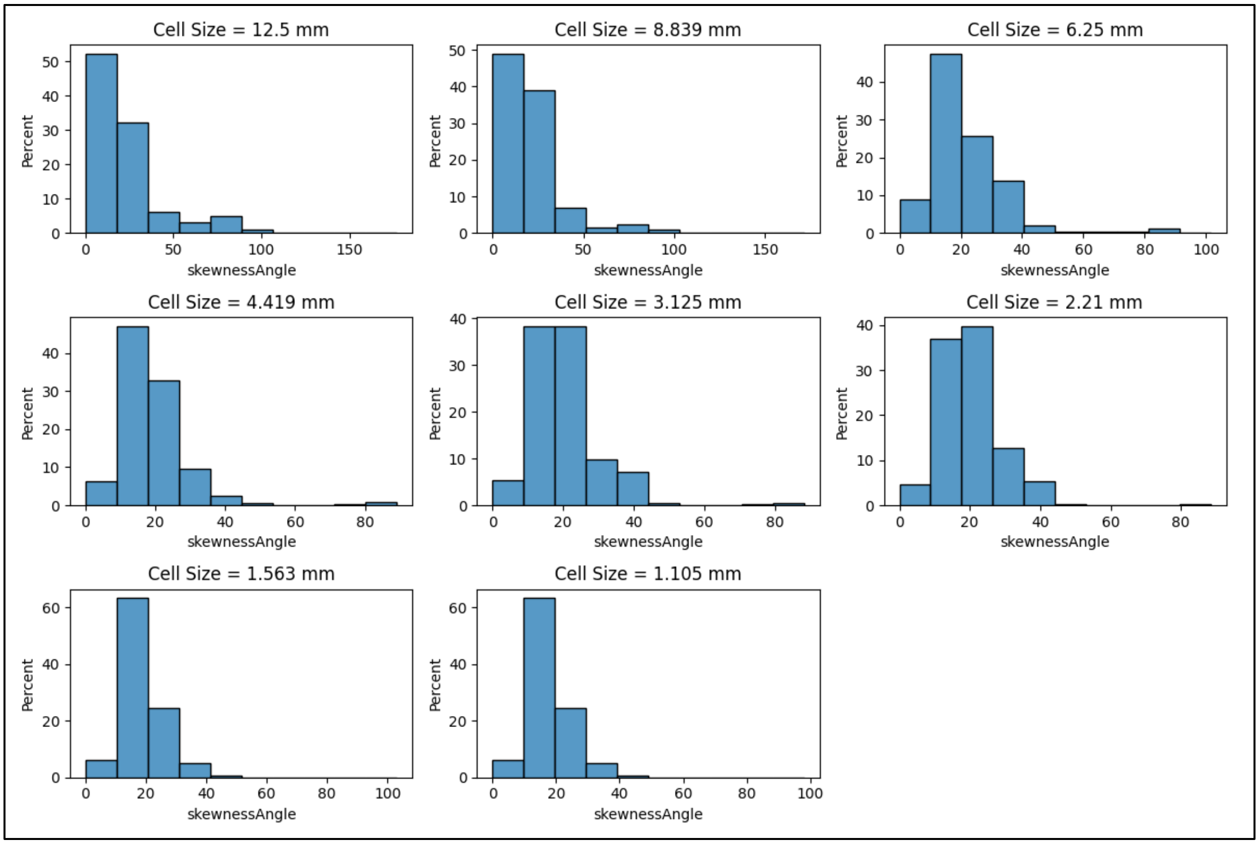

Figure 66: Mesh quality metrics – skewness angle histogram plots for different cell sizes in the mesh independence study

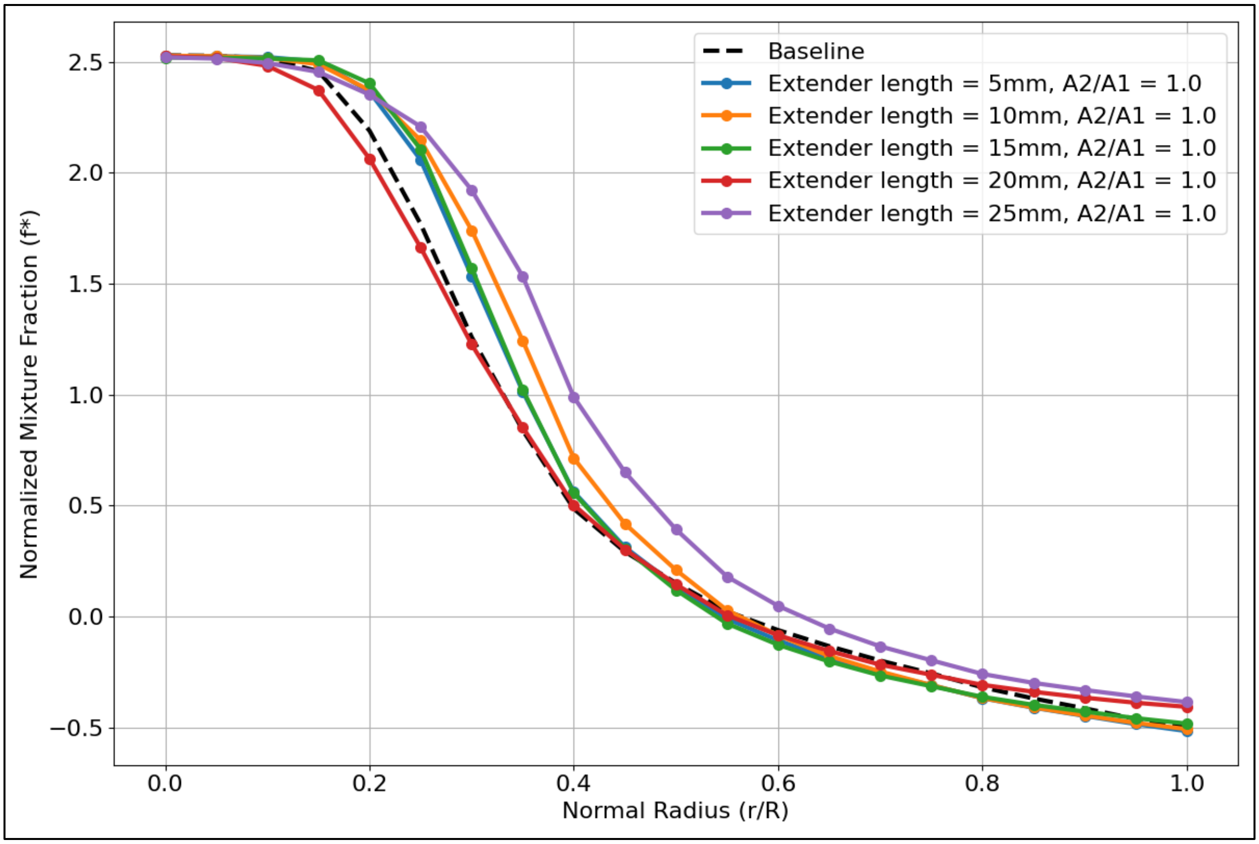

Figure 67: Normalized Mixture Fraction (f*) versus normal radius (r) for the baseline case and varying jet extender length with area ratio equal to 1 and (TR = 2.0, Re = 54,000)

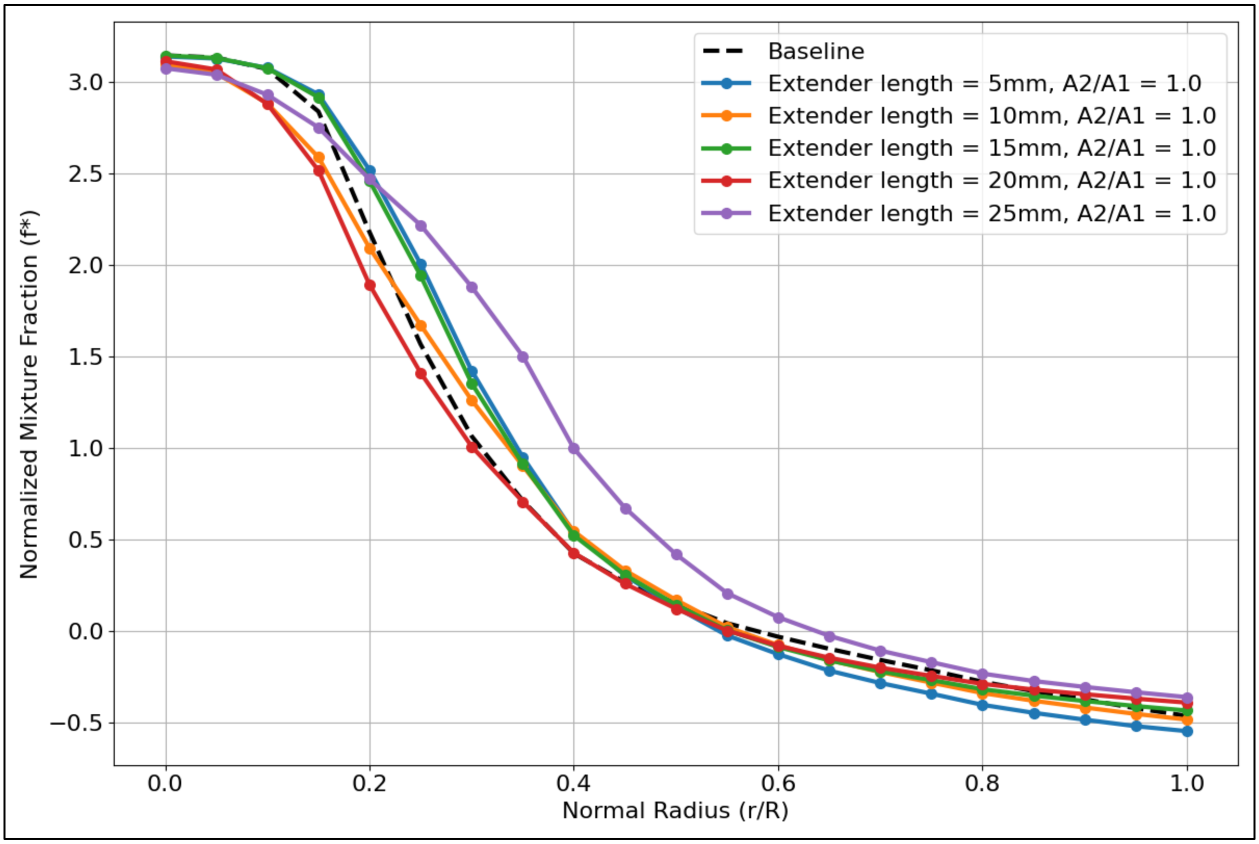

Figure 68: Normalized Mixture Fraction (f*) versus normal radius (r) for the baseline case and varying jet extender length with area ratio equal to 1 and (TR = 2.5, Re = 54,000)

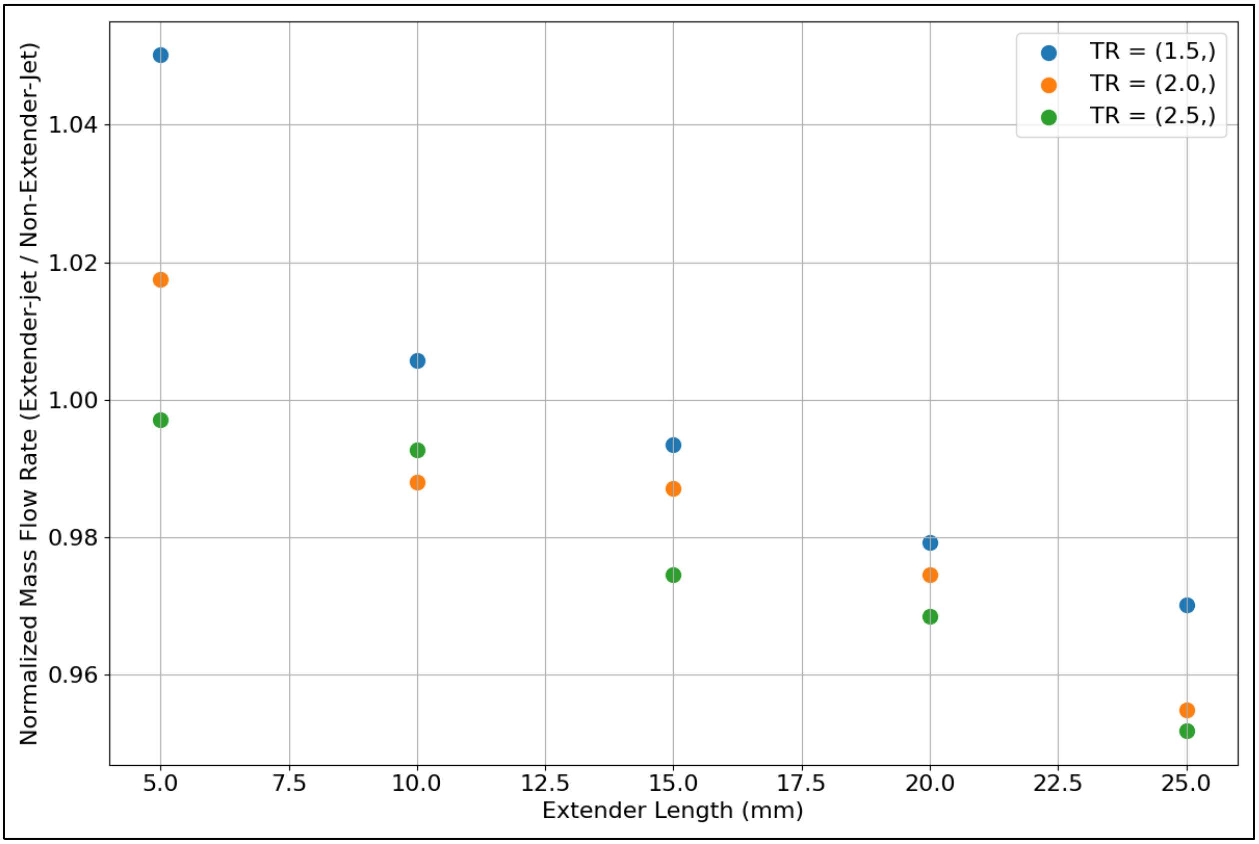

Figure 69: Normalized jet mass flow rate (jet with extender relative to jet without extender) for varying extender lengths and temperature ratios (Re = 54,000)

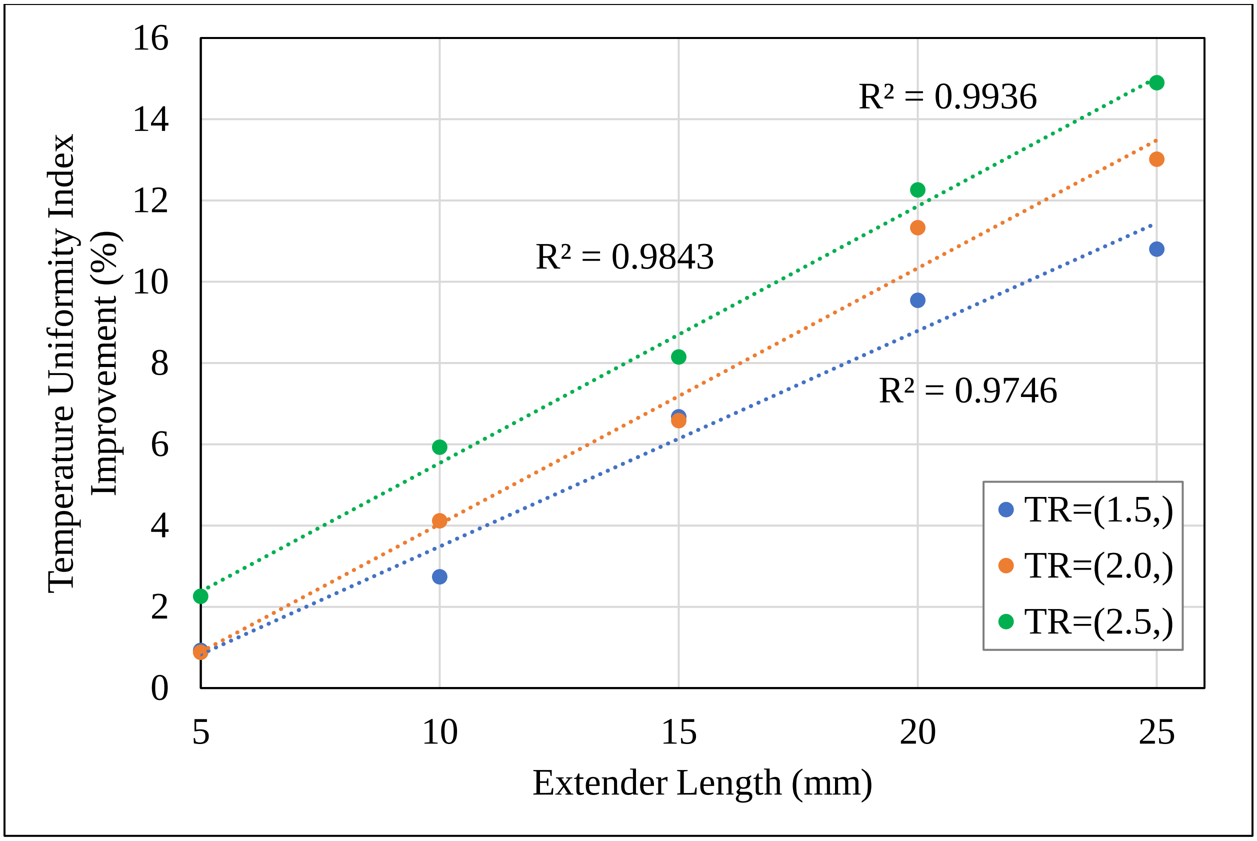

Figure 70: Temperature Uniformity Index Improvement percentage vs. jet extender length (mm) at Re = 54,000 and different temperature ratios

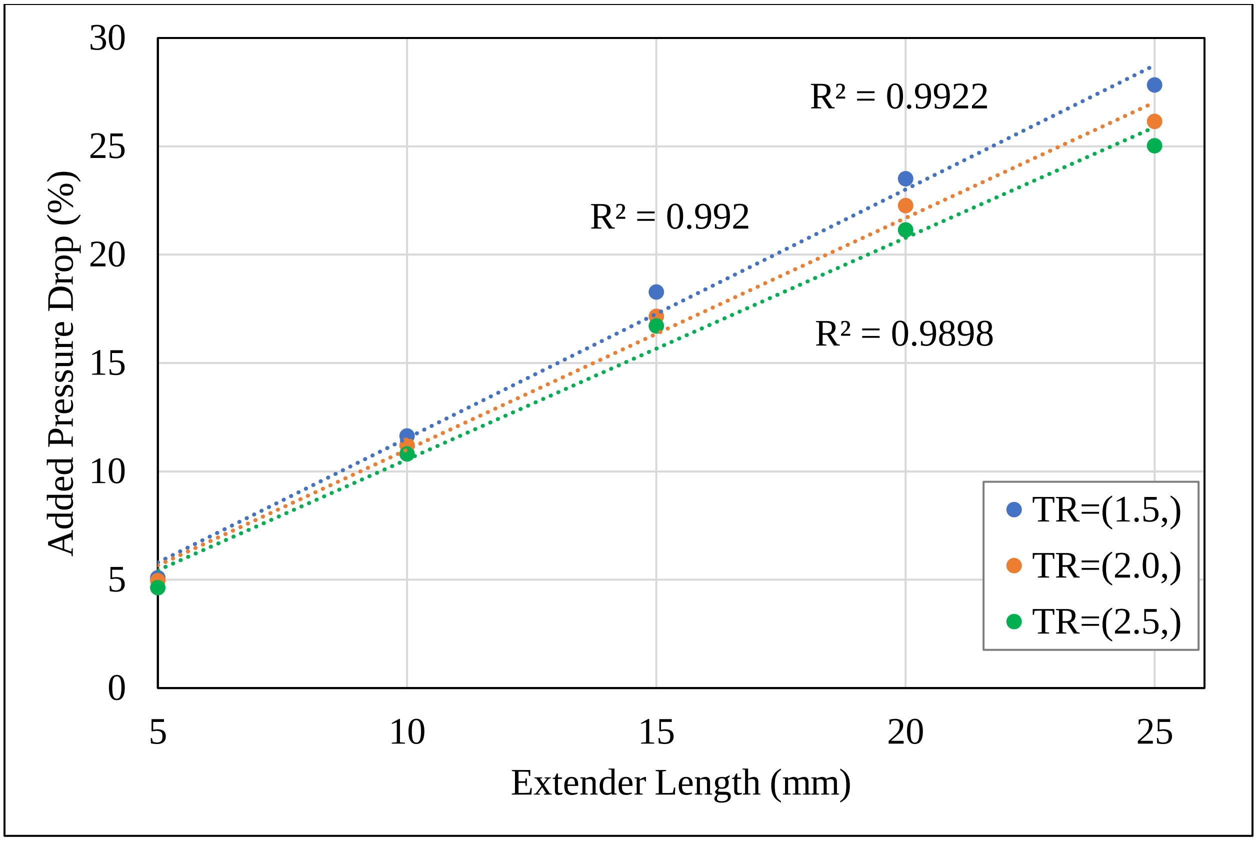

Figure 71: Added pressure drop percentage vs. jet extender length (mm) at Re = 54,000 and different temperature ratios

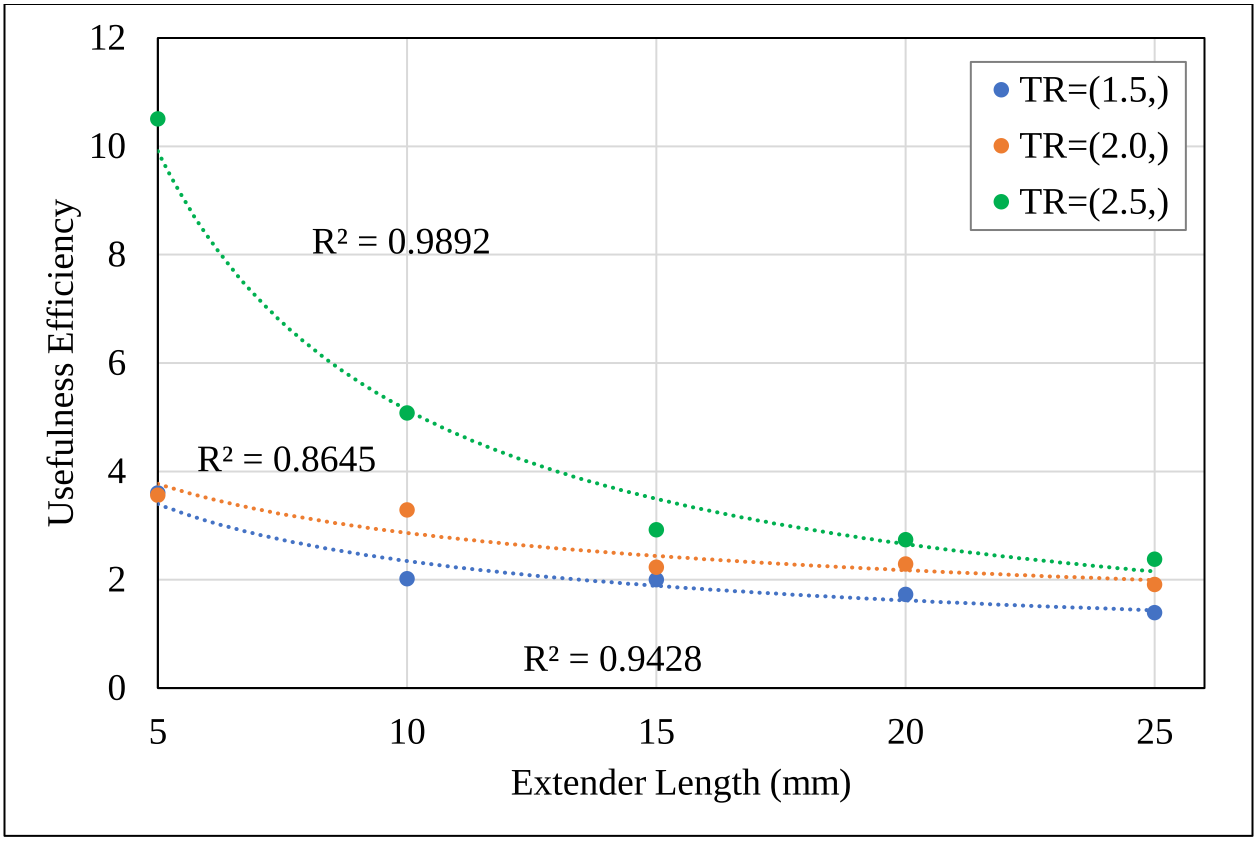

Figure 72: Usefulness Efficiency vs. jet extender length (mm) at Re = 54,000 and different temperature ratios

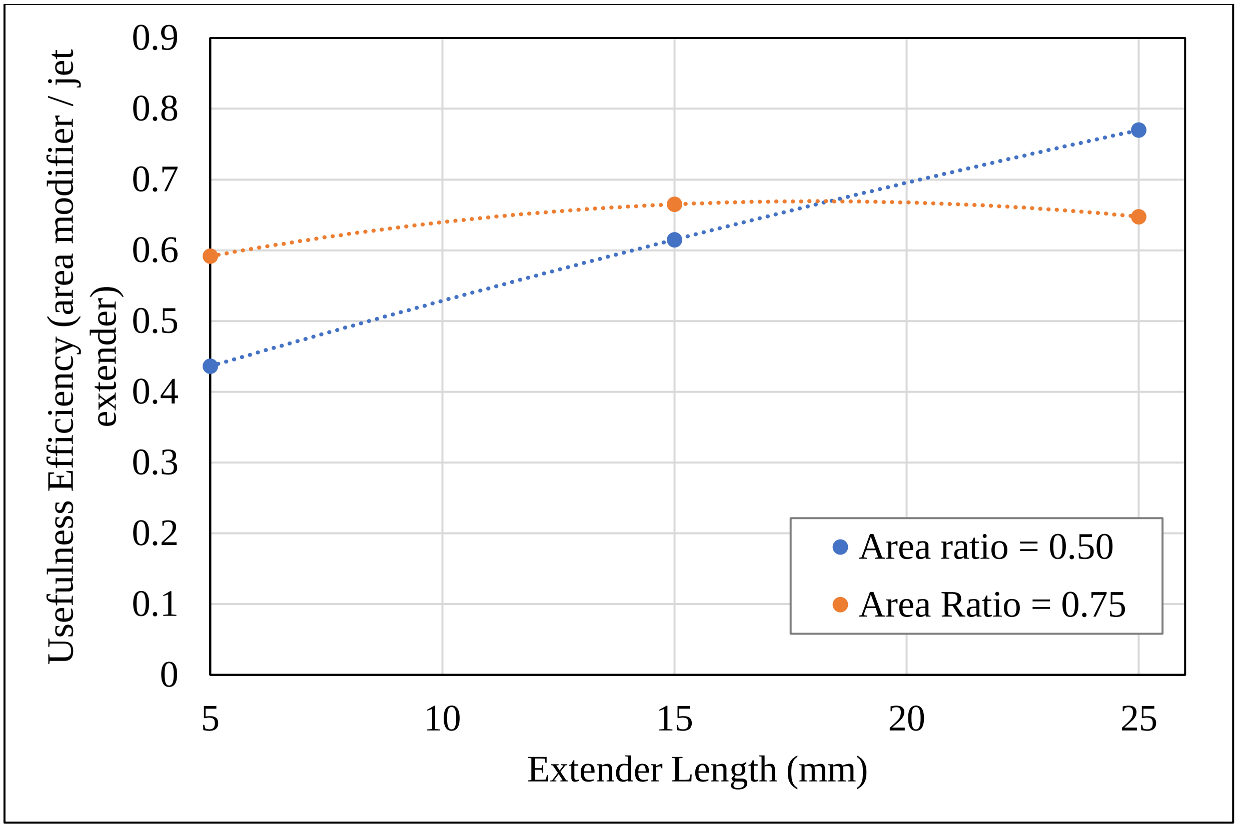

Figure 73: Normalized Usefulness efficiency of jet area modifiers vs. modifier extender length at Re = 54,000, temperature ratio = 1.5, and different area ratios